2016

Investigation on the electronic structures, hardness and thermoelectric properties of superionic thermoelectric materials

Lanling Zhao
University of Wollongong, lz083@uowmail.edu.au

UNIVERSITY OF WOLLONGONG

Institute for Superconducting & Electronic Materials

Investigation on the electronic structures, hardness and thermoelectric properties of superionic thermoelectric materials

Lanling Zhao

"This thesis is presented as part of the requirements for the Award of the Degree of Doctor of the Philosophy University of Wollongong"

January 2016

CERTIFICATION

I, Lanling Zhao, declare that this thesis, submitted in partial fulfilment of the requirements for the award of Doctor of Philosophy, in the Institute for Superconducting & Electronic Materials (ISEM), Faculty of Engineering, University of Wollongong, NSW, Australia, is wholly my own work unless otherwise referenced or acknowledged. This thesis has not been submitted for qualifications at any other academic institutions.

Lanling Zhao

January 2016

ABSTRACT

Among all the state-of-the-art high temperature thermoelectric materials, the superionic $Cu_{2-x}Se$ and $Cu_{2-x}S$ based materials, which have the phonon-liquid electron-crystal (PLEC) structure, exhibit low thermal conductivity and high zT values for their high temperature cubic phases. It has been reported that hot-pressed $Cu_{2-x}Se$ and $Cu_{2-x}S$ polycrystalline bulks show excellent thermoelectric performance, with zT values around 1.5 for $Cu_{1.98}Se$ and 1.7 for $Cu_{1.97}S$ at 1000 K, respectively. The fabrication method requires expensive equipment, however, and lengthy treatment, which obstruct the practical applications of thermoelectric materials. Therefore, it is quite essential to find a low-cost and time-saving method to fabricate highly dense thermoelectric bulk samples.

In this thesis, it is proposed that highly dense $Cu_{2-x}Se$ and $Cu_{2-x}S$ bulks could be fabricated by a facile and cheap method, denoted as the melt-quenching approach, based on our analysis of the binary phase diagram of the Cu-Se and Cu-S systems. We successfully fabricated some highly dense pure $Cu_{2-x}Se$, pure $Cu_{2-x}S$, and $Cu_{2-x}Se_{1-y}S_y$, as well as Te-doped and I-doped $Cu_{2-x}Se$ bulk samples, using the proposed facile melt-quenching approach.

It should be pointed out that the calculated electronic band structures and density of states (DOS) could provide important information on the electronic transport properties, since the thermoelectric performance is basically determined by the electronic and thermal transport properties of thermoelectric materials. Moreover, the doping approach has been considered to be one of the most effective approaches to improve the thermoelectric performance. Dopant elements not only could modify the electrical conductivity by changing the charge carrier density, but also could reduce the

thermoelectric conductivity by reducing the mean free path of lattice vibrations. Therefore, it is quite essential to do some theoretical calculations on the electronic structures for the doped systems to obtain theoretical backup for predicting variations of the electrical and thermal transport properties as well as enhancement of the overall thermoelectric performance.

In this work, we calculated the electronic band structures and DOS for the stoichiometric Cu_2Se and Cu_2S, copper deficient $Cu_{2-x}Se$ and $Cu_{2-x}S$, and Te/I/S-doped $Cu_{2-x}Se$ compounds based on the density functional theory (DFT) calculations implemented by the Cambridge Serial Total Energy Package (CASTEP). The generalized gradient approximation (GGA) was used in our calculations, with parameterization by the Perdew-Burke-Ernzerhof (PBE) and ultra-soft pseudo-potentials. The theoretical calculation results were in good agreement with our experimental observations.

It is well known that the crystal structures, such as the lattice parameters and symmetry, fundamentally determine the physical properties of a compound. Therefore, it is very necessary to investigate doping effects on the crystal structures for the $Cu_{2-x}Se$ and $Cu_{2-x}S$ systems. In this thesis, tellurium, iodine and sulphur doping effects on the lattice parameters for the $Cu_{2-x}Se$ system are systematically investigated based on Rietveld refinements of the collected X-ray diffraction patterns.

It should be pointed out that good mechanical performance is quite essential for the practical application of thermoelectric materials, because the thermoelectric materials are likely to sustain some strong mechanical and thermal stresses caused by the pressure needed to make good contact between the thermoelectric modules and the heat source and the temperature gradient inside the thermoelectric modules. It has been reported that the correlation between electronic and mechanical properties can be

related to the elastic interaction between dislocations and impurities, which will confine the motion of dislocations, and then, in turn, lead to enhanced hardness values. Therefore, it is also interesting to investigate the mechanical properties of the melt-quenched pure $Cu_{2-x}Se$ and $Cu_{2-x}S$, $Cu_{2-x}Se_{1-y}S_y$ alloys, and Te-doped and I-doped $Cu_{2-x}Se$ systems.

Besides investigations of the hardness and conducting theoretical calculations on the electronic band structures and DOS, this thesis work also included investigating the structural and thermoelectric properties for the pure $Cu_{2-x}Se$ and $Cu_{2-x}S$, $Cu_{2-x}Se_{1-y}S_y$ alloys, and Te-doped and I-doped $Cu_{2-x}Se$ bulk samples obtained from the facile melt-quenching approach.

ACKNOWLEDGEMENTS

It is my pleasure to convey my gratitude to my principle supervisor, Prof. Xiaolin Wang, and my co-supervisors, A/Prof. Zhenxiang Cheng, and Prof. Shixue Dou, for their continuous support, patience, academic guidance, and great encouragement in various ways during my PhD studies in the Institute for Superconducting & Electronic Materials (ISEM) at the University of Wollongong (UOW), Australia. I would also like to thank my co-supervisor, Prof. Jiyang Wang, in Shandong University, China, for his continued support and encouragement throughout my research in UOW, Australia.

I would like to acknowledge the Chinese Scholarship Council for the living allowance scholarship for my PhD study in ISEM. I would also like to acknowledge the University of Wollongong for providing a Free Tuition Scholarship for me, and thank Prof. Xiaolin Wang for providing a top-up Scholarship for me in the last two years of my PhD study.

I would like to thank Dr. Tania Silver for her kind help in polishing the English of the manuscripts for my journal articles and this thesis.

I would like to express my appreciation to Mr. Tomas Katkus, Dr. Germanas Peleckis, Dr. Xun Xu, Dr. Dongqi Shi, Mr. Tony Romeo, and Dr. Mitchell Nancarrow for their contributions to providing training on and maintenance of relevant instruments and for doing some measurements for me.

I would like to thank my dear friends and colleagues at ISEM including Dr. Zengji Yue, Mr. Frank Fei Yun, Mr. Feixiang Xiang, Mr. Sheik Nazrul Islam, Mr. Zhenwei Yu, Dr. Lili Liu, Mr. Yuyang Hou, Ms. Fang Li, Qiuran Yang, and others, who made my PhD study in Australia a productive, enjoyable, and memorable experience for my whole life.

I would like to express special thanks to my dearest friend Mr. Jun Wang, especially for his moral support during the whole period of my PhD and for always being there whenever I needed him.

I would like to express my gratitude to my parents, and my sister and brother-in-law for their inseparable support and love throughout my life. I would never have gone so far without their selfless dedication and unwavering belief.

Finally, I would like to thank everyone who was important to the success of my PhD study in the University of Wollongong. This thesis is dedicated to them.

TABLE OF CONTENTS

LIST OF FIGURES

LIST OF TABLES

LIST OF ABBREVIATIONS

XRD	X-ray diffraction
FE-SEM	Field emission scanning electron microscopy
EDS	Energy-dispersive X-ray spectroscopy
PLD	Pulsed laser deposition
SPS	Spark plasma sintering
DSC	Differential scanning calorimetry
CASTEP	Cambridge serial total energy package
DFT	Density functional theory
GGA	Generalized gradient approximation
PBE	Perdew-Burke-Ernzerhof
DOS	Density of states
TE	Thermoelectric
TEG	Thermoelectric generator
TEC	Thermoelectric cooler
GOF	Goodness of fit
LN	Liquid nitrogen
D	Thermal diffusivity
fcc	Face-centred cubic
R_p	Profile R-factor
R_{wp}	Weighted profile R-factor
T_c	Critical temperature
ξ	Interaction parameter
r	Radius

zT	Dimensionless figure-of-merit
$S(\alpha)$	Seebeck coefficient
ρ	Electrical resistivity
σ	Electrical conductivity
κ	Total thermal conductivity
κ_L	Lattice thermal conductivity
κ_c	Charge carrier thermal conductivity
L	Lorenz number
s	Thermoelectric compatibility factor
η	Efficiency
T_H	Temperature of the hot side
T_C	Temperature of the cool side
dd	Density
C_p	Specific heat
ΔT	Temperature difference
θ	Scattering angle
T	Absolute temperature
$\%$	Percent
$\sim$	Roughly similar
PF	Power factor
λ	Wavelength
μ	Mobility
n	Carrier concentration
m^*	Effective mass

m_e	Effective mass for electrons
f. u.	Formula unit
k_B	Boltzmann constant,
h	Planck constant
$\hbar$	Reduced Planck constant or Dirac constant
$E(k)$	Energy at the k point of the first Brillouin zone
q	Elementary charge
$\bar{\tau}$	Average scattering time

CHAPTER 1

1 INTRODUCTION

1.1 Background

High temperature thermoelectric technology has been increasingly significant in the quest for a sustainable and environmental friendly supply of clean energy, due to our increasingly severe environmental problems and the global energy crisis.[1-3] Thermoelectric technology can convert thermal energy directly into electricity when a temperature gradient is formed on thermoelectric junctions,[4-7] with such distinct virtues as high reliability, quiet operation due to the lack of moving parts, and no pollution.[8-10] Up to now, thermoelectric technology has been successfully applied in many areas, such as powering deep space missions,[11] harvesting waste heat from power plants,[12] automotive exhaust systems,[13] and other industrial processes.

Bulk thermoelectric materials can be divided into several types such as PbQ (Q = Te, Se, S) based materials, SnTe based materials, Si_xGe_{1-x} alloys, Bi_2X_3 (X = Te, Se) based materials, Mg_2X (X = Si, Sn) based materials, Sb_2Te_3 based materials, BiCuOCh (Ch = S, Se, Te) based materials, Zintl phase, skutterudites, clathrates, half-Heuslers, and liquid-like materials. Both $Cu_{2-x}Se$ and $Cu_{2-x}S$ are recently re-discovered promising high temperature thermoelectric materials with typical liquid-like crystal structures in their cubic structured phases.

Highly dense polycrystalline thermoelectric bulks are commonly synthesized by the combination of solid-state reactions and hot-pressing approaches using spark plasma sintering (SPS) or hot-pressing systems. They are very costly, and long heat treatments are needed (usually up to several days), making thermoelectric materials less suitable

for practical applications. Therefore, it is more desirable to find an effective fabrication method that is low-cost and time-saving.

In practical applications, thermoelectric materials are likely to sustain some strong mechanical and thermal stresses caused by the pressure needed to make good contact between the thermoelectric modules and the heat source, as well as the temperature gradient inside the thermoelectric modules. Therefore, good mechanical performance is quite essential for the practical applications of thermoelectric materials. Unfortunately, there is a lack of the information on the mechanical properties of thermoelectric materials with high thermoelectric performance. Hence, it is quite essential to do some investigations on the mechanical properties of thermoelectric materials.

It should be pointed out that the calculated electronic band structures and density of states (DOS) could provide much information on the electronic transport properties. Furthermore, the thermoelectric performance is basically determined by the electronic and thermal transport properties of thermoelectric materials. Moreover, the doping approach has been considered to be one of the most effective approaches to improve the thermoelectric performance, based on its effects on adjusting electrical conductivity by changing the charge carrier density and reducing the thermoelectric conductivity by reducing the mean free path of lattice vibrations. Therefore, it is quite essential to do some theoretical calculations on the electronic structures to obtain theoretical support for the modification of the electrical and thermal transport properties and achieving enhancement of the overall thermoelectric performance.

The purpose of this thesis is to fabricate highly dense thermoelectric bulk samples using a low-cost and time-saving method, and investigate the doping effects from both the theoretical and the experimental sides. In this thesis, highly dense $Cu_{2-x}S$

and $Cu_{2-x}Se$ bulks will be fabricated by a melt-quenching approach. We will perform related density functional theory calculations on the electronic band structures and density of states for the pure $Cu_{2-x}S$ and $Cu_{2-x}Se$, as well as Te-doped, I-doped, and S-doped $Cu_{2-x}Se$ systems to achieve a fundamental understanding of the doping effects on the thermoelectric properties of the $Cu_{2-x}Se$ system. In addition, we will also study the mechanical properties of these systems.

1.2 Thermoelectric effect

The thermoelectric effect describes the direct conversion between a temperature difference and electric voltage. A thermoelectric device can convert thermal energy into electricity directly when a temperature gradient is formed on thermoelectric junctions. Conversely, when a voltage is applied to a thermoelectric device, a temperature difference will be generated.

The thermoelectric effect can be used to generate electricity, and to measure or change the temperature of objects. Thermoelectric devices can be used to control the temperature due to the fact that the polarity of the applied voltage basically determines the direction of heating and cooling.

It is well known that the thermoelectric effect is related to three different effects: the Seebeck effect, Peltier effect, and Thomson effect. The Seebeck effect was discovered by a German physicist named Thomas Seebeck who reported some experiments demonstrating the production of an electrical potential difference by heating the junctions between dissimilar conductors in 1821. After thirteen years, a French physicist named Jean Charles Peltier discovered the Peltier effect, which is exactly the reverse of the Seebeck effect, describing the phenomenon that the absorption and generation of heat will occur when a current is passed through a junction between

two dissimilar conductors. Furthermore, an Irish mathematical physicist and engineer named William Thomson predicted (in 1851) and 1st Baron Kelvin observed (in 1854) the Thomson effect, which is related to the heating or cooling of a current-carrying conductor with a temperature gradient. These thermoelectric effects will be discussed in detail in the subsequent sections of this thesis.

1.2.1 Seebeck effect

Figure 1-1 is a schematic diagram of the Seebeck effect in a loop with two different conductors. An electrical potential will be generated when the two different electrical conductors are kept at different temperatures. The phenomenon was discovered by a German physicist named Thomas Seebeck (1770-1831) in 1821, who demonstrated that an electrical potential can be generated when the junctions between dissimilar conductors/semiconductors are heated.

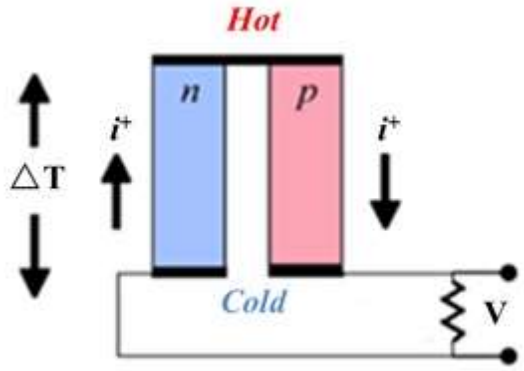

Figure 1-1 Schematic diagram showing the Seebeck effect in a loop with two different conductors.

The voltages generated by the Seebeck effect are very small, with only a few microvolts per degree Kelvin of temperature difference at the junction. Multiple such devices can be connected in series to increase the output voltages or in parallel to increase the maximum deliverable current. Large arrays of Seebeck-effect devices can

provide useful and small-scale electrical power when a large temperature difference is maintained across the junctions.

The voltage generated by the Seebeck effect can be estimated by

$$V = \int_{T_1}^{T_2} (S_B(T) - S_A(T))dT \quad (1\text{-}1)$$

where S_A and S_B are the Seebeck coefficients of conductor A and conductor B, and T_1 and T_2 are the temperatures of the cold and hot junctions, respectively. If the Seebeck coefficient is constant in the measured temperature range, Equation 1-1 can be simplified into the following format (Equation 1-2).

$$V = (S_B - S_A) \cdot (T_2 - T_1) \quad (1\text{-}2)$$

The Seebeck coefficients generally vary as functions of temperature and depend strongly on the composition of the conductor.

The Seebeck effect can be used in thermocouples to approximately measure temperature differences, and also can be used to actuate electronic switches that turn large systems on or off.

1.2.2 Peltier effect

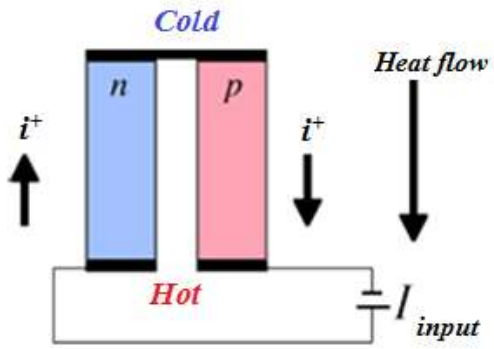

Figure 1-2 Schematic diagram of the Peltier effect.

Figure 1-2 displays a schematic diagram of the Peltier effect. This effect was discovered by the French physicist Jean Charles Athanase Peltier in 1834. The Peltier effect is related to the presence of heating or cooling at an electrified junction of two different conductors, indicating that heat may be generated (or removed) at a junction when a current flows through a junction between two conductors A and B. The Peltier heat generated at the junction per unit time, $\dot{Q}$, is equal to

$$\dot{Q} = (\Pi_A - \Pi_B)I \tag{1-3}$$

where Π_A (Π_B) is the Peltier coefficient of conductor A (B), and I is the electric current (from A to B). The Peltier coefficients represent how much heat is carried per unit charge.

The Peltier effect has been successfully applied in heat pumps and thermoelectric coolers. A typical Peltier-effect device consists of multiple junctions in series, through which a current is driven. Some of the junctions lose heat due to the Peltier effect, while others gain heat.

1.2.3 Thomson effect

Besides the Seebeck effect and Peltier effect, the third thermoelectric effect, theThomson effect, was predicted by William Thomson in 1851 and subsequently observed by Lord Kelvin (in 1854). The Thomson effect describes the heating or cooling of a current-carrying conductor with a temperature gradient.

It should be pointed out that the Seebeck coefficient is temperature dependent for many materials, and therefore, a gradient in the Seebeck coefficient could be generated due to a spatial gradient in temperature. If a current is driven through this gradient then a continuous version of the Peltier effect will occur.

If a current density $\boldsymbol{J}$ passes through a homogeneous conductor, the heat production rate $\dot{q}$ per unit volume can be predicted by the Thomson effect,

$$\dot{q} = -\text{К}\boldsymbol{J} \cdot \boldsymbol{\nabla T}_{\dot{q}} \tag{1-4}$$

where $\boldsymbol{\nabla T}$ and K are the temperature gradient and the Thomson coefficient, respectively. The first Thomson relation is

$$\text{К} \equiv \frac{d\Pi}{dT} - S, \tag{1-5}$$

and this relationship is easily shown, given that the Thomson effect is a continuous version of the Peltier effect. By considering the second relation ($\Pi = TS$), the first Thomson relation will become

$$\text{К} = T\frac{dS}{dT}, \tag{1-6}$$

indicating a subtle and fundamental connection between the Peltier and Seebeck effects. This simple form of the second Thomson relation is only guaranteed for a time-reversal-symmetric material, and it will take another complicated form if the material is placed in a magnetic field or is itself magnetically ordered. It should be pointed out that these two Thomson equations indicate that the Thomson, Peltier, and Seebeck effects are different manifestations of one effect and can be characterized by the Seebeck coefficient.

1.3 Applications of thermoelectric devices

High temperature thermoelectric technology has been increasingly significant for a sustainable and environmentally friendly supply of clean energy, due to our increasingly severe environmental problems and the global energy crisis.[1-3] Thermal energy can be

converted into electricity directly when a temperature gradient is created on thermoelectric junctions.[4-7] Thermoelectric devices can work with high reliability and quiet operation due to the lack of moving parts, and there is no pollution.[8-10]

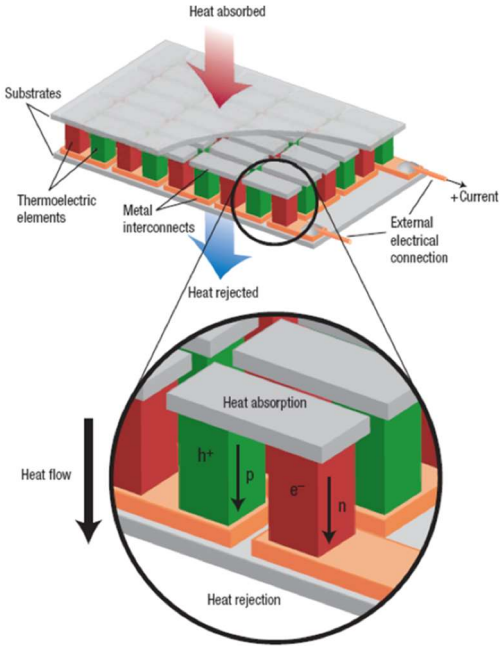

Figure 1-3 Thermoelectric module showing the direction of charge flow for both cooling and power generation.[5]

Because the voltage drop across one thermal couple is only on the order of millivolts, only connecting many in series could bring the voltage closer to that found in a typical DC power source. Actual thermoelectric devices contain many thermoelectric couples (Figure 1-3 bottom), consisting of *n*-type (containing free electrons) and *p*-type (containing free holes) thermoelectric elements wired electrically in series and thermally in parallel (Figure 1-3 top).[5]

A thermoelectric generator uses the heat flow across a temperature gradient to power an electric load through the external circuit. The temperature difference provides the voltage ($V = \alpha\Delta T$) from the Seebeck effect (where α is the Seebeck coefficient) while the heat flow drives the electrical current, which therefore determines the power

output. In a Peltier cooler the external circuit is a D.C. power supply, which drives the electric current (I) and heat flow (Q), thereby cooling the top surface due to the Peltier effect. In both the thermoelectric generator and the Peltier cooler, the heat rejected must be removed through a heat sink. This will be discussed in detail in the following sections.

Thermoelectric technology has been successfully applied in many areas, such as powering deep space missions[11] , harvesting waste heat from power plants[12] , automotive exhaust systems[13] , and other industrial processes, with several distinct virtues such as high reliability, quiet operation, and no pollution.[8, 9, 14] The efficiency of a thermoelectric generator for energy generation (η) is defined as the output electrical energy over the input thermal energy, and the maximum efficiency, denoted as the reversible Carnot efficiency, η_{max}, for actual thermoelectric devices can be estimated by

$$\eta_{max} = \frac{T_H - T_C}{T_H} \frac{\sqrt{1+z\bar{T}}-1}{\sqrt{1+z\bar{T}}+\frac{T_C}{T_H}} \quad (1\text{-}7)^{[5, 15]}$$

where T_H, T_C, $z\bar{T}$ are the temperature at the hot junction, the temperature at the surface being cooled, and the modified dimensionless figure-of-merit, respectively. It indicates that η can be improved by adjusting T_H, T_C, and $z\bar{T}$, although the last factor of $z\bar{T}$ fundamentally dominates the final η of a given thermoelectric device. As to the dimensionless figure-of-merit (zT), it can be derived as

$$zT = S^2\sigma T/\kappa = S^2\sigma T/(\kappa_L+\kappa_c) \quad (1\text{-}8)$$

where S, σ, T, κ, κ_L, and κ_c are the Seebeck coefficient or thermal power, electrical conductivity, absolute temperature, total thermal conductivity, lattice thermal conductivity, and charge carrier thermal conductivity, respectively.[4, 16-21] It should be

noted that increased σ and S, and concurrently decreased κ values are preferable to achieve high zT values.

1.3.1 Thermoelectric generators (TEGs)

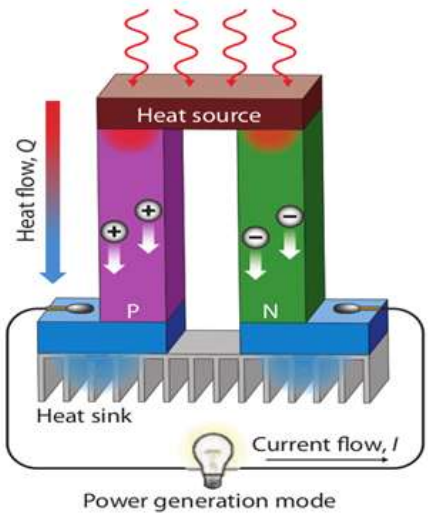

Figure 1-4 Schematic diagram of the power generation mode of thermoelectric devices based on the Seebeck effect.[22]

Thermoelectric materials can be used for power generation based on the Seebeck effect, with the corresponding devices denoted as thermoelectric generators. Figure 1-4 shows a schematic diagram of the power generation mode for thermoelectric devices based on the Seebeck effect. The charge carriers diffuse from the hot side to the cold side and an electric voltage or current can be detected in the device when a temperature gradient is applied to the thermal couple. In order to get sufficiently high voltage, the actual thermoelectric generators contain many thermal couples connected in series.

Thermoelectric generators have been successfully applied in many areas, such as power generation for space missions and waste heat recovery in automotive applications and from steam power plants, the steel industry, the cement industry, oil refineries, and the paper and printing industry, as well as the aluminum industry. In addition,

thermoelectric generators can also be used for waste heat recovery from the human body.[23]

Currently, thermoelectric materials for power generation purposes are based on PbTe in low and medium temperature gradient applications.[24] Skutterudite materials have emerged as a promising class of materials for thermoelectric conversion applications in the 500 to 900 K range since the 1990s. SiGe alloys and FeSi are employed in high temperature thermoelectric generators.[25] It should be pointed out that iron silicate materials exhibit very high durability and tolerate high mechanical stresses at high temperatures.[26] In the last few years, the zT values have been greatly enhanced by employing such methods as band engineering and nanostructuring.

1.3.2 Thermoelectric coolers (TECs)

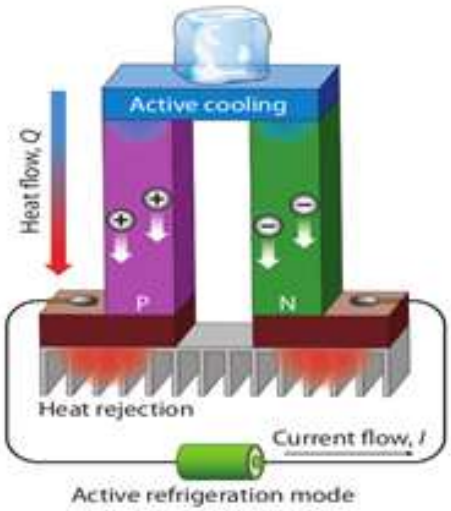

Figure 1-5 Schematic diagram of the active refrigeration mode of thermoelectric devices based on the Peltier effect.[22]

Thermoelectric materials can also be used as refrigerators known as Peltier coolers or thermoelectric coolers (TEC). Figure 1-5 shows the schematic diagram for the active

refrigeration mode of thermoelectric devices based on the Peltier effect. The TEC device has two sides, and when a DC current flows through the device, it brings heat from one side to the other, so that one side gets cooler while the other gets hotter. The "hot" side is attached to a heat sink so that it remains at ambient temperature, while the cool side goes below room temperature. In some applications, multiple coolers can be cascaded together for lower temperature.

TECs are typically connected sides by sides and sandwiched between two ceramic plates. They have several distinct advantages such as no moving parts, no chlorofluorocarbons, flexible shape, small size, long lifetime and controllable via changing the input voltage/current. The temperature control within fractions of a degree can be maintained in TECs. However, TECs only can dissipate a limited amount of heat flux and are relegated to applications with low heat flux.

TECs are commonly used in camping, portable coolers, cooling electronic components and small instruments. The cooling effect of Peltier heat pumps can be used to extract water from the air in dehumidifiers. A camping/car type electric cooler can typically reduce the temperature by up to 20 C below the ambient temperature. Climate-controlled jackets are also beginning to use TECs. They are also used for wine coolers and replacing heat sinks for microprocessors.

1.4 Thermoelectric parameters

It is well known that the efficiency for a thermoelectric device is mainly determined by zT, defined as $zT = S^2 T\sigma / \kappa$, where S, σ, T, κ are the Seebeck coefficient, electrical conductivity, absolute temperature, and total thermal conductivity, respectively. In this part, these thermoelectric parameters will be discussed in detail one by one.

1.4.1 Seebeck coefficient (*S*)

The Seebeck coefficient, *S*, of a material is a measure of the magnitude of an induced thermoelectric voltage in response to a temperature difference across that material, as induced by the Seebeck effect. It is generally given the unit of microvolts per Kelvin (μV/K) with positive or negative values depending on the charge carrier type of holes or electrons.

The Seebeck coefficient is defined in terms of the portion of electric current driven by temperature gradients,

$$\boldsymbol{J} = -\sigma \boldsymbol{\nabla} V - \sigma S \boldsymbol{\nabla} T \tag{1-9}$$

where $\boldsymbol{J}$, σ, $\boldsymbol{\nabla} V$, and $\boldsymbol{\nabla} T$ are the current density, electrical conductivity, voltage gradient and temperature gradient, respectively. The zero-current, steady state special case described above has $\boldsymbol{J} = 0$, indicating that the two current density terms can be cancelled out and $\boldsymbol{\nabla} V = S \boldsymbol{\nabla} T$.

Experimentally, *S* can be determined by the following Equation 1-10.

$$S = -\frac{V_{left} - V_{right}}{T_{left} - T_{right}} \tag{1-10}$$

According to this equation, if *S* is positive, the end with the higher temperature should have the lower voltage, and vice versa. The voltage gradient ($\boldsymbol{\nabla} V$) in the material will point against the temperature gradient ($\boldsymbol{\nabla} T$).

It should be pointed out that *S* is generally dominated by the contribution from the diffusion of charge carriers, tending to push charge carriers towards the cold side of the material until a compensating voltage has built up. As a result, in *p*-type semiconductors where the charge carriers are holes, *S* is positive. Likewise, in *n*-type semiconductors

with electrons as the charge carriers, *S* is negative. In most conductors, however, the charge carriers exhibit both hole-like and electron-like behaviour, and the sign of *S* usually depends on which type of charge carrier is predominant.

High *S* values are preferable for good thermoelectric materials that can give high thermoelectric performance with high *zT* values. *S* can be estimated by the following formula, [5, 27, 28]

$$S = \frac{8\pi^2 k_B^2}{3eh^2} m^* T \left(\frac{\pi}{3n}\right)^{2/3} \quad (1\text{-}11)$$

where n, k_B, h, and m^* are the charge carrier density, Boltzmann constant, Planck constant, and DOS effective mass of the charge carriers, respectively. Furthermore, information on effective mass and charge carrier density can be deduced from the related density functional theory calculations on band structures and density-of-states (DOS). In this regard, *S* can be roughly predicted through performing theoretical calculations on the band structures and DOS.

1.4.2 Electrical conductivity (σ)

Electrical conductivity is an intrinsic property of materials that quantifies the ability of a given material to conduct an electric current. It is commonly represented by σ, with the units S·cm^{-1}. The electrical conductivity is defined as the ratio of the created current density to the applied electric field,

$$\sigma = \frac{J}{E} \quad (1\text{-}12)$$

where *J* is the magnitude of the created current density and *E* is the magnitude of the electric field. It is well known that σ and *S* can be estimated by the following

formulas,[5, 27, 28]

$$\sigma = ne\mu \tag{1-13}$$

where n and μ are the charge carrier density and carrier mobility, respectively. Moreover, the carrier mobility (μ) can be derived from the following equation,

$$\mu = \frac{q}{m^*}\bar{\tau} \tag{1-14}$$[29, 30]

which indicates that the carrier mobility is related to the elementary charge, conduction effective mass, and average scattering time of the charge carriers. Furthermore, the band effective mass can be estimated by the following formula

$$\frac{1}{m^*} = \frac{1}{\hbar^2}\frac{d^2E(k)}{d\kappa^2} \tag{1-15}$$

where $\hbar$ and $E(k)$ are the reduced Planck constant or Dirac constant and the energy at the k point of the first Brillouin zone, respectively. It should be noted that the $\frac{d^2E(k)}{d\kappa^2}$ part can be obtained from the calculated electronic band structure. Therefore, the estimation of σ can also be roughly achieved if the average scattering time is considered as a constant.[31, 32]

1.4.3 Power factor (PF)

The power factor (PF) is parameter that is used to estimate the usefulness of a given material in a thermoelectric generator or cooler, and it is defined as

$$PF = S^2\sigma \tag{1-16}$$

where S and σ are the Seebeck coefficient and electrical conductivity under a given

temperature gradient, respectively. Thermoelectric materials with a high power factor are able to move more heat or extract more energy from that heat in a space-constrained application, but are not necessarily more efficient in generating this energy.

1.4.4 Thermal conductivity (κ)

Thermal conductivity is a material property that describes the ability to allow the flow of heat from its warmer surface through the material to its colder surface, determined as the heat energy transferred per unit of time and per unit of surface area divided by the temperature gradient, which is the temperature difference divided by the distance between the two surfaces. Generally, the thermal conductivity is expressed by the symbol κ with units of $W \cdot m^{-1} \cdot K^{-1}$.

The thermal conductivity of a given system can be calculated by two different approaches. The first approach is to employ the Green-Kubo relation giving the exact mathematical expression for the transport coefficient γ in terms of integrals of time correlation functions, as shown in Equation 1-17.

$$\gamma = \int_0^\infty \langle \dot{A}(t)\dot{A}(0) \rangle dt \tag{1-17}$$

This approach, however, requires the use of a molecular dynamics computer simulation when calculating the thermal conductivity of a dense fluid or solid. The second approach is based on the relaxation time. The phonons in a given system are known to be scattered due to the anharmonicity within the crystal potential. As to the mechanisms of the phonon scattering, there are mainly three types: boundary scattering, mass defect scattering, and phonon-phonon scattering.

It is well known that $\kappa = \kappa_c + \kappa_L$, where κ_c and κ_L are the charge carrier thermal conductivity and the lattice thermal conductivity, respectively, since electrons and lattice vibrations are two ways for thermal energy to be transported in solids. Furthermore, the charge carrier thermal conductivity can be estimated by

$$\kappa_c = L\sigma T \tag{1-18}$$

where L, σ, and T are the Lorentz number, electrical conductivity, and absolute temperature, respectively. The phonon thermal conductivity can be expressed using the following relationship, which is confirmed by kinetic theory[33] and the Boltzmann transport equation.[34, 35]

$$\kappa_L = \frac{1}{3}\int C_v(\omega) \cdot v(\omega) \cdot l(\omega) d\omega \tag{1-19}$$

where C_v, v, l, and ω are the specific heat, phonon group velocity, phonon mean free path, and phonon frequency, respectively. Hence, for good electrical conductors such as metals, electrons are the dominant thermal energy carriers, while the lattice vibrations predominately determine the heat transport in many non-metals such as semiconductors and dielectric materials.

1.4.5 Dimensionless figure-of-merit (zT)

It is well known that the ability of a given thermoelectric material to efficiently produce thermoelectric power is related to its dimensionless figure-of-merit, which is defined in Equation 1-20, in which S, σ, κ, κ_c, κ_L, PF, and T are the Seebeck coefficient, electrical conductivity, total thermal conductivity, charge carrier thermal conductivity, lattice thermal conductivity, power factor, and absolute temperature, respectively.

$$zT = \frac{S^2\sigma}{\kappa}T = \frac{S^2\sigma}{\kappa_c+\kappa_L}T = \frac{PF}{\kappa_c+\kappa_L}T \quad (1\text{-}20)$$

The higher the zT value, the higher the efficiency that could be obtained from thermoelectric generators or coolers. It should be noted that an important drawback for thermoelectric devices is their low efficiency, which seriously limits wider applications of thermoelectric materials. If the efficiency could be significantly improved, thermoelectric devices could be an important part of the solution to today's energy challenges. The improvement of zT has always been an important research topic in the field of thermoelectric materials, and many methods have been developed to achieve enhanced zT values through increasing PF or decreasing κ values.

1.4.6 Thermoelectric compatibility factor (s)

Besides the above discussed electrical conductivity, Seebeck coefficient, power factor, total thermal conductivity, charge carrier thermal conductivity, and lattice thermal conductivity, there is another thermoelectric property, the thermoelectric compatibility factor, s, which becomes important when different materials or large temperature differences are used. For power generators and Peltier coolers, s can be estimated by Equations 1-21[5, 36, 37] and 1-22[5, 38], respectively, where α is the Seebeck coefficient, zT is the dimensionless figure-of-merit, and T is the absolute temperature.

$$s = \frac{\sqrt{1+zT}-1}{\alpha T} \quad (1\text{-}21)$$

$$s = \frac{\sqrt{1+zT}+1}{\alpha T} \quad (1\text{-}22)$$

It should be noted that, for practical applications of thermoelectric materials, besides having high zT values, the thermoelectric compatibility factor is crucial for the

efficient operation of a high temperature thermoelectric device.[5, 15, 36, 37, 39] The closer the *s* for two *n*-type and *p*-type materials, the higher the combined efficiency that will be achieved when they are adjoining segments in one thermoelectric device. Generally, this parameter should not change by more than a factor of two from the hot to the cold end of a thermoelectric element.

1.5 Approaches used to optimize thermoelectric properties

High temperature thermoelectric materials have attracted great attention due to their crucial role in direct conversion from thermal energy to electrical energy in solid-state waste heat recovery applications for decades. Thermoelectric technology has many distinct virtues, such as no hazardous emissions and no mechanical moving parts, and it is also considered to be a clean and sustainable energy source.

The critical limitation blocking the widespread use and adoption of thermoelectric materials is the relatively low conversion efficiency, which can be assessed by the reversible Carnot efficiency (η), defined as the fraction of absorbed heat that is converted into work, which can be estimated by the following formula

$$\eta_{max} = \frac{T_{hot}-T_{cold}}{T_{hot}} \frac{\sqrt{1+z}-1}{\sqrt{1+z}+\frac{T_{cold}}{T_{hot}}} \quad (1\text{-}23)^{[40\text{-}44]}$$

where T_{hot}, T_{cold}, and zT are the temperatures at the hot and cold ends of the thermoelectric generator, and the dimensionless figure-of-merit for the constituent thermoelectric materials, respectively. Obviously, η is a function of the materials' zT values, the average working temperature of the generator, and the temperature difference between the hot (T_{hot}) end and the cold (T_{cold}) end. It

should be noted that zT fundamentally dominates the final η values, although an improved η could also be achieved by adjusting T_{hot} and T_{cold}.

As to the definition of the dimensionless figure-of-merit (zT), the zT value is related to the Seebeck coefficient (S), the electrical conductivity (σ), the absolute temperature (T), and the total thermal conductivity (κ), which is the sum of the charge carrier thermal conductivity (κ_c) and the lattice thermal conductivity (κ_L).

In order to obtain enhanced zT values, the highest possible electrical conductivity and Seebeck coefficient, and the lowest possible thermal conductivity should be achieved synergistically. Apart from the independent parameter κ_L, however, the other transport properties that define the material's efficiency (S, κ, and κ) cannot be independently tuned because of the strong interdependence among the properties via the carrier concentration in a given thermoelectric material.[5] As a result, the primary conventional efforts for maximizing zT of thermoelectric materials relate to carrier concentration optimization[5, 45] and lattice thermal conductivity reduction.[10, 46-48]

1.5.1 Approaches to optimize the electronic transport properties

The Seebeck coefficient and electrical conductivity can be estimated by Equation 1-11 and Equation 1-13. Moreover, the carrier mobility (μ) and effective mass (m^*) can be derived from Equation 1-14 and Equation 1-15, respectively. These formulas relating to σ and S indicate that changing the charge carrier density and mobility, as well as the effective mass, should be effective methods to obtain optimized σ and S values, and thus achieve enhanced thermoelectric performance with increased zT values.

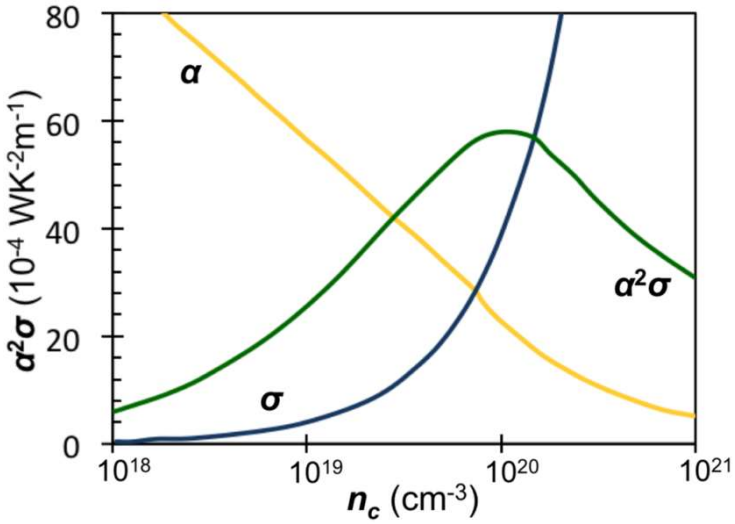

Figure 1-6 Variation in the electrical transport properties as a function of carrier concentration.[49]

Figure 1-6 shows the variation of electrical transport properties as a function of carrier concentration, indicating that the ideal carrier concentration to achieve a high power factor is in the range from 10^{19} to 10^{21} cm^{-3}. Doping approaches using elements with different numbers of valence electrons compared to the substituted element has successfully been proved to effectively modify the carrier concentration and give the doped systems greatly enhanced thermoelectric performance.[50]

It is well known that the optimal carrier concentration in thermoelectric materials also depends on the band structure.[10] Using a classical statistics approximation, Ioffe[45] estimated that n is proportional to $(mT)^{3/2}$ for a single carrier type system, where m^* is density of states effective mass and can be estimated by $m^* = N_V^{2/3} m_b^*$ for semiconductors having valley degeneracy of N_V and an average band mass of m_b^* for each valley. Hence, band structure engineering should be an effective method to achieve an optimal carrier concentration by modifying the relative energies of the electronic bands through alloying[10, 51, 52] or by introducing impurity energy levels that are

resonant with the host band through resonant doping,[53] or both[54, 55]. It has been reported that in PbTe-based, [56-59] SnTe-based, [60-62] and other types[63] of thermoelectric materials, greatly enhanced zT values have been achieved by applying the band structure engineering approach.

1.5.2 Approaches to optimize the thermal transport properties

It should be pointed out that it is not always advantageous to have a very high electrical conductivity because this will result in high thermal conductivity based on the Wiedeman-Franz (WF) law

$$\kappa_c = L\sigma T \tag{1-24}$$

$$L = \frac{k_B^2}{e^2}\left[\frac{\left(p+\frac{7}{2}\right)\left(p+\frac{3}{2}\right)F_{\left(p+\frac{5}{2}\right)}F_{\left(p+\frac{1}{2}\right)}-\left(p+\frac{5}{2}\right)^2F_{\left(p+\frac{3}{2}\right)}^2}{\left(p+\frac{3}{2}\right)^2F_{\left(p+\frac{1}{2}\right)}^2}\right] \tag{1-25}$$

where L, e, and k_B are the Lorenz number, electronic charge, and Boltzmann constant, respectively. Here, p appears when estimating the relaxation time, τ,

$\tau \approx E^p$

where E is the energy of the electrons. F is the Fermi-Dirac integral of order r, which is defined as

$$F_r(\eta_F) = \int_0^\infty \frac{x^r}{1+e^{x-\eta_F}}dx \tag{1-26}$$

where η_F is the reduced Fermi energy. For n-type semiconductors, η can be written as

$$\eta_F = \frac{E_F-E_C}{k_BT} \tag{1-27}$$

where E_F and E_C are the energy of the Fermi level and the conduction band, respectively. The above formulas involving L indicate that for semiconductors, L is related to the position of the Fermi energy level and the relaxation time of the electrons. Typically, L is taken to be 2.45×10^{-8} $W \cdot m \cdot K^{-2}$ for metals and degenerate semiconductors, although it can vary, depending on the temperature and material.

It should be pointed out that an effective way to maximize zT values through adjusting the thermal conductivity is to manipulate the lattice vibration part, κ_L, which is the only parameter not determined by the electronic structure of the thermoelectric material. All other material parameters, such as the electrical conductivity, Seebeck coefficient, and charge carrier thermal conductivity, are correlated with the electronic structure of the material and thus, in most cases, cannot be optimized independently.

The lattice thermal conductivity can be expressed using Equation 1-19, which is confirmed by kinetic theory[33] and the Boltzmann transport equation.[34, 35] The strategies used to reduce the lattice thermal conductivity can be categorized into three types, corresponding to reduction of the specific heat, the phonon group velocity, and the mean free path of thermoelectric materials. This will be discussed in detail in the following paragraph.

Specific heat: Materials with large unit cells or complicated crystal structures can benefit from the reduction of specific heat by utilizing the nearly zero phonon group velocity of the optical branch. When the number of atoms increases in a unit cell, this induces an increase in the optical branch, since the total number of acoustic branches is limited to 3; 1 in the longitudinal and 2 in the transverse acoustic branches. Therefore, the material absorbs heat, but only a small fraction of the energy is transported through the acoustic branch, leading to low thermal conductivity.

In the long wavelength limit, the phonon group velocity approaches the speed of sound. To reduce the speed of sound, weak bonding and heavy mass are required. It is challenging to change the phonon dispersion, since the feature size of a material should be less than the phonon coherence length in a rough estimation. Nevertheless, this can be implemented in superlattice structures. Due to the standing wave generated due to constructive interference by Bragg reflection, phonon band gaps can be generated within the acoustic branch, which reduces the thermal conductivity because the phonon group velocity becomes zero at the band gap.

Grain boundary scattering, impurity scattering and phonon-phonon scattering are commonly used to minimize the mean free path of the lattice vibrations. Specifically, scattering from alloy atoms, vacancies, nanoparticles, and nanosized holes are four types of different impurity scattering processes. Alloying is a very efficient way to reduce thermal conductivity while maintaining the crystallinity of a material to ensure good electrical transport. Scattering due to both alloy atoms and vacancies follows the Rayleigh law, which predicts selective scattering of short-wavelength phonons. To further reduce the thermal conductivity by scattering mid- to long-wavelength phonons, nanoparticle structured thermoelectric materials have been proposed. Experimental results reveal that remarkable reductions in thermal conductivity can be observed in a material containing nanoscale holes. In such material, the feature size between holes is larger than the phonon coherence length, so changes in phonon dispersion might not occur. In contrast to grain boundary and impurity scattering, phonon-phonon scattering is inelastic and intrinsic. Therefore, it is not trivial to enhance the scattering rate through external means. Lone-pair electrons and acoustical-to-optical phonon scattering have been proposed as phonon-phonon scattering approaches. The electrostatic repulsion between lone-pair electrons and neighboring ions creates anharmonicity, increasing the

Grüneisen parameter. Acoustical phonons can efficiently be promoted to optical phonons by phonon-phonon scattering in a material with a small gap between the acoustic and optical branches.

1.6 Thermoelectric materials

1.6.1 Review of bulk thermoelectric materials

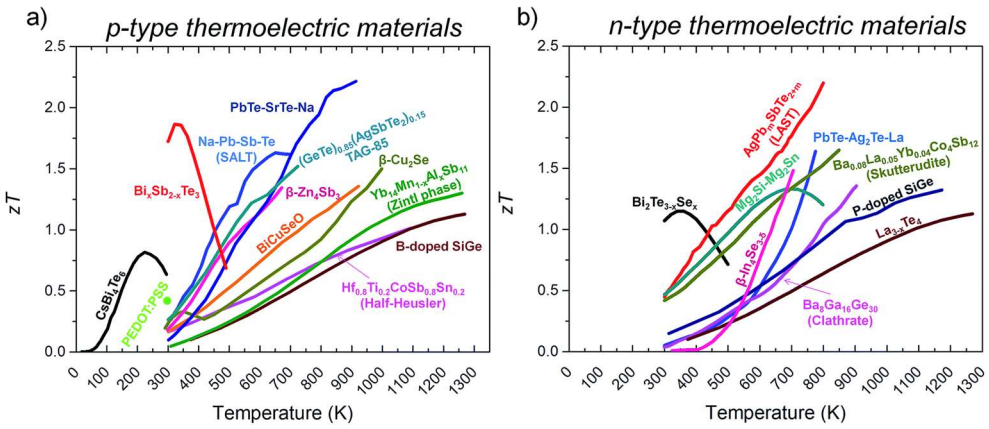

Figure 1-7 Temperature dependence of the figure-of-merit, zT, for state-of-the-art *p*-type and *n*-type thermoelectric materials.[64]

Figure 1-7 displays the temperature dependence of the figure-of-merit, zT, for the state-of-the-art *p*-type and *n*-type thermoelectric materials.[5, 64] Many of the state-of-the-art *p*-type thermoelectric materials in the temperature range from room temperature to 900 K have been well-developed and could achieve zT values over 1.0 easily and even values around 2.3 for PbTe-SrTe-Na[65] at T of ~ 900 K. When the temperature goes over 900 K, there are, however, only a few types of *p*-type thermoelectric materials that could remain stable and have high zT values. Among the latter *p*-type thermoelectric materials, β-Cu_2Se shows excellent thermoelectric performance compared to other thermoelectric materials such as Zintl phase $Yb_{14}Mn_{1-x}Al_xSb_{11}$,[66] B-doped SiGe,[67] and half-Heusler $Hf_{0.8}Ti_{0.2}CoSb_{0.8}Sn_{0.2}$.[68]

The thermoelectric materials can be mainly categorized into, but not limited to, the following types: metal chalcogenides, such as lead chalcogenides, bismuth chalcogenides, and tin chalcogonides, phonon-glass electron-crystal (PGEC) materials, such as skutterudites and clathrates, Zintl phases, and half-Heuslers, phonon-liquid electron-crystal (PLEC) materials such as $Cu_{2-x}Se$ and $Cu_{2-x}S$, silicon based materials such as SiGe alloys, and oxides.

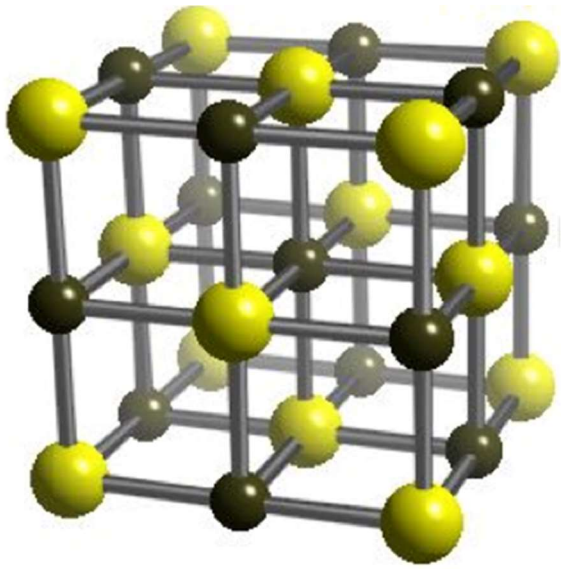

Figure 1-8 Typical crystal structure for the PbQ (Q = S, Se, Te) thermoelectric materials. Pb and S/Se/Te atoms are depicted by grey and yellow spheres, respectively.

Lead chalcogenide thermoelectric materials PbQ (Q = S, Se, Te)[69-71] show excellent thermoelectric performance in the medium temperature range from room temperature to 900 K and have been investigated for more than 60 years.[71, 72] Furthermore, they can become *n*-type and *p*-type thermoelectric materials depending on the doping elements and levels. Lead chalcogenides have typical NaCl (rock salt) crystal structures (Figure 1-8) and narrow band gaps at room temperature with energy gaps, E_g, around 0.32 eV for pure PbTe, 0.27eV for pure PbSe, and 0.37 eV for pure PbS.

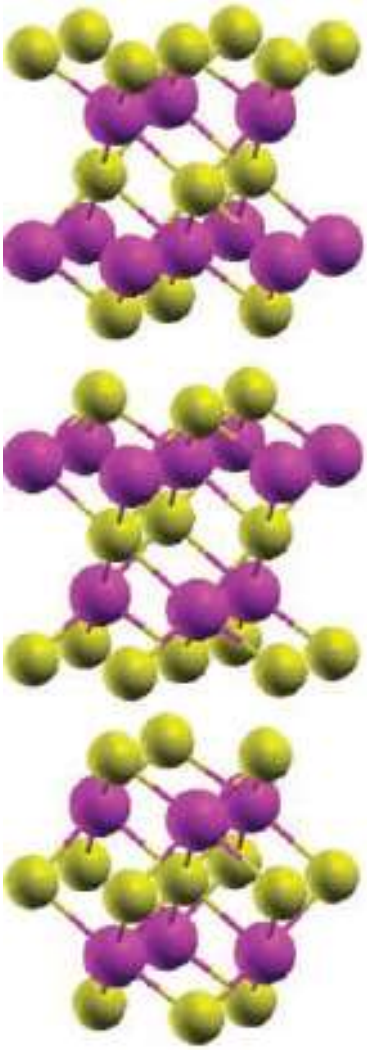

Figure 1-9 Typical crystal structure for the Bi_2Q_3 (Q = Se, Te) thermoelectric materials. Bi and S/Se/Te atoms are depicted by purple and yellow spheres, respectively.

Bi_2Q_3 (Q = Se, Te) based thermoelectric materials [73-75] have been proven to be the best commercial thermoelectric materials near room temperature. Figure 1-9 shows the typical crystal structure for Bi_2Q_3 (Q = Se, Te) based thermoelectric materials. It indicates that they have a layered rhombohedral crystal structure with space group $R\bar{3}m$. Pure Bi_2Te_3 has a band gap of 0.21 eV, and the un-doped Bi_2Se_3 has a band gap of 0.332 ± 0.055 eV.

Figure 1-10 shows the typical crystal structure for cubic structured SnTe. It should be noted that lead-free thermoelectric materials have become more and

more desirable, owing to the growing perception of the toxicity of lead. Among all the lead-free thermoelectric materials applied in the temperature interval from 600 to 900 K, the SnTe based compounds have received particularly great attention owing to the fact that SnTe has a similar crystal structure and band structure to the well-known PbTe.[62, 76-79]

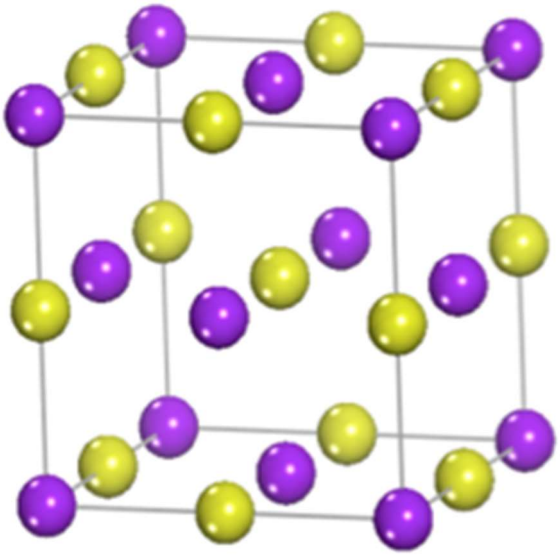

Figure 1-10 Crystal structure of cubic structured SnTe. Sn and Te atoms are depicted by purple and yellow spheres, respectively.

The concept of phonon-glass electron-crystal (PGEC) was first put forward by Slack[80] to describe the ideal that thermoelectric materials should achieve glass-like lattice thermal conductivity but crystal-like electron transport. One new idea Slack proposed is to reduce phonon thermal conductivity by the so called “phonon rattlers”. Two representative classes of materials that have received attention are skutterudites and clathrates.

Skutterudite is a type of arsenide mineral that was first discovered in Norway in 1845. Its composition is $CoAs_3$, with iron or nickel substituting for cobalt. Its general formula is TPn_3, where T is a transition metal and Pn is a pnictogen. Oftedal was the

first to describe its structure in 1928 as a cubic structure containing 32 atoms with space group $Im\bar{3}$. The unit cell consists of eight cubes of the transition metal (T = Co, Rh, or Ir) occupying the 8c sites (¼, ¼, ¼), with six of these cubes filled with square planar rectangles of the pnictogen (Pn = Sb, As, or P) occupying the 24g (0, y, z) sites.

Clathrates are another class of compound which has open structures to host loosely bound guest atoms. Clathrates typically have a large number of atoms in the unit cell and generally have low thermal conductivity, which is comparable to that of amorphous germanium. There are two types of clathrate materials. Type I are the more common and typical clathrates materials. Type I clathrates can be represented by $X_2Y_6E_{46}$, where X and Y are guest atoms encapsulated in two different cages and E is Si, Ge, or Sn.

Zintl phase thermoelectric materials are made up of electropositive cations (typically, Group I and II), which donate their electrons to electronegative anions; the anions, in turn, use them to form bonds in order to satisfy valence. The structural requirements of Zintl phases are explained by assuming the presence of both ionic and covalent contributions to the bonding picture of the structure. Classical Zintl phases are considered to be valence precise semiconductors. In a Zintl phase the Zintl anions provide the "electron-crystal" electronic structure through a covalently bonded network of complex anions or metalloids.

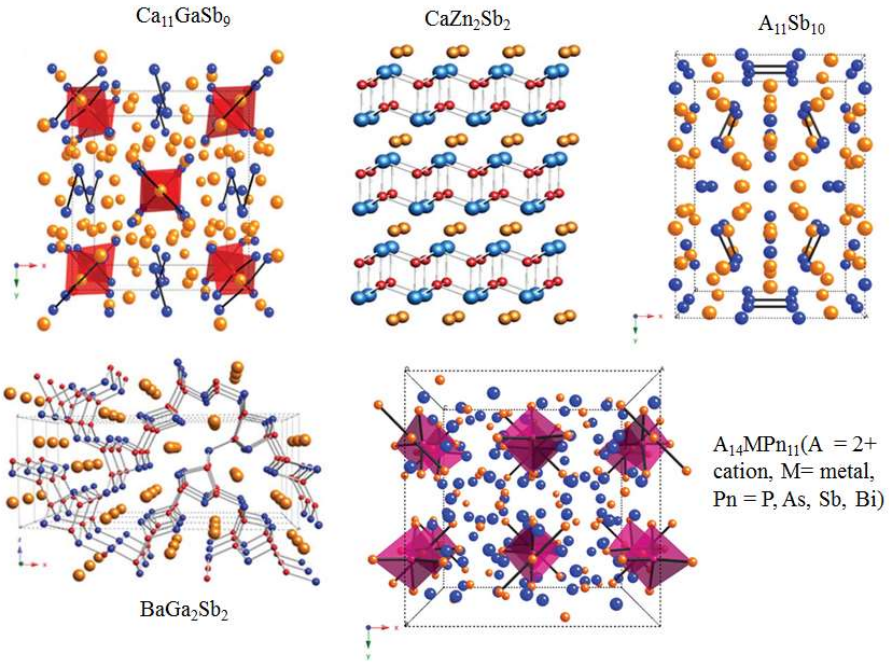

Figure 1-11 Typical crystal structures for the Zintl phase thermoelectric materials.[81]

Figure 1-11 shows the crystal structures for several typical Zintl phase thermoelectric materials. $Ca_{11}GaSb_9$, $CaZn_2Sb_2$, and $BaGa_2Sb_2$ are typical examples of Zintl phases containing antimony. These compounds are all semiconductors, and the bonding can be described via the Zintl formulism as consisting of electropositive cations and complex anions ($Ca_{11}GaSb_9$), a layered net ($CaZn_2Sb_2$), or an open framework or tunnel structure ($BaGa_2Sb_2$). Additionally, binary Zintl compounds containing Group I or II cations can also form complex structures providing phonon-glass qualities. A good example is the $A_{11}Sb_{10}$ structure type which can be described by the Zintl formulism as containing 44 A^{2+} cations with 2 $[Sb_4]^4$ squares, 8 $[Sb_2]^4$ dumbbells, and 16 Sb^{3-}anions in each unit cell. Furthermore, $A_{14}MPn_{11}$, where A is a heavy or alkaline earth metal, M is a transition or main group metal, and Pn is a heavier Group XV element (P, As, Sb, or Bi), is another type of Zintl compound. The electronic structure of the main group analogue is consistent with the Zintl formulism. The various sites allow for the potential tuning of the electronic and thermal properties through

elemental substitutions. Substituting on the cationic metal site, A, allows for possible tuning of the carrier concentration and disorder scattering of phonons, while substituting on the metal site, M, enables possible tuning of the electronic parameters.

Half-Heusler compounds possess a cubic structure consisting of three interpenetrating face-centered cubic (*fcc*) sub-lattices and one vacant sub-lattice, with high thermal stability and environmental friendliness. They exhibit promising power factors when properly doped. They also typically have a relatively high lattice thermal conductivity of ~10 $W \cdot m^{-1} \cdot K^{-1}$, which can be reduced to ~3 $W \cdot m^{-1} \cdot K^{-1}$ by alloying and nanostructuring approaches.

Oxides, a relative newcomer to the thermoelectric field, are potentially stable and chemically inert for high-temperature applications. Oxides were believed to be poor thermoelectric materials because of their low carrier mobility arising from the weak orbital overlap and localized electrons until the discoveries of good *p*-type thermoelectric properties in the layered cobaltites $NaCo_2O_4$, $Ca_4Co_3O_9$, and $Bi_2Sr_2Co_2O_9$ with large Seebeck coefficients, low thermal conductivities, and zT around 1 in the temperature range from 700 to1000 K. The most promising candidates for *n*-type oxide thermoelectric materials include perovskite-type $SrTiO_3$ and $CaMnO_3$, with rather high thermal conductivities.

1.6.2 $Cu_{2-x}X$ (X = S, Se) based thermoelectric materials

Cuprous and silver chalcogenides have a special crystal structure in which the chalcogen anions form a rigid crystalline lattice and the cuprous/silver cations are highly disordered in the rigid sub-lattice. These materials exhibit extremely low thermal conductivity and are categorized as phonon-liquid electron-crystals (PLEC) materials due to the liquid-like behavior of the cuprous

and silver cations.

At room temperature, α-Cu_2Se is monoclinic structured, and it then becomes cubic structured β-Cu_2Se with the phase transition temperature around 400 K.[82, 83] Similar to stoichiometric Cu_2Se, the stoichiometric compound Cu_2S possesses two phase-transitions.[84] One is at about 370 K, and the other is around 700 K. Below 370 K, it is called low chalcocite γ–phase (L-chalcocite). The second phase occurs between 370 K and 700 K, and is called high chalcocite β–phase (H-chalcocite). Above 700 K, Cu_2S is transformed to α–phase with an *fcc* cubic structure.

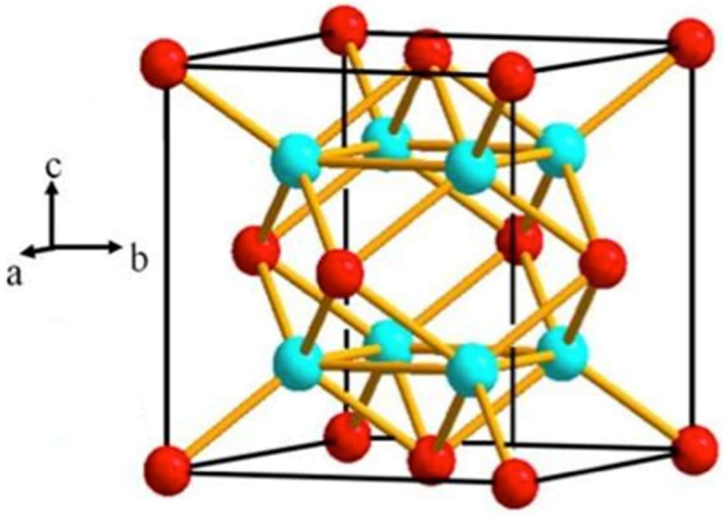

Figure 1-12 Ideal unit cell for the cubic structured Cu_2X (X = S, Se). Cu and S/Se atoms are depicted by blue and red spheres, respectively.

Figure 1-12 displays the ideal unit cell for cubic structured Cu_2X (X = S, Se). It indicates that high temperature β-phase Cu_2Se and α-phase Cu_2S are crystallized as a cubic structure with space group $Fm\bar{3}m$. The Se/S atoms form a rigid face-centred cubic (*fcc*) sub-lattice, while the Cu atoms occupy the tetrahedral interstitial positions in the ideal unit cell.

β-Cu_2Se and α-phase Cu_2S were proved to be excellent thermoelectric materials by L. D. Chen and G. J. Snyder's group[85-88] in 2012 and 2014, respectively. Furthermore, they also have several advantages, such as simple crystal structure and formula, earth-abundant elements, super-ionic conductivity, and non-sensitivity to oxygen, which indicates that the β-Cu_2Se and α-phase Cu_2S might be promising high temperature thermoelectric materials. Therefore, it should be fruitful to investigate how to modify the thermoelectric properties of the $Cu_{2-x}Se(S)$ system using the doping approach from the fundamentals based on first principles calculations as well as related experiments.

References

[1] F. J. DiSalvo, Thermoelectric cooling and power generation, Science 1999, 285, 703.

[2] L. E. Bell, Cooling, heating, generating power, and recovering waste heat with thermoelectric systems, Science 2008, 321, 1457.

[3] A. I. Hochbaum, R. Chen, R. D. Delgado, W. Liang, E. C. Garnett, M. Najarian, A. Majumdar, P. Yang, Enhanced thermoelectric performance of rough silicon nanowires, Nature 2008, 451, 163.

[4] J. Yang, Y. Hin-Lap, A. K. Y. Jen, Rational design of advanced thermoelectric materials, Adv. Energy Mater. 2013, 3, 549.

[5] G. J. Snyder, Toberer, E. S. , Complex thermoelectric materials, Nat. Mater. 2008, 7, 10.

[6] B. C. Sales, Smaller is cooler, Science 2002, 295, 1248.

[7] D. M. Rowe, CRC Handbook of thermoelectric, CRC Handbook of thermoelectrics, CRC press, FL 1995.

[8] D. M. Rowe, CRC hand book of thermoelectrics: macro to nano, CRC hand book of thermoelectrics: macro to nano. CRC Press, New York 2005.

[9] G. S. Nolas, J. Poon, M. Kanatzidis, Recent developments in bulk thermoelectric materials, MRS Bull. 2006, 31, 199.

[10] Y. Z. Pei, A. D. Lalonde, N. A. Heinz, X. Shi, S. Iwanaga, H. Wang, L. D. Chen, G. J. Snyder, Stabilizing the optimal carrier concentration for high thermoelectric efficiency, Adv. Mater. 2011, 23, 5674.

[11] Y. Pei, A. D. LaLonde, N. A. Heinz, G. J. Snyder, High Thermoelectric Figure of Merit in PbTe Alloys Demonstrated in PbTe-CdTe, Adv. Energy Mater. 2012, 2, 670.

[12] Y. Du, K. Cai, S. Chen, H. Wang, S. Z. Shen, R. Donelson, T. Lin, Thermoelectric fabrics: Toward power generating clothing, Sci. Rep. 2015, 5, 6411.

[13] Y. Tung, M. Cohen, Relativistic Band Structure and Electronic Properties of SnTe, GeTe, and PbTe, Phys. Rev. 1969, 180, 823.

[14] Y. Pei, A. D. LaLonde, N. A. Heinz, X. Shi, S. Iwanaga, H. Wang, L. Chen, G. J. Snyder, Stabilizing the optimal carrier concentration for high thermoelectric efficiency, Adv. Mater. 2011, 23, 5674.

[15] G. Snyder, T. Ursell, Thermoelectric efficiency and compatibility, Phys. Rev. Lett. 2003, 91, 148301.

[16] J. B. Vaney, J. Carreaud, G. Delaizir, A. Pradel, A. Piarristeguy, C. Morin, E. Alleno, J. Monnier, A. P. Gonçalves, C. Candolfi, A. Dauscher, B. Lenoir, High-temperature thermoelectric properties of Sn-doped β-As_2Te_3, Adv. Electron. Mater. 2015, 1, 1400008.

[17] S. K. Bux, R. G. Blair, P. K. Gogna, H. Lee, G. Chen, M. S. Dresselhaus, R. B. Kaner, J.-P. Fleurial, Nanostructured bulk silicon as an effective thermoelectric material, Adv. Funct. Mater. 2009, 19, 2445.

[18] C. J. Vineis, A. Shakouri, A. Majumdar, M. G. Kanatzidis, Nanostructured thermoelectrics: big efficiency gains from small features, Adv. Mater. 2010, 22, 3970.

[19] J. R. Sootsman, D. Y. Chung, M. G. Kanatzidis, New and old concepts in thermoelectric materials, Angew. Chem. Int. Ed. Engl. 2009, 48, 8616.

[20] H.-S. Kim, Z. M. Gibbs, Y. Tang, H. Wang, G. J. Snyder, Characterization of Lorenz number with Seebeck coefficient measurement, APL Mater. 2015, 3, 041506.

[21] H. J. Wu, L. D. Zhao, F. S. Zheng, D. Wu, Y. L. Pei, X. Tong, M. G. Kanatzidis, J. Q. He, Broad temperature plateau for thermoelectric figure of merit ZT>2 in phase-separated $PbTe_{0.7}S_{0.3}$, Nat. Commun. 2014, 5, 4515.

[22] J. Li, W. Liu, L. Zhao, M. Zhou, High-performance nanostructured thermoelectric materials, NPG Asia Mater. 2010, 2, 152.

[23] K. Saqr, M. Musa, Critical review of thermoelectrics in modern power generation applications, Therm Sci 2009, 13, 165.

[24] D. M. Rowe, C. M. Bhandari, Modern Thermoelectrics, Reston Publishing Co., Reston, Va., USA, 1983.

[25] C. B. Vining, CRC Handbook of Thermoelectrics (Ed. D. M. Rowe), CRC Press, Boca Raton, Fla., USA, 1995.

[26] B. A. Cook, J. L. Harringa, Solid-State Synthesis of Thermoelectric Materials, Thermoelectric Hand-book: Macro to Nano (Ed. D. M. Rowe), Boca Raton, Fla., USA, Taylor & Francis Group, LLC, 2005.

[27] M. Cutler, J. Leavy, R. Fitzpatrick, Electronic transport in semimetallic cerium sulfide, Phys. Rev. 1964, 133, A1143.

[28] A. Bulusu, D. G. Walker, Review of electronic transport models for thermoelectric materials, Superlattice Microst. 2008, 44, 1.

[29] D. K. Misra, A. Rajput, A. Bhardwaj, N. S. Chauhan, S. Singh, Enhanced power factor and reduced thermal conductivity of a half-Heusler derivative $Ti_9Ni_7Sn_8$: A bulk nanocomposite thermoelectric material, Appl. Phys. Lett. 2015, 106, 103901.

[30] B. Lange, C. Freysoldt, J. Neugebauer, Native and hydrogen-containing point defects in Mg_3N_2: A density functional theory study, Phys. Rev. B 2010, 81, 224109.

[31] D. Parker, X. Chen, D. J. Singh, High three dimensional thermoelectric performance from low dimensional bands, Phys. Rev. Lett. 2013, 110, 146601.

[32] B. Z. Sun, Z. Ma, C. He, W. Kechen, Anisotropic thermoelectric properties of layered compounds in SnX_2 (X = S, Se): A promising thermoelectric material, Phys. Chem. Chem. Phys. 2015.

[33] C. Kittel, Introduction to solid state physics, John Wiley & Sons, New York, 1996.

[34] C. L. Tien, A. Majumdar, F. M. Gerner, Microscale energy transport, Taylor & Francis, Washington, D. C. 1998.

[35] G. Chen, Nanoscale energy transport and conversion, Oxford University, New York, 2005.

[36] G. J. Snyder, T. Caillat, Using the compatibility factor to design high efficiency segmented thermoelectric generators, MRS Proceedings 2003, 793, 37.

[37] G. J. Snyder, Application of the compatibility factor to the design of segmented and cascaded thermoelectric generators, Appl. Phys. Lett. 2004, 84, 2436.

[38] T. S. Ursell, G. J. Snyder, Twenty-first international conference on thermoelectric materials ICT'02 412, IEEE, Long Beach, California, USA, 2002.

[39] A. Bhardwaj, N. S. Chauhan, D. K. Misra, Significantly enhanced thermoelectric figure of merit of p-type Mg_3Sb_2-based Zintl phase compound via

nanostructuring employing high energy mechanical milling coupled with spark plasma sintering, J. Mater. Chem. A 2015, 3, 10777.

[40] Y. Wu, Z. Wang, Y. He, A new method for calculating the thermoelectric efficiency, Chin. Phys. Lett. 2004, 21, 1848.

[41] B. W. Swanson, E. V. Somers, R. R. Heikes, Optimization of a sandwiched thermoelectric device, Journal of Heat Transfer 1961, 83, 77.

[42] L. Onsager, Reciprocal relations in irreversible processes. I, Phys. Rev. 1931, 37, 405.

[43] M. S. El-Genk, H. H. Saber, High efficiency segmented thermoelectric unicouple for operation between 973 and 300 K, Energ. Convers. Manage. 2003, 44, 1069.

[44] J. Schilz, L. Helmers, W. E. Muller, M. Niino, A local selection criterion for the composition of graded thermoelectric generators, J. Appl. Phys. 1998, 83, 1150.

[45] A. F. Ioffe, Semiconductor thermoelements, and Thermoelectric cooling, Infosearch, London, 1957.

[46] K. F. Hsu, S. Loo, F. Guo, W. Chen, J. S. Dyck, C. Uher, T. Hogan, E. K. Polychroniadis, M. G. Kanatzidis, Cubic $AgPb_{(m)}SbTe_{(2+m)}$: bulk thermoelectric materials with high figure of merit, Science 2004, 303, 818.

[47] B. Poudel, Q. Hao, Y. Ma, Y. Lan, A. Minnich, B. Yu, X. Yan, D. Wang, A. Muto, D. Vashaee, X. Chen, J. Liu, M. S. Dresselhaus, G. Chen, Z. Ren, High-thermoelectric performance of nanostructured bismuth antimony telluride bulk alloys, Science 2008, 320, 634.

[48] B. C. Sales, D. Mandrus, R. K. Williams, Filled skutterudite antimonides: A new class of thermoelectric materials, Science 1996, 272, 1325.

[49] D. R. Merrill, D. B. Moore, S. R. Bauers, M. Falmbigl, D. C. Johnson, Misfit Layer Compounds and Ferecrystals: Model Systems for Thermoelectric Nanocomposites, Materials 2015, 8, 2000.

[50] H. Wang, Y. Pei, A. D. LaLonde, G. J. Snyder, Heavily doped p-type PbSe with high thermoelectric performance: an alternative for PbTe, Adv. Mater. 2011, 23, 1366.

[51] Y. Pei, X. Shi, A. LaLonde, H. Wang, L. Chen, G. J. Snyder, Convergence of electronic bands for high performance bulk thermoelectrics, Nature 2011, 473, 66.

[52] S. N. Girard, J. He, X. Zhou, D. Shoemaker, C. M. Jaworski, C. Uher, V. P. Dravid, J. P. Heremans, M. G. Kanatzidis, High performance Na-doped PbTe-PbS thermoelectric materials: electronic density of states modification and shape-controlled nanostructures, J. Am. Chem. Soc. 2011, 133, 16588.

[53] J. P. Heremans, V. Jovovic, E. S. Toberer, A. Saramat, K. Kurosaki, A. Charoenphakdee, S. Yamanaka, G. J. Snyder, Enhancement of thermoelectric efficiency in PbTe by distortion of the electronic density of states, Science 2008, 321, 554.

[54] J. P. Heremans, B. Wiendlocha, A. M. Chamoire, Resonant levels in bulk thermoelectric semiconductors, Energy Environ. Sci. 2012, 5, 5510.

[55] C. M. Jaworski, B. Wiendlocha, V. Jovovic, J. P. Heremans, Combining alloy scattering of phonons and resonant electronic levels to reach a high thermoelectric figure of merit in PbTeSe and PbTeS alloys, Energy Environ. Sci. 2011, 4, 4155.

[56] Y. Pei, N. A. Heinz, G. J. Snyder, Alloying to increase the band gap for improving thermoelectric properties of Ag_2Te, J. Mater. Chem. 2011, 21, 18256.

[57] Y. Pei, H. Wang, Z. M. Gibbs, A. D. LaLonde, G. J. Snyder, Thermopower enhancement in $Pb_{1-x}Mn_xTe$ alloys and its effect on thermoelectric efficiency, NPG Asia Mater. 2012, 4, e28.

[58] Y. Z. Pei, H. Wang, G. J. Snyder, Band engineering of thermoelectric materials, Adv. Mater. 2012, 24, 6125.

[59] Q. Zhang, F. Cao, W. Liu, K. Lukas, B. Yu, S. Chen, C. Opeil, D. Broido, G. Chen, Z. Ren, Heavy doping and band engineering by potassium to improve the thermoelectric figure of merit in p-type PbTe, PbSe, and $PbTe_{(1-y)}Se_{(y)}$, J. Am. Chem. Soc. 2012, 134, 10031.

[60] G. Ding, J. Li, G. Gao, Band structure engineering of multiple band degeneracy for enhanced thermoelectric power factors in MTe and MSe (M = Pb, Sn, Ge), RSC Adv. 2015, 5, 91974.

[61] L.-D. Zhao, h. wu, C. Chang, D. Feng, Y. Xiao, X. Zhang, Y. Pei, L. Zheng, D. Wu, S. Gong, Y. Chen, J. He, M. Kanatzidis, Synergistically optimized electrical and thermal transport properties in SnTe via alloying high-solubility MnTe, Energy Environ. Sci. 2015, 8, 3298.

[62] G. Tan, F. Shi, S. Hao, H. Chi, L. D. Zhao, C. Uher, C. Wolverton, V. P. Dravid, M. G. Kanatzidis, Codoping in SnTe: enhancement of thermoelectric performance through synergy of resonance levels and band convergence, J. Am. Chem. Soc. 2015, 137, 5100.

[63] B. Du, Y. Saiga, K. Kajisa, T. Takabatake, Thermoelectric properties of p-type clathrate $Ba_{8.0}Ga_{15.9}Zn_ySn_{30.1}$single crystals with various carrier concentrations, Chem. Mater. 2015, 27, 1830.

[64] M.Rull-Bravo, A. Moure, J. F. Fernández, M. Martín-González, Skutterudites as thermoelectric material: revisited, RSC Adv. 2015, 5, 41653.

[65] K. Biswas, J. He, I. D. Blum, C. I. Wu, T. P. Hogan, D. N. Seidman, V. P. Dravid, M. G. Kanatzidis, High-performance bulk thermoelectrics with all-scale hierarchical architectures, Nature 2012, 489, 414.

[66] E. S. Toberer, C. A. Cox, S. R. Brown, T. Ikeda, A. F. May, S. M. Kauzlarich, G. J. Snyder, Traversing the metal-insulator transition in a zintl phase: rational enhancement of thermoelectric efficiency in $Yb_{14}Mn_{1-x}Al_xSb_{11}$, Adv. Funct. Mater. 2008, 18, 2795.

[67] G. Joshi, H. Lee, Y. Lan, X. Wang, G. Zhu, D. Wang, R. W. Gould, D. C. Cuff, M. Y. Tang, M. S. Dresselhaus, G. Chen, Z. Ren, Enhanced Thermoelectric Figure-of-Merit in Nanostructured p-type Silicon Germanium Bulk Alloys, Nano Lett 2008, 8, 4670.

[68] X. Yan, W. Liu, H. Wang, S. Chen, J. Shiomi, K. Esfarjani, H. Wang, D. Wang, G. Chen, Z. Ren, Stronger phonon scattering by larger differences in atomic mass and size in p-type half-Heuslers $Hf_{1-x}Ti_xCoSb_{0.8}Sn_{0.2}$, Energy Environ. Sci. 2012, 5, 7543.

[69] Q. Zhang, E. K. Chere, K. McEnaney, M. Yao, F. Cao, Y. Ni, S. Chen, C. Opeil, G. Chen, Z. Ren, Enhancement of thermoelectric performance of n-type PbSe by Cr doping with optimized carrier concentration, Adv. Energy Mater. 2015, 5, n/a.

[70] S. A. Yamini, D. R. G. Mitchell, Z. M. Gibbs, R. Santos, V. Patterson, S. Li, Y. Z. Pei, S. X. Dou, G. Jeffrey Snyder, Heterogeneous distribution of sodium for high thermoelectric performance of p-type multiphase lead-chalcogenides, Adv. Energy Mater. 2015, n/a.

[71] D. Wu, L.-D. Zhao, X. Tong, W. Li, L. Wu, Q. Tan, Y. Pei, L. Huang, J.-F. Li, Y. Zhu, M. Kanatzidis, J. He, Superior thermoelectric performance in PbTe-PbS pseudo-binary: extremely low thermal conductivity and modulated carrier, Energy Environ. Sci. 2015, 8, 2056.

[72] Q. Zhang, F. Cao, K. Lukas, W. Liu, K. Esfarjani, C. Opeil, D. Broido, D. Parker, D. J. Singh, G. Chen, Z. Ren, Study of the thermoelectric properties of lead

selenide doped with boron, gallium, indium, or thallium, J. Am. Chem. Soc. 2012, 134, 17731.

[73] Q. Zhang, X. Ai, L. Wang, Y. Chang, W. Luo, W. Jiang, L. Chen, Improved thermoelectric performance of silver nanoparticles-dispersed Bi_2Te_3 composites deriving from hierarchical two-phased heterostructure, Adv. Funct. Mater. 2015, 25, 966.

[74] X. Yan, B. Poudel, Y. Ma, W. S. Liu, G. Joshi, H. Wang, Y. Lan, D. Wang, G. Chen, Z. F. Ren, Experimental studies on anisotropic thermoelectric properties and structures of *n*-type $Bi_2Te_{2.7}Se_{0.3}$, Nano Lett. 2010, 10, 3373.

[75] J. Koenig, M. Winkler, T. Dankwort, A. Hansen, H. Pernau, V. Duppel, M. Jaegle, K. Bartholome, L. Kienle, W. Bensch, Thermoelectric efficiency of $_{(1-x)}$(GeTe)$_x$(BiSeTe) and implementation into highly performing thermoelectric power generators, Dalton Trans. 2014, 44, 2835.

[76] C. I. Okoye, Electronic and optical properties of SnTe and GeTe, J. Phys.: Condens. Matter 2002, 14, 8625.

[77] C. W. Li, J. Ma, H. B. Cao, A. F. May, D. L. Abernathy, G. Ehlers, C. Hoffmann, X. Wang, T. Hong, A. Huq, O. Gourdon, O. Delaire, Anharmonicity and atomic distribution of SnTe and PbTe thermoelectrics, Phys. Rev. B 2014, 90.

[78] J. He, J. Xu, G. Liu, X. Tan, H. Shao, Z. Liu, J. Xu, J. Jiang, H. Jiang, Enhanced power factor in promising thermoelectric material $SnPb_xTe$ prepared via zone-melting, RSC Adv. 2015, 5, 59379.

[79] K. Hoang, S. D. Mahanti, M. G. Kanatzidis, Impurity clustering and impurity-induced bands in PbTe-, SnTe-, and GeTe-based bulk thermoelectrics, Phys. Rev. B 2010, 81.

[80] G. A. Slack, CRC handbook of thermoelectrics edited by Rowe, David Michael, CRC Press, 1995.

[81] S. M. Kauzlarich, S. R. Brown, G. J. Snyder, Zintl phases for thermoelectric devices, Dalton Trans 2007, 2099.

[82] Z. Ogorelec, On the relation between electrical conductivity and phase transition of non-stoichiometric cupporus selenides, J. Phys. Chem. Solids 1969, 30, 149.

[83] B. Celustka, Z. Ogorelec, Evaluation of some physical quantifies in the two phase region in cuprous selenide, J. Phys. Chem. Solids 1971, 32, 1449.

[84] D. J. chakrabari, D. E. Laughlin, The Cu-S system, Bulletin of alloys phase diagrams 1983, 4, 254.

[85] H. Liu, X. Shi, F. Xu, L. Zhang, W. Zhang, L. Chen, Q. Li, C. Uher, T. Day, G. J. Snyder, Copper ion liquid-like thermoelectrics, Nat. Mater. 2012, 11, 422.

[86] Y. He, T. Day, T. Zhang, H. Liu, X. Shi, L. Chen, G. J. Snyder, High thermoelectric performance in non-toxic earth-abundant copper sulfide, Adv. Mater. 2014, 26, 3974.

[87] H. Liu, X. Shi, M. Kirkham, H. Wang, Q. Li, C. Uher, W. Zhang, L. Chen, Structure-transformation-induced abnormal thermoelectric properties in semiconductor copper selenide, Materials Letters 2013, 93, 121.

[88] H. Liu, Y. He, X. Shi, X. Guo, L. Chen, Recent progress in “phonon-liquid” thermoelectric materials, Chinese Science Bulletin (Chinese Version) 2013, 58, 2603.

CHAPTER 2

2 EXPERIMENTAL METHODS

2.1 Materials fabrication

2.1.1 Solid state reaction

The solid state reaction, also called a dry media reaction, is a chemical reaction without the presence of any solvents for fabricating new compounds from raw materials. It has several advantages such as low cost and environmental friendliness because of the elimination of solvents.

Generally, in a typical solid state reaction process, the raw materials are first mixed together in a mortar by hand. Sometimes, the mixed raw materials need to undergo a first heat treatment (calcination). The mixed raw or calcined materials are then sintered at high temperatures in a furnace to react completely and form new compounds.

In this thesis, the raw materials were first mixed together in an agate mortar by hand. They were then pressed into pellets using a stainless steel die and table press. Finally, the mixed raw materials were sealed in evacuated quartz tubes by an oxyacetylene torch, and heated to 873 K for 10 h to form the desired compounds.

2.1.2 Melt-quenching approach

It is well known that highly dense polycrystalline thermoelectric bulks are commonly synthesized by the hot pressing or spark plasma sintering (SPS) method under high temperature and high pressure. The hot-pressing and SPS systems are, however, quite expensive, and long heat treatments are needed to obtain high quality polycrystalline bulk samples. This, to some extent, makes thermoelectric materials less suitable for practical applications. Therefore, it is much more attractive to find an effective fabrication method that is low-cost and time-saving.

Here, we proposed to achieve highly dense samples for certain types of thermoelectric compound by employing a low-cost and time-saving method based on the following facts and analyses: Materials possessing the congruent melting property should maintain the same chemical phase and composition from the homogeneous melt state to the solid state, despite subtle differences in the real chemical compositions of the solid and melt states due to possible loss of volatile element(s) above the melting temperature.[1, 2] This means that highly dense bulks should be easily obtained by the melt-quenching approach. This has been successfully adopted for single crystal growth [3, 4] and casting technology for various materials, giving high density and excellent performance, although little work has been done on the fabrication of polycrystalline thermoelectric materials.

In this thesis, the highly dense thermoelectric bulk samples were synthesized by the proposed melt-quenching method. Firstly, the polycrystalline materials fabricated by the solid state reaction were crushed into small pieces. Secondly, they were sealed in evacuated quartz tubes again. Thirdly, the sealed materials were heated using the oxyacetylene torch (or heated to 1373 to 1473 K (depending on the composition of the polycrystalline bulks) for 10 minutes to melt completely, and then quenched in water (or subjected to furnace cooling) to obtain highly dense polycrystalline bulks.

2.2 Materials characterization

2.2.1 X-ray Powder Diffraction (XRD)

X-ray powder diffraction (XRD) is a rapid analytical technique revealing information on the crystallographic structure (lattice parameters) and phase

identification (chemical composition) of crystalline materials. Finely ground and homogenized powders are needed for XRD experiments.

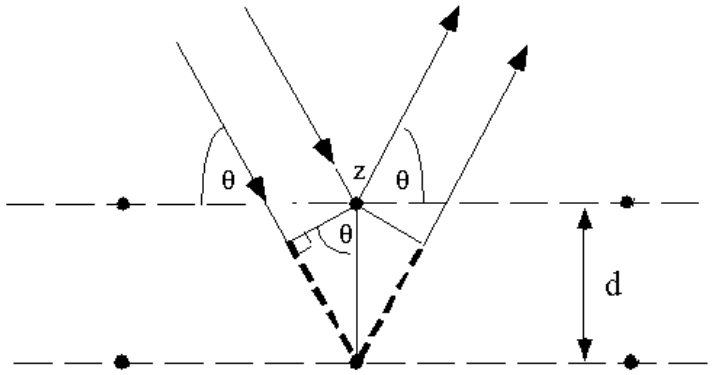

Figure 2-1 Derivation of Bragg's law.

X-ray diffraction is based on constructive interference of monochromatic X-rays and a crystalline sample. These X-rays are generated by a cathode ray tube, filtered to produce monochromatic radiation, collimated to concentrate them, and directed toward the sample. The interaction of the incident rays with the sample produces constructive interference (and a diffracted ray) when the conditions satisfy Bragg's law, as displayed in Figure 2-1 and Equation 2-1,

$$n\lambda = 2dsin\theta \qquad (2\text{-}1)$$

where d, θ, n and λ are the spacing between diffracting planes, the incident angle, an integer representing the order of the diffraction peak, and the wavelength of the beam, respectively. This law relates the wavelength of electromagnetic radiation to the diffraction angle and the lattice spacing in a crystalline sample. These diffracted X-rays are then detected, processed, and counted. All possible diffraction directions of the lattice should be attained due to the random orientation of the powdered sample, by scanning the sample through a wide range of 2θ angles. Conversion of the diffraction

peaks to *d*-spacings allows identification of the mineral because each mineral has a set of unique *d*-spacings. Typically, this is achieved by comparison of the *d*-spacings with standard reference patterns.

In this thesis, the XRD experiments for all the fabricated samples were performed on a GBC MMA diffractometer, shown in Figure 2-2, with a Cu-Kα radiation source (λ = 0.154 nm). Typically, diffraction data was collected in the 2θ range from 10 to 80° with a step width of 0.02º.

Figure 2-2 X-ray diffraction instrument (Model: GBC MMA).

2.2.2 Scanning Electron Microscopy (SEM)

The scanning electron microscope (SEM) uses a focused beam of high-energy electrons to generate a variety of signals at the surface of solid specimens. The signals derived from electron-sample interactions reveal information about the sample, such as external morphology (texture), chemical composition, and the crystalline structure and orientation of the materials making up the sample. In most applications, data are collected over a selected area of the surface of the sample, and a two-dimensional image is generated that displays spatial variations in these properties.

Accelerated electrons in an SEM carry significant amounts of kinetic energy, and this energy is dissipated as a variety of signals produced by electron-sample interactions when the incident electrons are decelerated in the solid sample. These signals include secondary electrons (which produce SEM images), backscattered electrons (BSE), diffracted backscattered electrons (EBSD), photons, visible light, and heat. Secondary electrons and backscattered electrons are commonly used for imaging samples: secondary electrons are most valuable for showing the morphology and topography of samples, and backscattered electrons are most valuable for illustrating contrasts in composition in multiphase samples (i.e. for rapid phase discrimination). SEM analysis is considered to be "non-destructive"; that is, X-rays generated by electron interactions do not lead to volume loss of the sample, so it is possible to analyse the same materials repeatedly.

Figure 2-3 Field emission scanning electron microscope (FESEM) (Model: JSM-7500FA).

In this thesis, the morphology and structure of fabricated bulk samples were obtained by using a field emission scanning electron microscope (FESEM) model JSM-7500FA, shown in Figure 2-3. The JSM-7500F is an ultra-high resolution FESEM

equipped with a high brightness conical field emission (FE) gun and a low aberration conical objective lens (semi-in-lens).

The improved overall stability of the JSM-7500F makes it possible to readily observe specimens at magnifications up to ×1,000,000 with the guaranteed resolution of 1 nm. The energy filter makes it possible to observe the fine surface morphology of nanostructures.

2.2.3 Energy-dispersive X-ray spectroscopy (EDS)

Energy dispersive X-ray spectroscopy (EDS) is an analytical capability that can be coupled with several applications, including scanning electron microscopy (SEM), transmission electron microscopy (TEM), and scanning transmission electron microscopy (STEM). EDS, when combined with these imaging tools, can be used to obtain information on the element distributions or chemical characterization of sample areas as small as nanometers in diameter. The impact of the electron beam on the sample produces X-rays that are characteristic of the elements present on the sample. EDS analysis can be used to determine the elemental composition of individual points or to map out the lateral distribution of elements from the imaged area.

The accuracy of the EDS spectrum can be affected by various factors. Many elements will have overlapping peaks (e.g., Ti K_β and V K_α, Mn K_β and Fe K_α). The accuracy of the spectrum can also be affected by the nature of the sample. X-rays can be generated by any atom in the sample that is sufficiently excited by the incoming beam. These X-rays are emitted in any direction, so they may not all escape the sample. The likelihood of an X-ray escaping the specimen and thus being available for detection and measurement depends on the energy and the amount of X-rays, as well as density of the

material that they have to pass through. This can result in reduced accuracy in inhomogeneous and rough samples.

An EDS system is composed of three basic components: the X-ray detector, the pulse processor, and the analyser. These three components must be designed to work together to achieve optimum results. In practice, the X-ray detector first detects and converts X-rays into electronic signals. Then, the pulse processor measures the electronic signals to determine the energy of each X-ray detected. Finally, the analyser displays and interprets the X-ray data.

In this thesis, all EDS analyses for fabricated samples were carried out using the supplied EDS system coupled with the JEOL-7500A FESEM system.

2.2.4 Differential scanning calorimetry (DSC)

Differential scanning calorimetry (DSC) is a thermoanalytical technique in which the difference in the amount of heat required to increase the temperature of a sample and a reference is measured as a function of temperature. Both the sample and the reference are maintained at nearly the same temperature throughout the experiment. Generally, the temperature program for a DSC analysis is designed such that the sample holder temperature increases linearly as a function of time. The reference sample should have a well-defined heat capacity over the range of temperatures to be scanned.

The main application of DSC is in studying phase transitions, such as melting points, glass transitions, crystallization times and temperatures, heats of melting and crystallization, percent crystallinity, compositional analysis, thermal stability, and heat capacity.

Based on the operating mechanism, DSCs can be classified into two types, heat-flux DSCs and power-compensated DSCs. For the heat flux DSC, the sample material,

enclosed in a pan, and an empty reference pan are placed on a thermoelectric disk surrounded by a furnace. The furnace is heated at a linear heating rate, and the heat is transferred to the sample and reference pan through the thermoelectric disk. [5, 6] Owing to the heat capacity (C_p) of the sample, however, there would be a temperature difference between the sample and the reference pans, which is measured by area thermocouples, and the consequent heat flow is determined by the thermal equivalent of Ohm's law: $\boldsymbol{q} = \Delta T/R$, where q is the "sample heat flow", ΔT is the "temperature difference between sample and reference", and R is the "resistance of the thermoelectric disk". [6, 7]

Figure 2-4 Differential scanning calorimetry (DSC) device (Model: Netzsch 204F1).

Figure 2-5 Differential scanning calorimetry (DSC) device (Model: TA Q100).

In a power-compensated DSC, the sample and reference pans are placed in separate furnaces heated by separate heaters. The sample and reference are maintained

at the same temperature, and the difference in thermal power required to maintain them at the same temperature is measured and plotted as a function of temperature or time.[5, 7, 8]

In this thesis, the measurements of specific heat for all fabricated samples were performed by using heat flux DSC instruments, the Netzsch 204F1 (Figure 2-4) and the TA Q100 (Figure 2-5).

2.2.5 Electrical conductivity and Seebeck coefficient measurements

The measurements for the electrical conductivity and Seebeck coefficient were conducted simultaneously by means of a static DC method using an Ozawa Rz2001i system (Figure 2-6) within the temperature range from 300 to 1000 K. The electrical conductivity is measured using the four point method.

Figure 2-6 System used to measure the high temperature electrical conductivity and Seebeck coefficient (Model: Rz2001i).

To prevent oxidation or oxidising, the measurements were conductede under vacuum throughout the whole process. The fabricated samples were cut and polished into rectangular bars with a cross-section of 1 mm-2mm × 2mm-5mm, and then two

parallel platinum wires were wrapped around the sample to tap the voltage for the conductivity measurements.

2.2.6 Thermal conductivity measurements

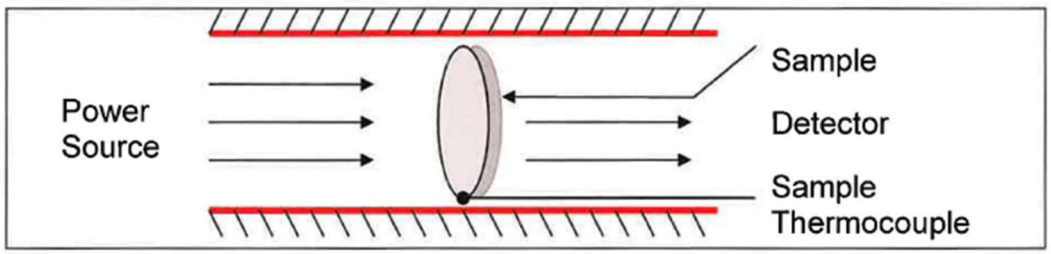

Figure 2-7 Schematic diagram illustrating the determination of thermal diffusivity.

As shown in Figure 2-7, a small thin disc-shaped specimen is subjected to a high-intensity short-duration radiant energy pulse. The energy of the pulse is absorbed on the front surface of the specimen, and the resulting rear face temperature rise (thermogram) is recorded. The thermal diffusivity value is calculated from the specimen thickness and the time required for the rear face temperature rise to reach a certain percentage of its maximum value. When the thermal diffusivity of the sample is to be determined over a temperature range, the measurement must be repeated at each temperature of interest.

The laser flash method is by far the most common technique, used 80% of the time. For measuring thermal conductivity, the following parameters are required: thermal diffusivity α , specific heat C_p, and density ρ as a function of temperature. The following formula shows this relation:

$$\lambda(\mathrm{T}) = \alpha(\mathrm{T}) \cdot C_p(\mathrm{T}) \cdot \rho(\mathrm{T}) \qquad (2\text{-}2)$$

For adiabatic conditions, α is determined by the following equation:

$$\alpha = 0.1388 \cdot I^2 / t_{0.5} \qquad (2\text{-}3)$$

where α is the thermal diffusivity in cm^2/s, I is the thickness of the test specimen in cm, and $t_{0.5}$ is the time at 50% of temperature increase measured at the rear of the specimen in seconds.

The advantage of the described method is the replacement of such parameters as absolute temperature increase and/or heat quantity by a much faster and more accurate parameter, the relative temperature increase.

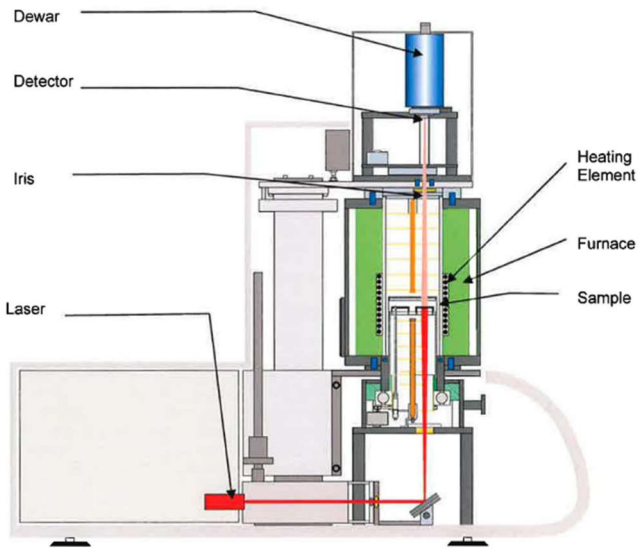

Figure 2-8 Schematic diagram illustrating the thermal diffusivity measurement system (Model: LFA 1000).

In this thesis, the thermal diffusivity data for all fabricated samples was obtained from the Linseis LFA 1000 system (Figure 2-8) under vacuum conditions in the temperature range from 300 K to 1000 K with a heating/cooling gradient of 50 K.

2.3 Density Functional Theory Calculations

Density functional theory (DFT) is computational quantum mechanical modelling method, which has been successfully used in physics, chemistry, and materials science to investigate the electronic structure of many-body systems. By using DFT, the

properties of a many-electron system can be determined by using functions of another function, which is the spatial dependent electron density. DFT is one of the most popular and versatile methods used in condensed-matter physics, computational physics, and computational chemistry.

2.3.1 Derivation of density functional theory

In many-body electronic structure calculations, the nuclei of the treated molecules or clusters are considered as fixed, generating a static external potential *V* in which the electrons are moving. A stationary electronic state is then described by a wavefunction $\Psi(\overrightarrow{r_1}, \dots, \overrightarrow{r_N},)$ satisfying the many-electron time-independent Schrödinger equation:

$$\hat{H}\Psi = [\hat{\boldsymbol{T}} + \hat{\boldsymbol{V}} + \hat{\boldsymbol{U}}]\Psi = \left[\sum_{i}^{N}\left(-\frac{\hbar^2}{2\boldsymbol{m_i}}\boldsymbol{\nabla_i^2}\right) + \sum_{i}^{N}\boldsymbol{V}(\overrightarrow{\boldsymbol{r_i}}) + \sum_{i<j}^{N}\boldsymbol{U}(\overrightarrow{\boldsymbol{r_i}}, \overrightarrow{\boldsymbol{r_j}})\right]\Psi = E\Psi \tag{2-4}$$

where, for the *N*-electron system, $\hat{H}$ is the Hamiltonian, *E* is the total energy, $\hat{T}$ is the kinetic energy, $\hat{V}$ is the potential energy from the external field due to positively charged nuclei, and $\hat{U}$ is the electron-electron interaction energy. It should be noted that $\hat{T}$ and $\hat{U}$ are universal operators, having the same vaue for any *N*-electron system, while the $\hat{V}$ is system dependent. This complicated many-particle equation cannot be separated into simpler single-particle equations because of the interaction term of $\hat{U}$.

The simplest method for solving the many-body Schrödinger equation based on the expansion of the wave-function in Slater determinants is the Hartree-Fock method, and the other sophisticated approaches are usually categorized as post-Hartree-Fock

methods. The problem with these methods is the huge computational effort, making it virtually impossible to apply them efficiently to larger and more complex systems.

DFT provides an appealing alternative because it could systematically map the many-body problem, with $\hat{U}$, onto a single-body problem without $\hat{U}$. In DFT, the key variable is the particle density, $n(\vec{r})$, which for a normalized Ψ is given by Equation 2-5.

$$n(\vec{r}) = N \int d^3r_2 \dots \int d^3r_N \Psi^*(\vec{r}, \overrightarrow{r_2}, \dots, \overrightarrow{r_N}) \Psi(\vec{r}, \overrightarrow{r_2}, \dots, \overrightarrow{r_N}) \quad (2\text{-}5)$$

This relation can be reversed, i.e., for a given ground-state density $n_0(\vec{r})$, it is possible, in principle, to calculate the corresponding ground-state wavefunction $\Psi_0(\vec{r}, \overrightarrow{r_2}, \dots, \overrightarrow{r_N})$. In other words, Ψ is a unique functional of n_0,[9] $\Psi_0 = \Psi_0[n_0]$ and consequently the ground-state expectation value of an observable $\hat{O}$ is also a functional of n_0 (Equation 2-6).

$$O[n_0] = \langle \Psi[n_0] | \hat{O} | \Psi[n_0] \rangle \quad (2\text{-}6)$$

In particular, the ground-state energy is a functional of n_0,

$$E_0 = E[n_0] = \langle \Psi[n_0] | \hat{T} + \hat{V} + \hat{U} | \Psi[n_0] \rangle \quad (2\text{-}7)$$

where the contribution of the external potential $\langle \Psi[n_0] | \hat{V} | \Psi[n_0] \rangle$ can be written explicitly in terms of the ground-state density n_0, $V[n_0] = \int V(\vec{r}) n_0(\vec{r})\, d^3r$. More generally, the contribution of the external potential $\langle \Psi | \hat{V} | \Psi \rangle$ can be written explicitly in terms of the density *n*, $V[n] = \int V(\vec{r}) n(\vec{r}) d^3r$. The functionals $T[n]$ and $U[n]$are called universal functionals, while $V[n]$ is called a non-universal functional, as it depends on the system under study. Having specified a system, i.e., having specified $\hat{V}$, one then has to minimize the functional, $E[n] = T[n] + U[n] + \int V(\vec{r}) n(\vec{r}) d^3r$, with respect to

$n(\vec{r})$, assuming one has got reliable expressions for $T[n]$ and $U[n]$. A successful minimization of the energy functional will yield the ground-state density n_0 and thus all other ground-state observables.

The variational problems of minimizing the energy functional $E[n]$ can be solved by applying the Lagrangian method of undetermined multipliers.[10] First, one considers an energy functional that does not explicitly have an electron-electron interaction energy term,

$$E_s[n] = \langle \Psi_s[n] | \hat{T} + \hat{V}_s | \Psi_s[n] \rangle \tag{2-8}$$

where $\hat{T}$ denotes the kinetic energy operator and $\hat{V}_s$ is an external effective potential in which the particles are moving, so that $n_s(\vec{r}) \stackrel{\text{def}}{=} n(\vec{r})$. Thus, one can solve the so-called Kohn-Sham equations of this auxiliary non-interacting system,

$$\left[-\frac{\hbar^2}{2m}\nabla^2 + V_s(\vec{r})\right]\emptyset_i(\vec{r}) = \epsilon_i \emptyset_i(\vec{r}) \tag{2-9}$$

which yields the orbitals $\emptyset_i$ that reproduce the density $n(\vec{r})$of the original many-body system, $n(\vec{r}) \stackrel{\text{def}}{=} n_s(\vec{r}) = \sum_i^N |\emptyset_i(\vec{r})|^2$.

The effective single-particle potential can be written in more detail as,

$$V_s(\vec{r}) = V(\vec{r}) + \int \frac{e^2 n_s(\vec{r}')}{|\vec{r}-\vec{r}'|} d^3r' + V_{XC}[n_s(\vec{r})] \tag{2-10}$$

where the second term denotes the so-called Hartree term describing the electron-electron Coulomb repulsion, while the last term V_{XC} is called the exchange-correlation potential. Here, V_{XC} includes all the many-particle interactions. Since the Hartree term and V_{XC} depend on $n(\vec{r})$, which depends on the $\emptyset_i$, which, in turn, depend on V_s, the

problem of solving the Kohn-Sham equation has to be approached in a self-consistent way.

Usually, once the initial value for $n(\vec{r})$ is given, one then can calculate the corresponding V_s and solves the Kohn-Sham equations for the $\emptyset_i$. From these, one calculates a new density and starts again. This procedure is then repeated until convergence is reached. A non-iterative approximate formulation called Harris functional DFT is an alternative approach to this.

2.3.2 Early density functional theories

2.3.2.1 The electronic density

The electronic density corresponding to a normalized *N*-electron wavefunction (with *r* and *s* denoting spatial and spin variables, respectively) is defined as, [11]

$$\rho(\vec{r}) = N \sum_{s1} \dots \sum_{sN} \int dr_2 \dots \int dr_N \, |\Psi(\vec{r}, s_1, r_1, s_2, \dots, \vec{r}_N, s_N)|^2, = \langle \Psi | \hat{\rho}(\vec{r}) | \Psi \rangle \quad (2\text{-}11)$$

where the operator corresponding to the density observable is shown in Equation2-12.

$$\hat{\rho}(\vec{r}) = \sum_{i=1}^{N} \sum_{s_i} \delta(\vec{r} - \vec{r}_i) \quad (2\text{-}12)$$

In Hartree-Fock and DFT, the wavefunction can be typically represented as a single Slater determinant constructed from *N* orbitals, φ_k, with corresponding occupations n_k. Based on these situations, the density can be simplified to Equation 2-13.

$$\rho(\vec{r}) = \sum_{k=1}^{N} n_k |\varphi_k(\vec{r})|^2 \quad (2\text{-}13)$$

It indicates that the density is a non-negative function integrating to the total number of electrons. Furthermore, for a system with kinetic energy *T*, the density should satisfy the inequalities[12] shown in Equations 2-14 and 2-15.

$$\frac{1}{2}\int dr\left(\nabla\sqrt{\rho(\vec{r})}\right)^2 \leq T \tag{2-14}$$

$$\frac{3}{2}\left(\frac{\pi}{2}\right)^{4/3}\left(\int dr\rho^3(\vec{r})\right)^{1/3} \leq T \tag{2-15}$$

For finite kinetic energies, the first inequality places the square root of the density in the Sobolev space $H^1(R^3)$. Together with the normalization and non-negativity, this defines a space containing physically acceptable densities displayed in Equation 2-16. For the second inequality, it places the density in the L^3 space with values within the intersection of L^1 and L^3 - a superset of $\mathcal{I}_N$ together with the normalization property.

$$\mathcal{I}_N = \left\{\rho\middle|\rho(\vec{r}) \geq 0, \rho^{1/2}(\vec{r}) \in H^1(R^3), \int dr\rho(\vec{r}) = N\right\} \tag{2-16}$$

2.3.2.2 The Thomas-Fermi model

The Thomas-Fermi (T-F) model, named after Llewellyn Thomas and Enrico Fermi, is a quantum mechanical theory for the electronic structure of many-body systems. T-F model is developed semiclassically shortly after the introduction of the Schrödinger equation.[13] It should be noted that T-F model is formulated in terms of the electronic density alone and is viewed as a precursor to modern density functional theory. This model is correct only in the limit of an infinite nuclear charge. For realistic systems, this approximation yields poor quantitative predictions and even fails to reproduce some general features of the density. It has, however, found modern applications in many fields through its ability to extract qualitative trends analytically and the ease with

which the model can be solved. The kinetic energy expression of T-F theory can also be used as one component of more sophisticated density approximations to the kinetic energy within modern orbital-free DFT.

Working independently, Thomas and Fermi used T-F model to approximate the electron distributions in an atom in 1927. Although electrons are distributed non-uniformly in an atom, an approximation was made that the electrons are distributed uniformly in each small volume element ΔV, but the electron density $\mathrm{n}(\vec{r})$ can still vary from one small volume element to the next.

For a small volume element ΔV, and for the atom in its ground state, a spherical momentum space volume V_f up to the Fermi momentum p_f can be filled out, and thus,

$$V_f = \frac{4}{3}\pi p_f^3(\vec{r}) \tag{2-17}$$

where $\vec{r}$ is a point in ΔV.

The corresponding phase space volume is displayed in Equation 2-18.

$$\Delta V_{ph} = V_f \Delta V = \frac{4}{3}\pi p_f^3(\vec{r})\Delta V \tag{2-18}$$

The electrons in ΔV_{ph} are distributed uniformly with two electrons per h^3 of this phase space volume, where h is Planck's constant. Then, the number of electrons in ΔV_{ph} is.

$$\Delta N_{ph} = \frac{2}{h^3}\Delta V_{ph} = \frac{8\pi}{3h^3} p_f^3(\vec{r})\Delta V \tag{2-19}$$

The number of electrons in ΔV is $\Delta N = n(\vec{r})\Delta V$, where $\mathrm{n}(\vec{r})$ is the electronic density.

Equating the number of electrons in ΔV to that in ΔV_{ph} gives

$$n(\vec{r}) = \frac{8\pi}{3h^3} p_f^3(\vec{r}) \tag{2-20}$$

The fraction of electrons at $\vec{r}$ that have momentum between *p* and *p*+*dp* is,

$$F_{\vec{r}}(p)dp = \frac{4\pi p^2 dp}{\frac{4}{3}\pi p_f^3(\vec{r})} \quad p \le p_f(\vec{r}) \tag{2-21}$$

$$= 0 \qquad \text{otherwise} \tag{2-22}$$

Based on the classical expression for the kinetic energy of an electron with mass of m_e, the kinetic energy per unit volume at $\vec{r}$ for the electrons of the atom can be estimated as,

$$t(\vec{r}) = \int \frac{p^2}{2m_e} n(\vec{r})\, F_{\vec{r}}(p)dp = n(\vec{r}) \int_0^{p_f(\vec{r})} \frac{p^2}{2m_e} \frac{4\pi p^2}{\frac{4}{3}\pi p_f^3(\vec{r})} dp = C_F[n(\vec{r})]^{5/3} \tag{2-23}$$

where a previous expression relating n($\vec{r}$) to $p_f(\vec{r})$ has been used and $C_F = \frac{3h^2}{10m_e}\left(\frac{3}{8\pi}\right)^{\frac{2}{3}}$. By integrating the kinetic energy per unit volume $t(\vec{r})$ over all space, the total kinetic energy of the electrons could be obtained as Equation 2-24.

$$T = C_F \int [n(\vec{r})]^{5/3} d^3r \tag{2-24}$$

This result indicates that the $t(\vec{r})$ can be expressed in terms of only the spatially varying electron density $n(\vec{r})$ according to the T-F model. Then, Thomas and Fermi were able to calculate the energy of an atom using this expression for the kinetic energy combined with the classical expressions for the nuclear-electron and electron-electron interactions.

The potential energy of an atom's electrons, due to the electrical attraction of the positively charged nucleus is,

$$U_{eN} = \int n(\vec{r})\, V_N(\vec{r}) d^3r \tag{2-25}$$

where $V_N(\vec{r})$ is the potential energy of an electron at $\vec{r}$ that is due to the electric field of the nucleus. For the case of a nucleus centered at $\vec{r} = 0$ with charge *Ze*, where *Z* is a positive integer and *e* is the elementary charge, $V_N(\vec{r})$ has the value of $\frac{-Ze^2}{r}$. The potential energy of the electrons due to their mutual electrical repulsion is,

$$U_{ee} = \frac{1}{2}e^2 \int \frac{n(\vec{r})n(\vec{r}')}{|\vec{r}-\vec{r}'|} d^3r d^3r' \quad (2\text{-}26)$$

Hence, the total energy of the electrons is the sum of their kinetic and potential energies,

$$E = T + U_{eN} + U_{ee} = C_F \int [n(\vec{r})]^{5/3} d^3r + \int n(\vec{r}) V_N(\vec{r})\, d^3r + \frac{1}{2}e^2 \int \frac{n(\vec{r})n(\vec{r}')}{|\vec{r}-\vec{r}'|} d^3r d^3r' \quad (2\text{-}27)$$

2.3.3 The Hohenberg-Kohn theorems

The T-F model just provides conceptual roots for the DFT, while the two Hohenberg-Kohn theorems (H-K)[9] offer a firm theoretical footing for DFT approximations. The original H-K theorems held only for non-degenerate ground states in the absence of a magnetic field, although they have since been generalized to encompass the other cases.[14, 15]

The first H-K theorem demonstrates that the ground state properties of a many-electron system are uniquely determined by an electron density that depends on only three spatial coordinates. It provide one way to reduce the many-body problem of *N* electrons with *3N* spatial coordinates to 3 spatial coordinates by using functionals of the electron density. The first H-K theorem can be extended to the time-dependent domain to develop time-dependent density functional theory (TDDFT), which can be used to describe excited states. The second H-K theorem defines an energy functional for the

system and proves that the correct ground state electron density minimizes this energy functional.

2.3.3.1 The first Hohenberg-Kohn theorem

The H-K theorems relate to any system consisting of electrons moving under the influence of an external potential $v_{ext}(\vec{r})$. In the first H-K theorem, the total energy is a unique functional of the electron density $n(\vec{r})$. The energy functional $E[n(\vec{r})]$ in the first H-K theorem can be written in terms of the external potential $v_{ext}(\vec{r})$,

$$E[n(\vec{r})] = \int n(\vec{r}) v_{ext}(\vec{r}) dr + F[n(\vec{r})] \quad (2\text{-}28)$$

where $F[n(\vec{r})]$ is an unknown, but otherwise universal, functional of the electron density $n(\vec{r})$ only. Correspondingly, a Hamiltonian for the system can be written such that the electron wavefunction Ψ that minimises the expectation value gives the ground state energy (assuming a non-degenerate ground state) as shown in Equation 2-29.

$$E[n(\vec{r})] = \langle \Psi | \hat{H} | \Psi \rangle \quad (2\text{-}29)$$

The Hamiltonian can be written as,

$$\hat{H} = \hat{F} + \hat{V}_{ext} \quad (2\text{-}30)$$

where $\hat{F}$ is the electronic Hamiltonian consisting of a kinetic energy operator $\hat{T}$ and an interaction operator $\hat{V}_{ee}$,

$$\hat{F} = \hat{V} + \hat{V}_{ee} \quad (2\text{-}31)$$

The electron operator $\hat{F}$ has the same value for all N-electron systems, therefore, $\hat{H}$ is completely determined by the number of electrons *N* and the external potential $v_{ext}(\vec{r})$.

The proof of the first H-K theorem is remarkably simple and proceeds by reductio ad absurdum. Let there be two different external potentials, $v_{ext,1}(\vec{r})$ and $v_{ext,2}(\vec{r})$, that give rise to the same density $n_0(\vec{r})$. The associated Hamiltonians, $\hat{H}_1$ and $\hat{H}_2$, will therefore have different ground state wavefunctions, $\Psi_1$and Ψ_2, that each yield $n_0(\vec{r})$. Using the variational principle, together with $\hat{F} = \hat{T} + \hat{V}_{ee}$ yields,

$$E_1^0 < \langle \Psi_2 | \hat{H}_1 | \Psi_2 \rangle = \langle \Psi_2 | \hat{H}_2 | \Psi_2 \rangle + \langle \Psi_2 | \hat{H}_1 - \hat{H}_2 | \Psi_2 \rangle$$

$$= E_2^0 + \int n_0(\vec{r}) \left[v_{ext,1}(\vec{r}) - v_{ext,2}(\vec{r}) \right] dr \qquad (2\text{-}32)$$

where E_1^0 and E_2^0 are the ground state energies of $\hat{H}_1$ and $\hat{H}_2$, respectively. It is at this point that the H-K theorems, and therefore DFT, apply rigorously to the ground state only. So adding the interchanged inequality to $F[n(r)] = \langle \psi | \hat{F} | \psi \rangle$ will lead to the following result,

$$E_1^0 + E_2^0 < E_2^0 + E_1^0 \qquad (2\text{-}33)$$

which is a contradiction, and as a result, the ground state density uniquely determines the external potential $v_{ext}(\vec{r})$, to within an additive constant. An equivalent expression for (2-33) holds when the subscripts are interchanged. Stated simply, the electrons determine the positions of the nuclei in a system and also all ground state electronic properties, because as mentioned earlier, $v_{ext}(\vec{r})$ and *N* completely define $\hat{H}$.

2.3.3.2 The second Hohenberg-Kohn theorem

The ground state energy can be obtained variationally: the density that minimises the total energy is the exact ground state density. The proof of the second H-K theorem is also straightforward: $n(\vec{r})$ determines $v_{ext}(\vec{r})$, and *N* and $v_{ext}(\vec{r})$ determine $\hat{H}$ and Ψ,

ultimately meaning that Ψ is a functional of $n(\vec{r})$, and so the expectation value of $\hat{F}$ is also a functional of $n(\vec{r})$,

$$F[n(r)] = \langle\psi|\hat{F}|\psi\rangle. \quad (2\text{-}34)$$

A density that is the ground-state of some external potential is known as v-representable. Following from this, a v-representable energy functional $E_v[n(\vec{r})]$ can be defined in which the external potential $v(\vec{r})$ is unrelated to another density $n'(\vec{r})$,

$$E_v[n(\vec{r})] = \int n'(\vec{r})\, v_{ext}(\vec{r})dr + F[n'(\vec{r})] \quad (2\text{-}35)$$

and the variational principle asserts,

$$\langle\psi'|\hat{F}|\psi'\rangle + \langle\psi'|\hat{V}_{ext}|\psi'\rangle > \langle\psi|\hat{F}|\psi\rangle + \langle\psi|\hat{V}_{ext}|\psi\rangle \quad (2\text{-}36)$$

where ψ is the wave-function associated with the correct ground state $n(\vec{r})$. This results in,

$$\int n'(\vec{r})v_{ext}(\vec{r})dr + F[n'(\vec{r})] > \int n(\vec{r})v_{ext}(\vec{r})dr + F[n(\vec{r})] \quad (2\text{-}37)$$

and therefore, the variational principle of the second H-K theorem could be obtained,

$$E_v[n'(\vec{r})] > E_v[n(\vec{r})] \quad (2\text{-}38)$$

2.3.4 The Kohn-Sham equations

In physics and quantum chemistry, specifically, density functional theory, the Kohn-Sham (K-S) equation is the Schrödinger equation of a fictitious system (the "Kohn-Sham system") of non-interacting particles (typically electrons) that generate the same density as any given system of interacting particles.[10, 11] The K-S equation is

defined by a local effective external potential in which the non-interacting particles move, typically denoted as $v_s(\vec{r})$ or $v_{eff}(\vec{r})$, called the K-S potential. As the particles in the K-S system are non-interacting fermions, the K-S wavefunction is a single Slater determinant constructed from a set of orbitals that are the lowest energy solutions to

$$\left(-\frac{\hbar^2}{2m}\nabla^2 + v_{eff}(\vec{r})\right)\emptyset_i(\vec{r}) = \varepsilon_i\emptyset_i(\vec{r}) \tag{2-39}$$

This eigenvalue equation is the typical representation of the K-S equations. Here, ε_i is the orbital energy of the corresponding K-S orbital, ϕ_i, and the density for an *N*-particle system is

$$\rho(\vec{r}) = \sum_i^N |\phi_i(\vec{r})|^2 \tag{2-40}$$

The K-S equations are named after Walter Kohn and Lu Jeu Sham, who introduced this concept at the University of California in 1965.

In K-S theory, the total energy of a system is expressed as a functional of the charge density,

$$E[\rho] = T_s[\rho] + \int dr v_{ext}(\vec{r})\rho(\vec{r}) + E_H[\rho] + E_{xc}[\rho] \tag{2-41}$$

where T_s, v_{ext} and E_H, and E_{xc} are the K-S kinetic energy, the external potential acting on the interacting system, the Hartree (or Coulomb) energy, and the exchange-correlation energy, respectively. Furthermore, T_s and E_H can be expressed as follows.

$$T_s[\rho] = \sum_{i=1}^N \int dr \phi_i^*(\vec{r})\left(-\frac{\hbar^2}{2m}\nabla^2\right)\phi_i(\vec{r}) \tag{2-42}$$

$$E_H = \frac{e^2}{2}\int dr \int dr' \frac{\rho(\vec{r})\rho(\vec{r}')}{|\vec{r}-\vec{r}'|} \tag{2-43}$$

The K-S equations are found by varying the total energy expression with respect to a set of orbitals to yield the K-Spotential as

$$v_{eff}(\vec{r}) = v_{ext}(\vec{r}) + e^2 \int \frac{\rho(\vec{r}')}{|\vec{r}-\vec{r}'|} dr' + \frac{\delta E_{xc}[\rho]}{\delta \rho(\vec{r})}, \tag{2-44}$$

where the last term，

$$v_{xc}(\vec{r}) \equiv \frac{\delta E_{xc}[\rho]}{\delta \rho(\vec{r})} \tag{2-45}$$

is the exchange-correlation potential. This term and the corresponding energy expression are the only unknowns in the K-S approach to density functional theory. An approximation that does not vary the orbitals is Harris functional theory.

The K-S orbital energies, ε_i, in general, have little physical meaning. The sum of the orbital energies is related to the total energy as

$$E = \sum_i^N \varepsilon_i - V_H[\rho] + E_{xc}[\rho] - \int \frac{\delta E_{xc}[\rho]}{\delta \rho(r)} \rho(\vec{r}) dr \tag{2-46}$$

For the more general restricted open-shell case, the orbital energies are non-unique. Therefore, this equation only holds true for specific choices of orbital energies.

2.3.5 The exchange-correlation functionals

Within the framework of K-S DFT, the intractable many-body problem of interacting electrons in a static external potential is simplified to a tractable problem of non-interacting electrons moving in an effective potential. The effective potential includes the external potential and the effects of the Coulomb interactions between the electrons, i.e., the exchange and correlation interactions. Hence, modeling the latter two interactions becomes the key point within K-S DFT.

The simplest approximation is the local-density approximation, which is based upon the exact exchange energy for a uniform electron gas, which can be obtained from the T-F model, and from fits to the correlation energy for a uniform electron gas. Non-interacting systems are relatively easy to solve, as the wavefunction can be represented as a Slater determinant of orbitals. Furthermore, the kinetic energy functional of such a system is known exactly. The exchange-correlation (XC) part of the total-energy functional, however, remains unknown and must be approximated.

2.3.5.1 Local-density approximations

Local-density approximations (LDA) are a type of approximations to the XC energy functional in DFT that depend solely upon the value of the electronic density at each point in space (and not, for example, derivatives of the density or the K-S orbitals). Many approaches can yield local approximations to the XC energy. The overwhelmingly successful local approximations, however, are those that have been derived from the homogeneous electron gas (HEG) model. In this regard, LDA is generally synonymous with functionals based on the HEG approximation and can be applied to the realistic systems such as molecules and solids.

In general, for a spin-unpolarized system, a local-density approximation for its XC energy can be estimated by the following equation

$$E_{xc}^{LDA}[\rho] = \int \rho(\vec{r})\epsilon_{xc}(\rho)dr \tag{2-47}$$

where ρ and ϵ_{xc} are the electronic density and the XC energy per particle of a HEG of charge density ρ, respectively. The XC energy can be decomposed into exchange and correlation terms linearly,

$$E_{xc} = E_x + E_c \tag{2-48}$$

so that separate expressions for E_x and E_c are sought. The exchange term takes on a simple analytic form for the HEG. Only limiting expressions for the correlation density are known exactly, therefore, there are numerous different approximations for E_c.

LDA are important in the construction of more sophisticated approximations to the exchange-correlation energy, such as the generalized gradient approximation or hybrid functionals, as a desirable property of any approximate XC functional is that it reproduces the exact results of the HEG for non-varying densities.

2.3.5.2 Generalized gradient approximation

The LDA approximates the energy of the true density by the energy of a local constant density, and it also does not work in situations where the density undergoes rapid changes, such as in molecules. The generalized gradient approximation (GGA) considering the gradient of the electron density can be considered as an improvement of the LDA. Symbolically, the GGA can be written as,

$$E_{xc} = E_{xc}[\rho(\vec{r}), \nabla\rho(\vec{r})] \quad (2\text{-}49)$$

This can lead to a large improvement over LDA results, with accuracy approaching that of correlated wavefunction methods such as MP2[16] and in some cases surpassing them.

There are several different parameterizations of the GGA. Some of them are semi-empirical, and experimental data is used in their derivation. Others are found entirely from first principles, and the PW91 functional[17] is a commonly used functional.

Perdew, Burke, and Ernzerhof developed a simplified GGA functional, Perdew-Burke-Ernzerhof (PBE) XC functional, which best fulfils many of the physical and mathematical requirements of DFT. Particularly, PBE XC functional not only satisfies the Lieb-Oxford bound[18] but also provides the correct linear response of the uniform

electron gas with proper uniform scaling.[19] Moreover, it also results in smooth pseudo-potentials.[20, 21]

In PBE XC functional, the enhancement factor of the exchange functional can be expresses as follows

$$F_x^{PBE}(s) = 1 + k - \frac{k}{\left(1+\frac{\mu}{k}s^2\right)} \tag{2-50}$$

where $k = 0.804$ is set to the maximum value allowed by the local Lieb-Oxford bound[18] on E_{xc}, and $\mu = 0.21951$ is set to recover the linear response of the uniform gas such that the effective gradient coefficient for exchange cancels that for correlation.

2.3.6 Ultra-soft pseudo-potentials

Many modern pseudo-potential calculations use a generalisation of the Kleinman-Bylander form known as ultra-soft pseudo-potentials, which attain much smoother (softer) pseudo-wavefunctions and use considerably fewer plane-waves for calculations of the same accuracy. This is achieved by relaxing the norm-conservation constraint, which offers greater flexibility in the construction of the pseudo-wavefunctions. In this scheme, the total valence density $n(\vec{r})$ is a sum of so-called hard and soft contributions,

$$n(\vec{r}) = \sum_n \left[|\phi_n(\vec{r})|^2 + \sum_{ij} Q_{ij}(\vec{r}) \langle \phi_n | \beta_j \rangle \langle \beta_j | \phi_n \rangle \right] \tag{2-51}$$

where β_i are projector functions depending on the ionic positions, and the augmentation function $Q_{ij}(\vec{r})$ is given by

$$Q_{ij}(\vec{r}) = \psi_i^*(\vec{r})\psi_j(\vec{r}) - \phi_i^*(\vec{r})\phi_j(\vec{r}) \tag{2-52}$$

where $\psi_i(\vec{r})$ and $\phi_i(\vec{r})$ are the all-electron wavefunctions and the ultra-soft

wavefunctions constructed without satisfying the norm-conservation condition $Q_{ij}(\vec{r}) = 0$, respectively. Also, the orthonormality condition takes on a generalised form,

$$\langle \phi_i | S(\{R_I\}) | \phi_j \rangle = \delta_{ij} \quad (2\text{-}53)$$

where $S(R_I)$ depends on the ionic positions through $|\beta_i\rangle$ and is defined as,

$$S = 1 + \sum_{ij} q_{ij} |\beta_j\rangle\langle\beta_i| \quad (2\text{-}54)$$

with,

$$q_{ij} = \int Q_{ij}(\vec{r}) dr \quad (2\text{-}55)$$

Typically, the cut-off energy E_{cut} when using ultrasofts is about half that of conventional norm-conserving pseudo-potentials, and for simple estimates the number of plane-waves scales as $E_{cut}^{\frac{3}{2}}$. Therefore, approximately one-third less plane waves are required in a given calculation. In this thesis, ultra-soft pseudo-potentials are used during the geometry optimizations for the considered compounds.

References

[1] G. J. Snyder, M. Christensen, E. Nishibori, T. Caillat, B. B. Iversen, Disordered zinc in Zn_4Sb_3 with phonon-glass and electron-crystal thermoelectric properties, Nat. Mater. 2004, 3, 458.

[2] A. May, J.-P. Fleurial, G. Snyder, Thermoelectric performance of lanthanum telluride produced via mechanical alloying, Phys. Rev. B 2008, 78, 125205.

[3] H. Yu, H. Zhang, Z. Wang, J. Wang, Z. Shao, M. Jiang, CW and Q-switched laser output of LD-end-pumped 1.06 μ m *c*-cut Nd : $LuV0_4$ laser, Optics Express 2007, 15, 3206.

[4] K. Wu, L. Z. Hao, H. H. Yu, Z. P. Wang, J. Y. Wang, H. J. Zhang, Thermal and laser properties of Nd : $Lu_3Sc_{1.5}Ga_{3.5}O_{12}$ for high power dual-wavelength laser, Optics Express 2012, 20, 6944.

[5] P. J. Haines, M. Reading, F. W. Wilburn, Differential thermal analysis and differential scanning calorimetry. In Brown ME (ed): Handbook of Thermal Analysis and Calorimetry, vol 1. The Netherlands: Elsevier Science BV, 1998, 279.

[6] R. L. Danley, New heat flux DSC measurement technique., Thermochim Acta 2002, 395, 201.

[7] P. Gill, T. T. Moghadam, B. Ranjbar, Differential scanning calorimetry techniques: applications in biology and nanoscience, Journal of Biomolecular Techniques 2010, 21, 167.

[8] Z. N, E. G, O. S, L. A, An analytical expression of the output of a power-compensated DSC in a wide temperature range, Thermochim Acta 2002, 143, 117.

[9] P. Hohenberg, Inhomogeneous electron gas, Phys. Rev. 1964, 136, B864.

[10] W. Kohn, L. J. Sham, Self-Consistent Equations Including Exchange and Correlation Effects, Phys. Rev. 1965, 140, A1133.

[11] R. G. Parr, W. Yang, 1989. Density-Functional Theory of Atoms and Molecules. New York: Oxford University Press. ISBN 0-19-509276-7.

[12] E. Lieb, Density functional for coulomb systems, Int. J. Quantum Chem. 1983, 24, 243.

[13] E. Schrödinger, An undulatory theory of the mechanics of atoms and molecules, Phys. Rev. 1926, 28, 1049.

[14] M. Levy, Universal variational functionals of electron densities, first-order density matrices, and natural spin-orbitals and solution of the v-representability problem, Proc. Nati. Acad. Sd. USA 1979, 76, 6062.

[15] G. Vignale, M. Rasolt, Density-functional theory in strong magnetic fields, Phys. Rev. Lett. 1987, 59, 2360.

[16] K. Kim, K. D. Jordan, Comparison of Density Functional and MP2 Calculations on the Water Monomer and Dimer, The Journal of Physical Chemistry 1994, 98, 10089.

[17] K. Burke, J. Perdew, Y. Wang, in *Electronic Density Functional Theory*, (Eds: J. Dobson, G. Vignale, M. Das), Springer US, 1998, 81.

[18] E. H. Lieb, S. Oxford, Improved lower bound on the indirect coulomb energy, Int. J. Quantum Chem. 1981, 19, 427.

[19] M. Levy, Asymptotic coordinate scalling bound for exchange-correlation energy in density-funtional theory Int. J. Quantum Chem. 1989, 36, 617.

[20] J. P. Perdew, K. Burke, M. Ernzerhof, Generalized gradient approximation made simple, Phys. Rev. Lett. 1996, 77, 3865.

[21] X. Xu, W. A. Goddard, The extended Perdew-Burke-Ernzerhof functional with improved accuracy for thermodynamic and electronic properties of molecular systems, J Chem Phys 2004, 121, 4068.

CHAPTER 3

3 STRUCTURAL, THERMOELECTRIC AND MECHANICAL PROPERTIES FOR THE $CU_{2-X}S$ BULKS

3.1 Preface

High temperature thermoelectric materials have received great attention due to their crucial roles in direct energy conversion between heat and electricity, based on the Seebeck effect[1] and Peltier effect[2]. It is well known that the energy conversion efficiency for thermoelectric devices at a temperature T can be estimated by zT, which is related to the Seebeck coefficient, absolute temperature, electrical conductivity, and total thermal conductivity.[3-7] Apparently, high zT values can be achieved with concurrent high S and σ values, and low κ values.

Recently, it has been reported that hot-pressed $Cu_{2-x}S$ polycrystalline bulks show high thermoelectric performance with the highest zT values on record, ~ 1.7 at 1000 K.[8, 9] Furthermore, $Cu_{2-x}S$ consists of copper and sulphur, both of which are naturally abundant and non-toxic. Therefore, $Cu_{2-x}S$ should be one promising high temperature thermoelectric materials. It should be noted that the polycrystalline bulks were generally fabricated by the hot pressing method using spark plasma sintering (SPS) systems under high temperature and high pressure. This approach requires costly instruments and high electrical current for SPS, and may lead to Cu migration[10], which is disadvantageous for the large-scale fabrication of homogeneous thermoelectric materials.

In addition, mechanical stress caused by the good contact between the thermoelectric modules and the heat source, and thermal stress, induced by the temperature gradient between the hot and cold sides, coexist in the interior of thermoelectric devices, which can reduce the reliability of thermoelectric modules.[11-13]

Therefore, besides the high *zT* values, thermoelectric materials should also have good mechanical properties, and it is important to investigate the mechanical properties of $Cu_{2-x}S$.

High-temperature *α*-phase $Cu_{2-x}S$ has the same cubic crystal structure (space group: $Fm\bar{3}m$)[14-16] and superionic transport[17] as $Cu_{2-x}Se$,[18, 19] which makes this family of compounds distinct from other high temperature thermoelectric materials and leads to additional considerations for their use[20]. It has been reported that hot-pressed $Cu_{2-x}S$ bulks show lower electrical conductivity than hot-pressed $Cu_{2-x}Se$ bulks,[9, 19] indicating that there may be some differences in doping or in their electronic band structures due to the differences in the lattice parameter and ionic radius of Se^{2-} and S^{2-}. Therefore, it is desirable to investigate the electronic band structure for the $Cu_{2-x}S$ system.

Herein, we report the high thermoelectric and mechanical performance of highly dense Cu_2S and $Cu_{1.97}S$ bulks prepared by a melt-solidification technique. The fabricated $Cu_{1.97}S$ bulks show *zT* values as high as ~ 1.9 at 973 K, which confirms the reported high *zT* result and is somewhat higher than that for the hot-pressed polycrystalline $Cu_{1.97}S$ bulks. Furthermore, our $Cu_{1.97}S$ exhibits a much higher Vickers hardness of ~ 1.0 GPa compared to PbTe,[21] Bi_2Te_3,[22] and PbSe[23] polycrystalline bulks. Density functional theory (DFT) calculations of the high temperature *α*-phase $Cu_{2-x}S$ reveal that copper deficient $Cu_{2-x}S$ compounds are intrinsic *p*-type conductors with similar band structure but shifted Fermi level compared to the stoichiometric Cu_2S.

3.2 Experimental

3.2.1 Sample fabrications

Highly dense $Cu_{2-x}S$ polycrystalline bulks were fabricated by a melt-solidification technique. A mixture of Cu and S powders in the molar ratio 2-x : 1 (x = 0, 0.03) was pressed into pellets and sealed in evacuated quartz tubes, before being heated to 673 K for 1-5 hours with a heating rate of 5 K/min, and then heated to ~ 1423 K for 1-2 hours with a heating rate of 5 K/min, followed by a furnace cooling to room temperature.

The obtained bulks were shaped into disks with dimensions of Φ10 mm × 1 mm for the thermal diffusivity measurements. After the measurements, the same sample disks were cut into rectangular bars for measurements of the electrical conductivity and Seebeck coefficient.

3.2.2 Measurements

X-ray diffraction (XRD) patterns and field emission scanning electron microscope (FE-SEM) images were collected on GBC MMA and JEOL JSM-7500FA systems, respectively. The electrical conductivity and Seebeck coefficient were measured simultaneously in a helium atmosphere in the temperature range from 400 to 973 K using an RZ2001i system. The thermal diffusivity (D) was measured by the laser flash method (LINSEIS LFA 1000), and the specific heat (C_p) was determined by differential scanning calorimetry (Mettler Toledo TGA/DSC 1). The sample density (dd) was determined by the Archimedes method. The thermal conductivity (κ) was calculated by $\kappa = D \times C_p \times dd$. Vickers hardness of the as-prepared samples was measured at different locations employing the Duramin 70 Vickers hardness tester applying a load of 0.1 N.

3.2.3 Calculation details

First principles calculations were performed using density functional theory (DFT) implemented by the Cambridge Serial Total Energy Package (CASTEP) package[24] . The generalized gradient approximation (GGA)[25] was used in this calculation, with parameterization by the Perdew-Burke-Ernzerhof (PBE)[26] and ultra-soft pseudo-potentials. The plane wave cut-off energy was set at 400 eV. A 4×4×4 Monkhorst-Pack k-point mesh, with a Brillouin zone path of ΓXWLΓK of the primitive cell, was employed for the band structure calculations. The total and partial density of states of Cu_2S and copper deficient $Cu_{15}S_8$ were calculated on a 2×2×2 super-cell of the primitive cell.

3.3 Results and discussion

3.3.1 Structural properties

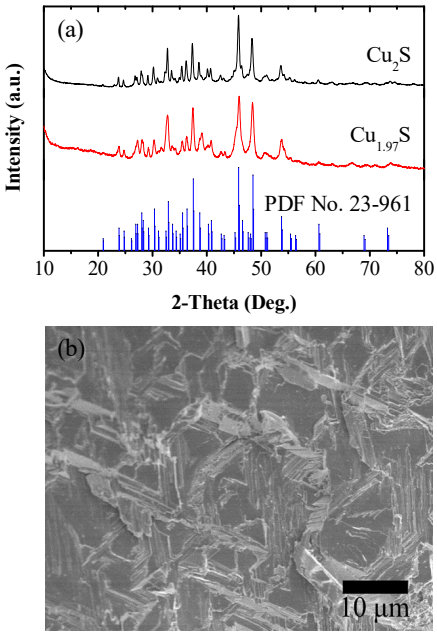

Figure 3-1 (a) X-ray diffraction patterns for the Cu_2S and $Cu_{1.97}S$ bulks fabricated by a melt-solidification technique, and for standard low temperature β-phase Cu_2S (PDF No.

23-961), and (b) Typical field emission scanning electron microscope cross-sectional image of the melted-solidified bulks.

Figure 3-1(a) shows the X-ray diffraction patterns for the Cu_2S and $Cu_{1.97}S$ bulks fabricated by a melt-solidification technique. The results indicate that all the fabricated bulks are single-phase and crystallized in the orthorhombic structure (PDF No. 23-961). Furthermore, Figure 3-1(b) displays the typical field emission scanning electron microscope cross-sectional image of the melted-solidified bulks, implying that the melt-solidified bulks are composed of highly dense and micro-scale grains without any visible voids or porosity.

3.3.2 Thermoelectric properties

3.3.2.1 Electronic transport property

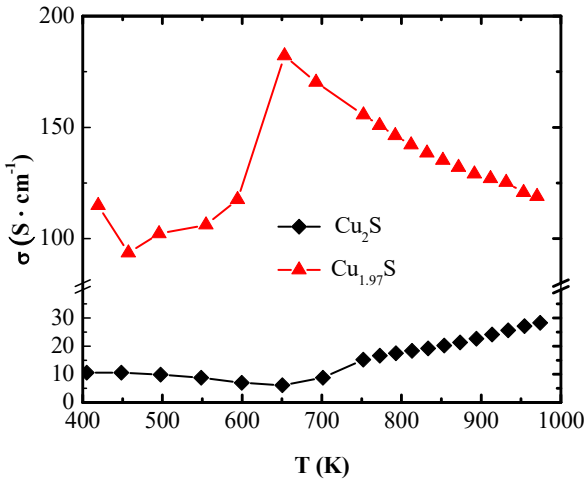

Figure 3-2 Temperature dependence of electrical conductivity (σ) for the fabricated Cu_2S and $Cu_{1.97}S$ polycrystalline bulks.

Figure 3-2 shows the temperature dependence of the electrical conductivity for the Cu_2S and $Cu_{1.97}S$ bulks in the temperature range from 400 K to 1000 K. The electrical conductivity for the high temperature α-phase $Cu_{1.97}S$ bulks decreases as the temperature increases, showing the typical electrical conductivity behaviour of metallic

or heavily doped semiconducting materials, with values between 185 and 120 $S \cdot cm^{-1}$ over a wide temperature range from 700 to 1000 K. On the other hand, the Cu_2S bulks have much smaller electrical conductivity over the whole measured temperature range compared to the $Cu_{1.97}S$ bulks, with the highest value ~ 30 $S \cdot cm^{-1}$ at 973 K.

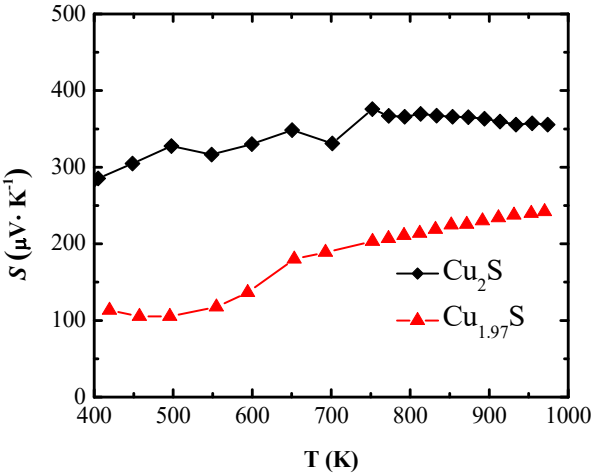

Figure 3-3 Temperature dependence of Seebeck coefficient (*S*) for the fabricated Cu_2S and $Cu_{1.97}S$ polycrystalline bulks.

Figure 3-3 shows the temperature dependence of Seebeck coefficient (*S*) for the fabricated Cu_2S and $Cu_{1.97}S$ polycrystalline bulks. The results indicate that the Cu_2S sample has a much higher Seebeck coefficient than $Cu_{1.97}S$ from 400 to 1000 K, with the highest values being ~ 240 $\mu V \cdot K^{-1}$ for $Cu_{1.97}S$ and ~ 370 $\mu V \cdot K^{-1}$ for Cu_2S, respectively.

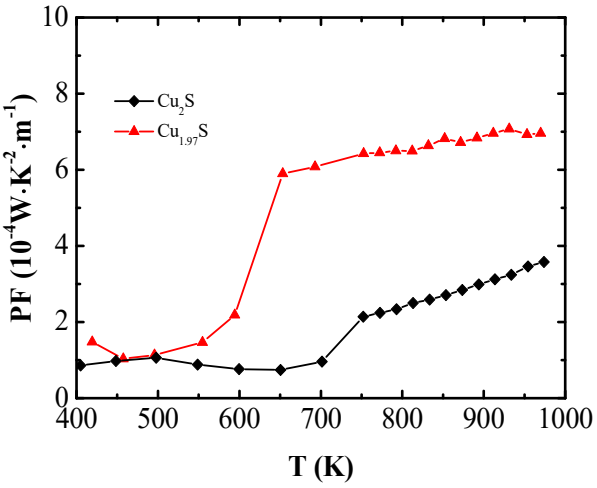

Figure 3-4 Temperature dependence of power factor (PF) for the fabricated Cu_2S and $Cu_{1.97}S$ polycrystalline bulks.

Figure 3-4 displays the temperature dependence of power factor (PF) for the fabricated Cu_2S and $Cu_{1.97}S$ polycrystalline bulks. It reveals that, in the temperature range from 650K to 1000 K, the cubic structured $Cu_{1.97}S$ bulks have greatly enhanced power factor compared to the stoichiometric cubic structured Cu_2S bulks with values around 7.0×10^{-4} W·K^{-2}·m^{-1} for the $Cu_{1.97}S$ bulks which is about two times of the power factor the Cu_2S bulks. This is consistent with the results obtained from the temperature dependence of electrical conductivity and Seebeck coefficient. It is well known that the thermoelectric performance is greatly related to power factor. Therefore, we anticipate that the $Cu_{1.97}S$ bulks should have much better thermoelectric performance in comparison with the Cu_2S bulks, with greatly improved *zT* values.

3.3.2.2 Thermal transport property

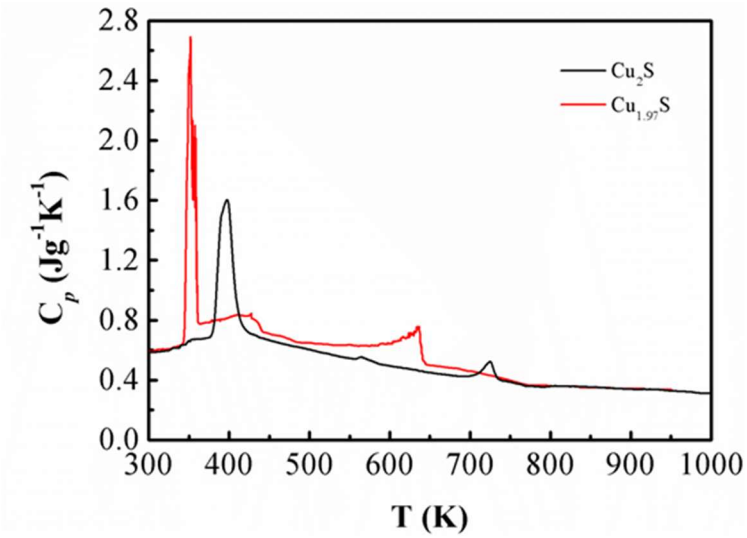

Figure 3-5 Temperature dependence of specific heat (C_p) for the fabricated Cu_2S and $Cu_{1.97}S$ polycrystalline bulks.

Figure 3-5 shows the temperature dependence of specific heat (C_p) for the fabricated Cu_2S and $Cu_{1.97}S$ polycrystalline bulks. The results indicate that both the Cu_2S and $Cu_{1.97}S$ bulks exhibit two phase transitions at around 350 - 400 K and 600 - 750 K, respectively.

In order to further investigate the thermal transport properties of the $Cu_{2-x}S$ system, we have also calculated κ_L and κ_c. According to the Wiedemann-Franz relationship, κ_c can be estimated by $\kappa_c = LT\sigma$, where L is the Lorenz number.[27-30] Here, we take $L = 1.5 \times 10^{-8}\ V^2 \cdot K^{-2}$ to calculate κ_c. Our results show that the $Cu_{1.97}S$ samples have much higher κ_c values in the whole temperature range from 300 to 1000 K, especially when the temperature is higher than 650 K. This can be ascribed to the higher electrical conductivity of the $Cu_{1.97}S$ samples compared to that of the Cu_2S samples. For the lattice thermal conductivity, the Cu_2S and $Cu_{1.97}S$ samples have comparable values in the temperature range from 300 to 650 K, while the $Cu_{1.97}S$ samples exhibit much lower

values than the Cu_2S samples when T is over 650 K. furthermore, both the high temperature cubic structured Cu_2S and $Cu_{1.97}S$ show stable κ_L values owing to their liquid-like crystal structure.

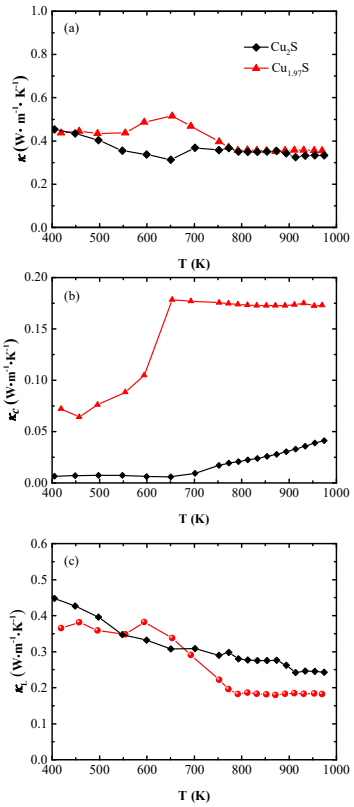

Figure 3-6 Temperature dependence of the thermal transport properties for the fabricated Cu_2S and $Cu_{1.97}S$ polycrystalline bulks: (a) total thermal conductivity (κ), (b) charge carrier thermal conductivity (κ_c), and (c) lattice thermal conductivity (κ_L).

3.3.2.3 Thermal and electronic transport property stability

In order to test whether the $Cu_{2-x}S$ bulk is electrically and thermally stable, which is essential for practical application, or not, we have repeated the measurements from room temperature to 1000 K several times for the same sample. The differential scanning calorimeter thermal response plots for the fabricated $Cu_{1.97}S$ bulks are

displayed in Figure 3-7, indicating that the fabricated $Cu_{1.97}S$ bulks are very thermally stable.

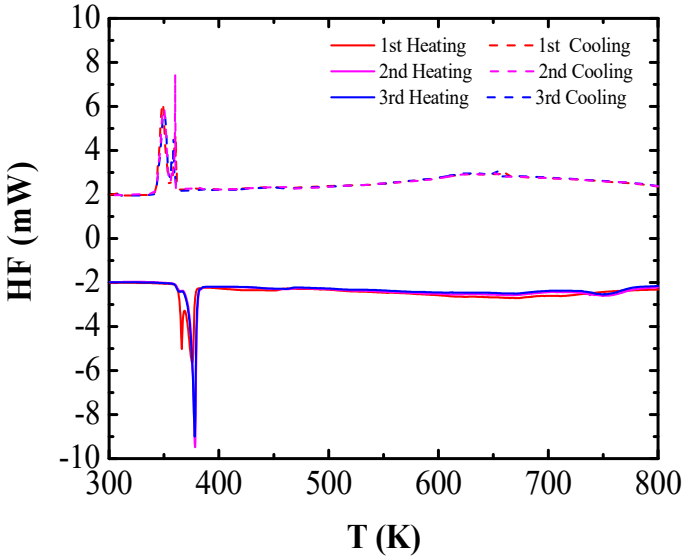

Figure 3-7 Differential scanning calorimeter thermal response plots for the fabricated $Cu_{1.97}S$ bulks.

The temperature dependence of both the electrical conductivity and thermal diffusivity is displayed in Figure 3-8. The results reveal that both Cu_2S and $Cu_{1.97}S$ show quite good repeatibility for the thermal diffusivity during the repeated heating and cooling processes, which are in good agreement with the results derived from the repeated DSC measurements. However, the temperature dependence of elelcrical conductivity indicates that both of the obtained Cu_2S and $Cu_{1.97}S$ show poor electrical stability under the concurrent of high temperature and electrical field. The electrical conductivity decreases with the increasing times of heating and coolinng processes. This poor reproducibility can be ascribed to several factors. It might be related to the superionic conductivity of this compound, the copper ions could move from one side of the sample to the other side upon the application of an electrical field. Additionally, the evaporation of sulphur during the measurements can also lead to poor reproducibility of the electrical conductivity.[31] These problems might can be restained by decreasing the

applied elelctrical field for measurements, doping approaches that can weaken the drift of copper ions, and increasing the pressure of inert gases in the measurement chamber to supress the evaporation.It should be noted that the stable thermal properties, such as heat flow and thermal diffusivity, could make this compound find potentail applications in other thermal related areas.

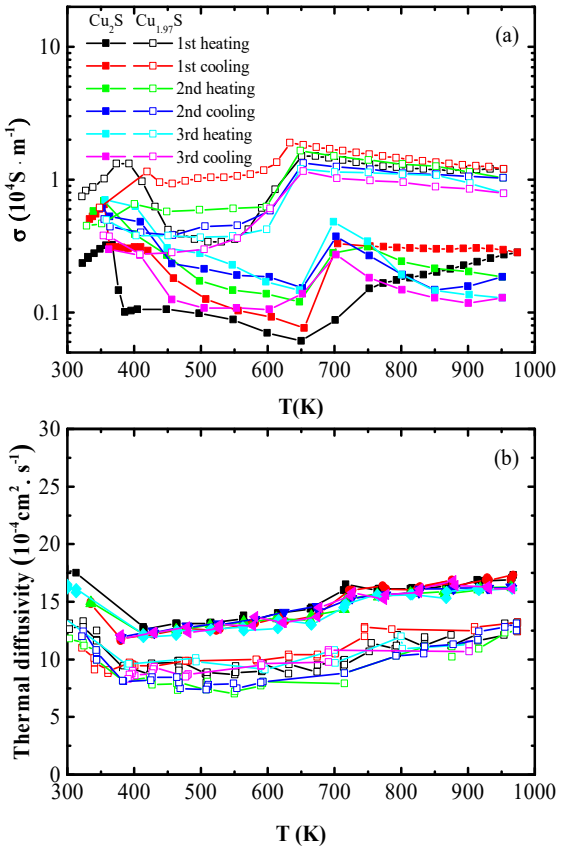

Figure 3-8 Temperature dependence of the electrical conductivity and thermal diffusion for the fabricated Cu_2S and $Cu_{1.97}S$ polycrystalline bulks: (a) electrical conductivity, and (b) thermal diffusion. For each sample, we measured six times with three heating and three cooling processes.

3.3.2.4 Dimensionless Figure-of-merit

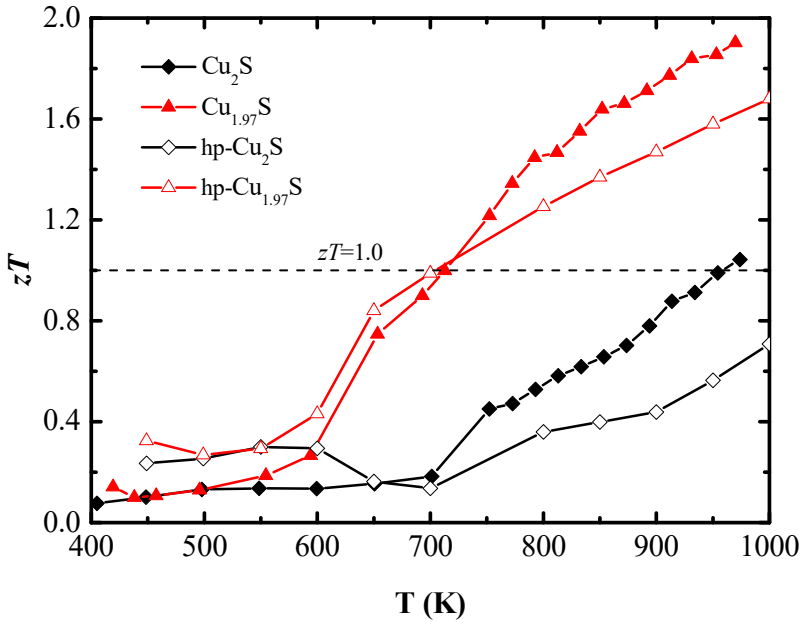

Figure 3-9 Temperature dependence of the dimensionless figure-of-merit (zT) for the fabricated Cu_2S and $Cu_{1.97}S$ polycrystalline bulks.

Figure 3-9 shows the dimensionless figure-of-merit (zT) for the fabricated Cu_2S and $Cu_{1.97}S$ polycrystalline bulks. It demonstrates that the total thermoelectric performance is very sensitive to the copper deficiency, with zT over 1.0 at T > 700 K and as high as 1.9 at 973 K for the $Cu_{1.97}S$, and zT of ~ 1.0 at 973 K for the Cu_2S. Furthermore, in the temperature range from 700 to 1000 K, the Cu_2S and $Cu_{1.97}S$ bulks fabricated by the melt-solidification technique confirm the high thermoelectric performance of $Cu_{2-x}S$ with perhaps even higher zT values compared to the SPS hot-pressed samples,[9] which could be due to better optimization of the carrier concentration via the copper deficiency.

3.3.3 Mechanical property

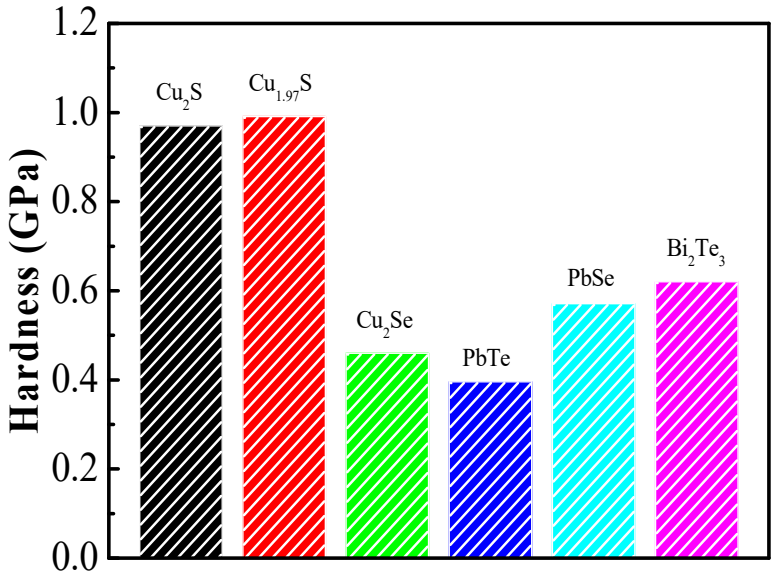

Figure 3-10 Vickers hardness values of the fabricated Cu_2S and $Cu_{1.97}S$ bulks. The hardness values of polycrystalline Bi_2Te_3, PbTe, PbSe, and Cu_2Se bulks are also provided for comparison.

Figure 3-10 shows the Vickers hardness values of the Cu_2S and $Cu_{1.97}S$ polycrystalline bulks. The Vickers hardness values of several other thermoelectric materials are also presented for comparison. It was reported that hot-pressed polycrystalline Bi_2Te_3[32], PbTe[33], and PbSe[23] bulks show hardness of around 0.62, 0.40, and 0.60 GPa, respectively. Compared to the $Cu_{2-x}Se$ polycrystalline bulks having hardness of around 0.42 GPa, the Cu_2S and $Cu_{1.97}S$ bulks exhibit much higher hardness, with values of ~ 0.97 GPa for the Cu_2S and ~ 1.0 GPa for the $Cu_{1.97}S$, respectively.

3.3.4 First principles calculations on electronic band structures and density-of-states

Figure 3-11 shows the ideal version of unit cell (a) and primitive cell (b) for the high temperature α-phase Cu_2S. It indicates that high temperature α-phase Cu_2S is crystallized as a cubic structure with space group of $Fm\bar{3}m$. The S atoms form a rigid face-centred cubic (*fcc*) sub-lattice, while the Cu atoms occupy the tetrahedral interstitial positions in the ideal unit cell.

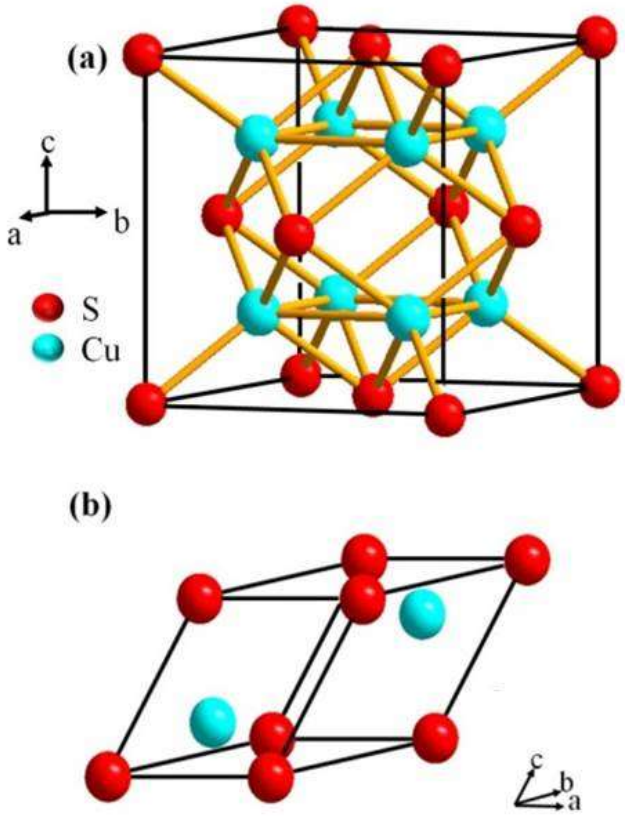

Figure 3-11 Ideal version of unit cell (a) and primitive cell (b) for the high temperature α-phase Cu_2S.

Figure 3-12 shows the calculated electronic band structures for the high temperature cubic phase of the stoichiometric Cu_2S. The calculations predict that Cu_2S will be a small-band-gap semiconductor. The calculated band gap is essentially zero at the Γ point, but it is well known that the DFT method often underestimates the gap.[34, 35]

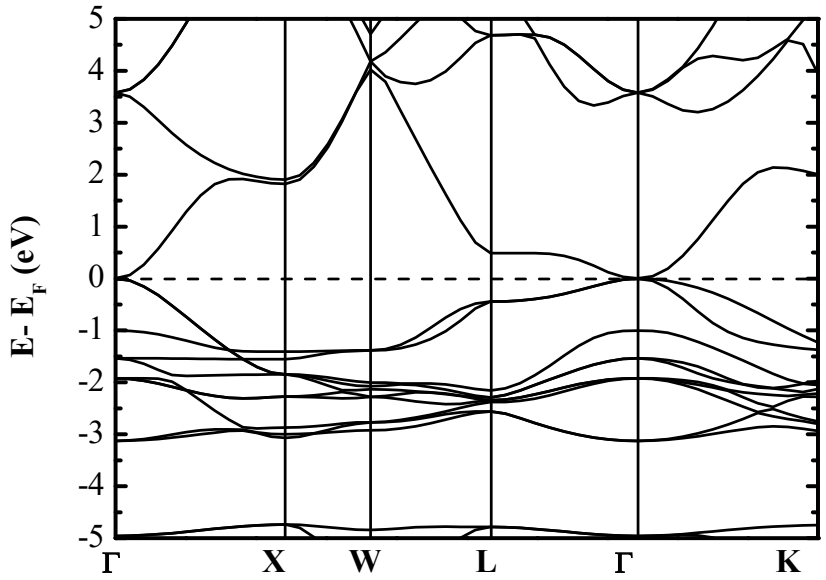

Figure 3-12 Calculated electronic band structures for the stoichiometric Cu_2S.

Figure 3-13 shows the calculated total and partial density of states (DOS) for the stoichiometric Cu_2S and copper deficient $Cu_{15}S_8$. It reveals that the valence bands consist of three regions: a lower region between 12 and 16 eV below the E_F, which is mainly constituted by S 3s states, a middle region between 4 and 8 eV below the E_F, which is a mixture of Cu 3p, 3d, and 4s states, and S 3p states, and an upper region between the E_F and -4 eV, which mostly consists of Cu 3d states, even though the S 3p states also contribute to this region.

For the stoichiometric Cu_2S, the calculated partial and total DOS is in good agreement with the electronic band structure calculation results, further evidence that the stoichiometric Cu_2S is a small-band-gap semiconductor. As to the copper deficient $Cu_{15}S_8$, the Cu 3d states and S 3p states of the middle region, belonging to the valence bands, penetrate into E_F. This explains well why the copper deficient $Cu_{2-x}S$ is a p-type conductor and why its conductivity is higher than that of the stoichiometric Cu_2S from experimental observations.

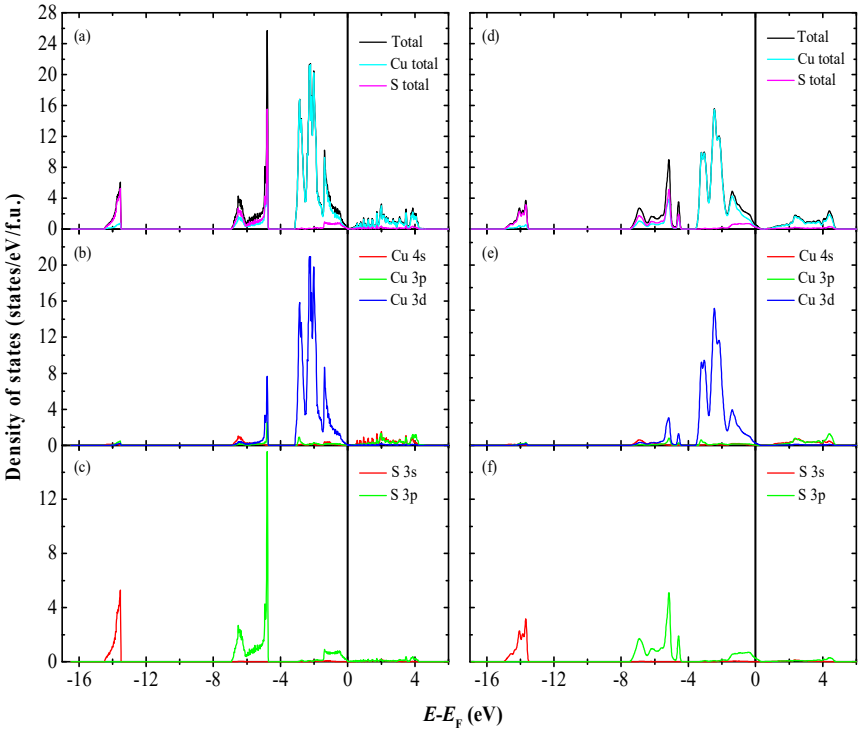

Figure 3-13 Calculated total and partial density-of-states (DOS) for the stoichiometric Cu_2S (left) and copper deficient $Cu_{15}S_8$ (right) using density functional theory.

3.4 Conclusions

In summary, our results indicate that the melt-solidification technique works well for the fabrication of highly dense Cu_2S and $Cu_{1.97}S$ polycrystalline bulks. The fabricated $Cu_{1.97}S$bulks show excellent thermoelectric performance, with zT as high as ~1.9 at 973 K, and good mechanical properties with a Vickers hardness of ~ 1.0 GPa. Density functional theory calculations reveal that stoichiometric Cu_2S is a small-band-gap semiconductor, and copper deficiency makes the copper deficient $Cu_{2-x}S$ to be a *p*-type conductor. The synthesized Cu_2S and $Cu_{1.97}S$ show good quite good repeatibility for the thermal diffusivity during the repeated heating and cooling processes, however, exhibit poor poor electrical stability under the concurrent of high temperature and electrical field.

References

[1] T. Geballe, G. Hull, Seebeck Effect in Germanium, Phys. Rev. 1954, 94, 1134.

[2] T. C. Harman, J. H. Cahn, M. J. Logan, Measurement of Thermal Conductivity by Utilization of the Peltier Effect, J. Appl. Phys. 1959, 30, 1351.

[3] C. J. Vineis, A. Shakouri, A. Majumdar, M. G. Kanatzidis, Nanostructured thermoelectrics: big efficiency gains from small features, Adv. Mater. 2010, 22, 3970.

[4] P. Jood, R. J. Mehta, Y. Zhang, G. Peleckis, X. Wang, R. W. Siegel, T. Borca-Tasciuc, S. X. Dou, G. Ramanath, Al-doped zinc oxide nanocomposites with enhanced thermoelectric properties, Nano Lett. 2011, 11, 4337.

[5] W. Liu, X. Yan, G. Chen, Z. Ren, Recent advances in thermoelectric nanocomposites, Nano Energy 2012, 1, 42.

[6] M. Zebarjadi, K. Esfarjani, M. S. Dresselhaus, Z. F. Ren, G. Chen, Perspectives on thermoelectrics: from fundamentals to device applications, Energy Environ. Sci. 2012, 5, 5147.

[7] W. G. Zeier, Y. Pei, G. Pomrehn, T. Day, N. Heinz, C. P. Heinrich, G. J. Snyder, W. Tremel, Phonon scattering through a local anisotropic structural disorder in the thermoelectric solid solution $Cu_2Zn_{1-x}Fe_xGeSe_4$, J. Am. Chem. Soc. 2013, 135, 726.

[8] Z. H. Ge, B. P. Zhang, Y. X. Chen, Z. X. Yu, Y. Liu, J. F. Li, Synthesis and transport property of $Cu_{1.8}S$ as a promising thermoelectric compound, Chem. Commun. 2011, 47, 12697.

[9] Y. He, T. Day, T. Zhang, H. Liu, X. Shi, L. Chen, G. J. Snyder, High thermoelectric performance in non-toxic earth-abundant copper sulfide, Adv. Mater. 2014, 26, 3974.

[10] H. Yin, M. Christensen, N. Lock, B. B. Iversen, Zn migration during spark plasma sintering of thermoelectric Zn_4Sb_3, Appl. Phys. Lett. 2012, 101, 043901.

[11] Yi Ma, Qing Hao, Bed Poudel, Yucheng Lan, Bo Yu, Dezhi Wang, Gang Chen, Z. Ren, Enhanced Thermoelectric Figure-of-Merit in p-Type Nanostructured Bismuth Antimony Tellurium Alloys Made from Elemental Chunks, Nano Lett. 2008, 8, 2580.

[12] A. C. Kallel, G. Roux, C. L. Martin, Thermoelectric and mechanical properties of a hot pressed nanostructured n-type $Si_{80}Ge_{20}$ alloy, Materials Science and Engineering: A 2013, 564, 65.

[13] K. Ueno, A. Yamamoto, T. Noguchi, T. Inoue, S. Sodeoka, H. Obara, Optimization of hot-press conditions of Zn_4Sb_3 for high thermoelectric performance. II. Mechanical properties, J. Alloys Compd. 2005, 388, 118.

[14] D. J. L. Chakrabarti, D. E., The Cu-S (Copper-Sulfur) system, Bullentin of Alloys Phase Diagrams 1983, 4, 254.

[15] J. William R. Cook, Phase changes in Cu_2S as a function of temperature, Solid State Chem. 1972, 364, 703.

[16] J. Howard T. Evans, Copper coordination in low chalcocite and djurleite and other copper-rich sulfides, American Mineralogist 1981, 66, 807.

[17] E. Hirahara, The Physical Properties of Cuprous Sulfides-Semiconductors, J Phys Soc Jpn 1951, 6, 422.

[18] B. Yu, W. Liu, S. Chen, H. Wang, H. Wang, G. Chen, Z. Ren, Thermoelectric properties of copper selenide with ordered selenium layer and disordered copper layer, Nano Energy 2012, 1, 472.

[19] H. Liu, X. Shi, F. Xu, L. Zhang, W. Zhang, L. Chen, Q. Li, C. Uher, T. Day, G. J. Snyder, Copper ion liquid-like thermoelectrics, Nat. Mater. 2012, 11, 422.

[20] D. R. Brown, T. Day, T. Caillat, G. J. Snyder, Chemical Stability of $(Ag,Cu)_2Se$: a Historical Overview, J. Electron. Mater. 2013, 42, 2014.

[21] Y. Gelbstein, Z. Dashevsky, M. P. Dariel, The search for mechanically stable PbTe based thermoelectric materials, J Appl Phys 2008, 104, 033702.

[22] G. Li, K. R. Gadelrab, T. Souier, P. L. Potapov, G. Chen, M. Chiesa, Mechanical properties of $Bi_xSb_{2-x}Te_3$ nanostructured thermoelectric material, Nanotechnology 2012, 23, 065703.

[23] M. S. Darrow, W. B. White, R. Roy, Microindentation hardness variation as a function of composition for ploycrystalline solutions in the systems PbS/PbTe, PbSe/PbTe, and PbS/PbSe, J. Mater. Sci. 1969, 4, 313.

[24] S. J. Clark, M. D. Segall, C. J. Pickard, P. J. Hasnip, M. I. J. Probert, K. Refson, M. C. Payne, First principles methods using CASTEP, Z. Kristallogr. 2005, 220, 567.

[25] P. Hohenberg, Inhomogeneous electron gas, Phys. Rev. 1964, 136, B864.

[26] J. P. Perdew, K. Burke, M. Ernzerhof, Generalized Gradient Approximation Made Simple, Phys. Rev. Lett. 1996, 77, 3865.

[27] Y. Z. Pei, A. D. Lalonde, N. A. Heinz, X. Shi, S. Iwanaga, H. Wang, L. D. Chen, G. J. Snyder, Stabilizing the optimal carrier concentration for high thermoelectric efficiency, Adv. Mater. 2011, 23, 5674.

[28] J. Androulakis, C. H. Lin, H. J. Kong, C. Uher, C. I. Wu, T. Hogan, B. A. Cook, T. Caillat, K. M. Paraskevopoulos, M. G. Kanatzidis, Spinodal decomposition and nucleation and growth as a means to bulk nanostructured thermoelectrics: enhanced performance in $Pb_{1-x}Sn_xTe$-PbS, J. Am. Chem. Soc. 2007, 129, 9780.

[29] A. Bejan, A. D. Allan, Heat Transfer Handbook, Wiley, New York, 2003.

[30] R. J. Mehta, Y. Zhang, C. Karthik, B. Singh, R. W. Siegel, T. Borca-Tasciuc, G. Ramanath, A new class of doped nanobulk high-figure-of-merit thermoelectrics by scalable bottom-up assembly, Nat. Mater. 2012, 11, 233.

[31] G. Dennler, R. Chmielowski, S. Jacob, F. Capet, P. Roussel, S. Zastrow, K. Nielsch, I. Opahle, G. K. H. Madsen, Are Binary Copper Sulfides/Selenides Really New and Promising Thermoelectric Materials?, Adv. Energy Mater. 2014, 4, 1301581.

[32] L. Zhao, B. Zhang, J. Li, M. Zhou, W. Liu, J. Liu, Thermoelectric and mechanical properties of nano-SiC-dispersed Bi_2Te_3 fabricated by mechanical alloying and spark plasma sintering, J. Alloys Compd. 2008, 455, 259.

[33] Y. Gelbstein, G. Gotesman, Y. Lishzinker, Z. Dashevsky, M. P. Dariel, Mechanical properties of PbTe-based thermoelectric semiconductors, Scripta Mater 2008, 58, 251.

[34] P. Gorai, P. Parilla, E. S. Toberer, V. Stevanović, Computational Exploration of the Binary A1B1 Chemical Space for Thermoelectric Performance, Chem Mater 2015, 27, 6213.

[35] K. Niedziolka, R. Pothin, F. Rouessac, R. M. Ayral, P. Jund, Theoretical and experimental search for ZnSb based thermoelectric materials, J. Phys. Condens. Mat. 2014, 26, 365401.

CHAPTER 4

4 STRUCTURAL AND THERMOELECTRIC PROPERTIES FOR THE CRYSTAL AND MELT-QUENCHED $CU_{2-X}SE$

4.1 Preface

High temperature thermoelectric technology has been increasingly significant for a sustainable and environmental friendly supply of clean energy, due to our increasingly severe environmental problems and the energy crisis.[1-3] Thermal energy can be converted into electricity directly when a temperature gradient is formed on thermoelectric junctions.[4-7] Thermoelectric devices can work with high reliability, quiet operation due to the lack of moving parts, and no pollution.[8-10]

Many alloys and nanostructured materials, such as Co_4Sb_{12}, β-Zn_4Sb_3, and PbTe or PbSe-based alloys, have been investigated extensively and developed as high temperature thermoelectric materials for power generation.[11-17] Furthermore, their thermoelectric performance has been improved greatly, with the thermoelectric zT over 1.0. It is well known that the energy conversion efficiency of thermoelectric materials at a temperature T can be evaluated by the dimensionless thermoelectric figure-of-merit, zT, which is related to such parameters as the Seebeck coefficient, absolute temperature, electrical resistivity, and total thermal conductivity.[18-23] Furthermore, κ can be expressed by $\kappa = \kappa_L + \kappa_c$, where κ_L and κ_c are the lattice thermal conductivity, and the

charge carrier thermal conductivity, respectively. Lattice or atomic vibrations contribute predominantly to κ at high temperatures compared to those of the charge carriers.

Among these parameters, κ is the decisive factor ruling the thermoelectric performance, as it determines the heat transport capability between the hot and cold sides of the thermoelectric modules. Therefore, reducing κ has been the main focus of studies aiming to improve zT for various types of high temperature thermoelectric materials in particular. The following effective approaches have been commonly used so far to reduce κ through phonon refinements: 1) Reducing particle sizes to the nanoscale using nano-engineering, which gives rise to both intra-grain and inter-grain (grain boundaries) phonon confinement; 2) Fabricating multilayer thin films to reduce the dimensionality of thermoelectric materials; and 3) Doping with heavy atoms to effectively reduce the phonon vibrations.

Nevertheless, the fabrication methods employed for multilayer thin films and nanoparticles involve costly instruments that are capable of operating under conditions of high vacuum, high temperature, and high pressure, as well as complicated chemical processes. Highly dense polycrystalline thermoelectric bulks are commonly synthesized by the hot pressing method under high temperature and high pressure, using expensive spark plasma sintering (SPS) systems. They are all very costly and long heat treatments are needed (usually up to several days), making thermoelectric materials less suitable

for practical applications. Therefore, it is much desirable to find an effective fabrication method that is low-cost and time-saving.

We propose to achieve highly dense samples with excellent thermoelectric performance for certain type of thermoelectric compound by employing a low-cost and time-saving method based on the following facts and analyses: 1) Materials possessing the congruent melting property should maintain the same chemical phase and composition from the homogeneous melt state to the solid state, despite subtle difference in real chemical composition of the solid and melt state due to possible loss of volatile element(s) above the melting temperature. This means that highly dense bulks should be easily obtained by melt-quenching approach. This has been successfully adopted in single crystal growth and casting technology for various materials, giving highly density and excellent performance, although little work has been done on the fabrication of polycrystalline thermoelectric materials.[24-27] 2) Anisotropy plays a significant role in the thermoelectric performance of a material with anisotropic crystal structure or low crystal symmetry.[28] It should be noted that the anisotropy is an important or an additional factor that is likely to affect the overall thermoelectric performance of polycrystalline bulk samples, and it needs to be taken into account in the consideration of zT improvement.

Materials showing excellent thermoelectric performance, such as Bi_2Te_3, exhibit high anisotropy in their crystal structures, which is likely to be the reason why the

polycrystalline-bulk samples have lower zT than the single-crystal samples with certain preferred crystallographic directions. Inspired by the above considerations, for cubic structured thermoelectric materials, their thermoelectric performances along three main crystallographic axes (*a*, *b*, and *c* directions) should be the same due to the identical arrangement of atoms along these equivalent directions. Grain boundaries or particle sizes should have less effect on κ and other thermoelectric parameters in cubic structured thermoelectric materials compared to those with low crystal symmetry. Therefore, we propose two additional properties for excellent thermoelectric materials: congruent melting and high crystal symmetry, or at least less anisotropy.

It has come to our attention that the recently discovered new class of copper ion liquid-like thermoelectric material, $Cu_{2-x}Se$, ought to meet these requirements. $Cu_{2-x}Se$ bulks prepared by the hot pressing method show high thermoelectric performance with $zT > 1.5$ at T of ~ 1000 K.[29, 30] Its high temperature β-phase has cubic crystal structure with space group of $Fm\bar{3}m$, and copper ions can behave like a liquid, which could lead to similar thermoelectric performance between single crystals and polycrystalline bulks at high temperatures.

Figure 4-1 shows the binary phase diagram of the Cu-Se system [31-33] and assumed ideal unit cell of the high temperature β-phase $Cu_{2-x}Se$.[34] According to this binary phase diagram, the low temperature α-phase $Cu_{2-x}Se$ (shown in Figure 4-2) is transformed to the high-temperature β-phase at ~ 400 K and seems to undergo a

congruent melting at ~ 1400 K. Therefore, we can expect that highly dense $Cu_{2-x}Se$ bulks could be obtained by a melting and quenching (or melt-quenching) method. As this compound can be cupper deficient, we have the following discussions relating to the melting process for this compound.

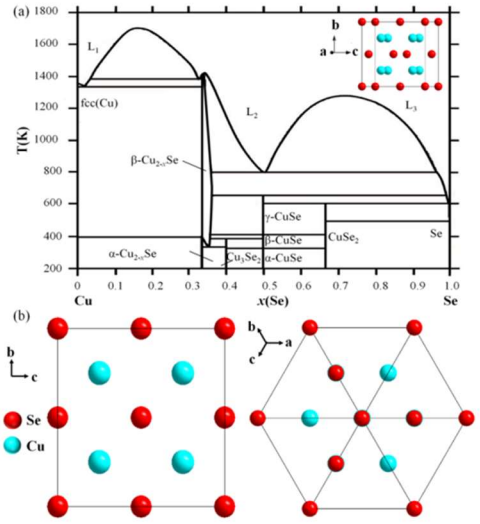

Figure 4-1 (a) Binary phase diagram for the Cu-Se system. The inset shows the 3D unit cell of high temperature β-phase $Cu_{2-x}Se$. (b) Unit cell of high temperature β-phase $Cu_{2-x}Se$ viewed towards the (100) and (111) planes, respectively.

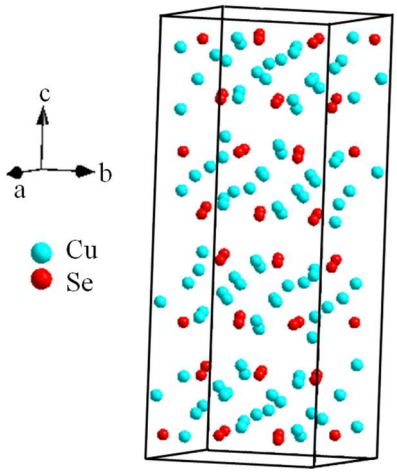

Figure 4-2 Unit cell of low temperature monoclinic structure α-phase Cu_2Se.[1]

Congruent melting occurs during melting of a compound when the composition of the liquid that forms is the same as the composition of the solid. Materials possessing the congruent melting property should maintain the same chemical phase and composition from the homogeneous melt state to the solid state, which means that highly dense bulks should be easily obtained by a melt-quenching approach.

Obviously, congruent melting is suitable for a line compound as the reviewer mentioned. But, it is not appropriate for the compounds with element deficiency, such as $Cu_{2-x}Se$[32-34](x<0.25) and $La_{3-x}Te_4$[24](x<1/3). The exact congruent melting composition for $Cu_{2-x}Se$, has been reported to be $Cu_{1.9975}Se$,[35] or $Cu_{1.9956}Se$,[36] or $Cu_{1.994}Se$.[37] For the $Cu_{2-x}Se$ with other x values, they should not be congruent melting, and the chemical compositions of melt-quenched samples should be different from the nominal composition of starting materials. This is due to the segregation of secondary phase, such as copper precipitation. However, it should be pointed out the amount of the segregated phase is very tiny and often hardly seen from the XRD patterns for melt-quenched $Cu_{2-x}Se$ samples.[29, 38]

Technically speaking, the Cu_2Se and $Cu_{1.98}Se$ used for our study are not congruent melting compounds. Despite of this, the tiny amount of secondary phase is not seen in our XRD patterns for our own samples. Therefore, highly dense bulks should be easily obtained by a melt-quenching approach with tiny changes in compositions compared to the starting materials.

As mentioned above, the thermoelectric performance of cubic structured materials along three main crystallographic axises should be the same due to the identical arrangement of atoms along these equivalent directions. Specifically, for the high temperature β-phase $Cu_{2-x}Se$, it has a cubic structure with space group of $Fm\bar{3}m$ and a quite small bandgap.[29, 39] Furthermore, the copper ions can behave like a liquid in the *fcc* rigid lattice constituted by Se atoms. Therefore, grain boundaries or particle sizes should have less effect on this system's thermal conductivity and other thermoelectric parameters compared to those with low crystal symmetry. Additionally, the liquid-like behavior of copper ions is favorable for both low electrical resistivity and low thermal conductivity. Therefore, the excellent thermoelectric performance should be intrinsic and less anisotropic for the high temperature β-phase $Cu_{2-x}Se$, because it is dominated by the liquid-like copper ions.

We anticipate that as long as the $Cu_{2-x}Se$ samples have 100% density, they should show high thermoelectric performance, regardless of grain sizes. Based on our analysis on the binary phase diagram of Cu-Se system, the long sintering reported for highly dense $Cu_{2-x}Se$ bulks seems to be unnecessary. The melt-quenching approach should only take a few minutes to achieve highly dense $Cu_{2-x}Se$ bulks, in contrast to the conventional hot-pressing method, which requires hours of heat treatment under high pressure and high temperature. Furthermore, there is a lack of information on what the intrinsic thermoelectric performance or zT should be for the $Cu_{2-x}Se$. Therefore, it is

important to carry out experiments using $Cu_{2-x}Se$ single crystals for the investigation of its intrinsic thermoelectric properties, as well as for comparison purposes.

4.2 Experimental

4.2.1 Sample fabrications

Firstly, polycrystalline $Cu_{2-x}Se$ pellets were synthesized by a conventional solid-state method. A mixture of Cu and Se powders in the molar ratio 2-x:1 (x = 0.02) was pressed into pellets and sealed in evacuated quartz tubes, before being heated to 873 K for 1-5 hours with a heating rate of 5 K/min, followed by a furnace cooling to room temperature. Secondly, the as-sintered $Cu_{2-x}Se$ pellets were used in the melt-quenching approach. In order to achieve fast melting and quenching, the as-sintered samples were placed at one end of the sealed quartz and heated up using a flame of acetylene and oxygen until they melted completely. They were then quickly quenched in water or liquid nitrogen to obtain highly dense bulks with different grain sizes. For comparison, single crystals were also prepared using a modified Bridgman method. The as-prepared pellets were sealed in a quartz tube and melted at a temperature above 1423 K for 2 hours to obtain a homogeneous melt, followed by cooling down to 1073-1173 K at a rate of 1-5 K/h. The samples were then cooled to room temperature at a rate of 4 K/min.

Finally, the obtained samples were shaped into disks with dimensions of Φ10 mm × 1 mm for thermal diffusivity measurements. After the measurements, the same pieces

of samples were cut into rectangular bars for measurements of the electrical resistivity and Seebeck coefficient.

4.2.2 Measurements

XRD patterns were collected on a GBC MMA system and the Rietveld refinements were done using a soft ware named Retica. FE-SEM images and X-ray Energy dispersive spectroscopy (EDS) for points and mapping were collected from the JEOL JSM-7500FA system. The electrical resistivity and Seebeck coefficient were measured simultaneously in a helium atmosphere in the temperature range from 300 to 973 K using an RZ2001i system. The thermal diffusivity (D) was measured by the laser flash method (LINSEIS LFA 1000), and the specific heat (C_p) was determined by differential scanning calorimetry (TA Q100). The sample density (*dd*) was determined by the Archimedes method. The thermal conductivity (κ) was calculated by $\kappa = D \times C_p \times dd$.

4.3 Results and discussion

4.3.1 Structural properties

Figure 4-3 presents the standard X-ray diffraction (XRD) peaks of low temperature α-phase $Cu_{2-x}Se$ (PDF No. 27-1131), and the XRD patterns of powdered $Cu_{2-x}Se$ bulks fabricated by the melt-quenching approach (quenched in water and liquid nitrogen (LN)), and of a single-crystal sample prepared by a modified Bridgman method. It indicates that the single-crystal sample only shows (00*l*) peaks of low temperature α-

phase $Cu_{2-x}Se$, indicating that the single crystal sample's orientation is [00*l*] at low temperatures. At high temperature, the low temperature α-phase is converted to β-phase. Simultaneously, the (00*l*) plane becomes the (111) plane which has been reported for the $Cu_2Se_{1-x}I_x$ bulk samples.[40] Therefore, in this work, the thermoelectric performance of our single-crystal $Cu_{2-x}Se$ sample was characterized along the (111) plane of high temperature β-phase.

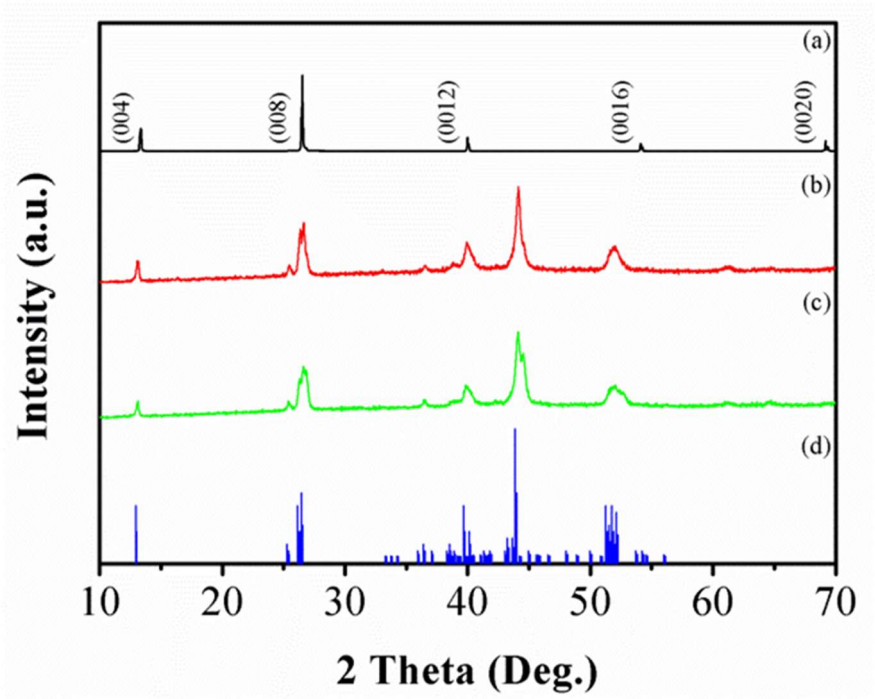

Figure 4-3 X-ray diffraction patterns for as-prepared samples: (a) $Cu_{2-x}Se$ single crystals grown by a modified Bridgman method. (b) Water-quenched $Cu_{2-x}Se$ bulks. (c) LN-quenched $Cu_{2-x}Se$ bulks. (d) Standard XRD peaks of low temperature α-phase $Cu_{2-x}Se$ (PDF No. 27-1131).

We also carried out Rietveld refinements for the powdered single-crystal and polycrystalline bulk samples. The refined XRD patterns and values of Rietveld

refinement parameters (lattice parameters, R-factors, and goodness of fit (GOF)) are displayed in Figure 4-4 and Table 4-1, respectively. The results indicate that all samples have monoclinic structure (space group *C*2/*c*) with some differences in the lattice parameters. No visible traces of any secondary phase were detected under the XRD resolution, which is consistent with previous reports.[38-42]

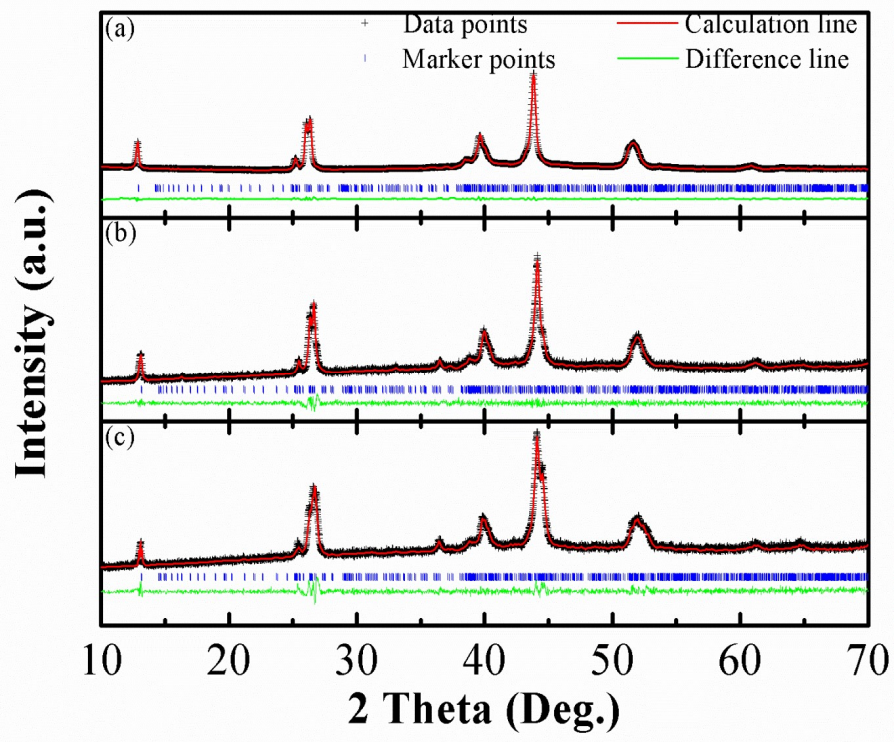

Figure 4-4 Experimental and calculated X-ray diffraction patterns, and the corresponding difference diagram for powdered single-crystal, water-quenched and LN-quenched $Cu_{2-x}Se$ samples.

Table 4-1 Values of Rietveld refinement parameters: lattice parameters, R-factors, and goodness of fit (GOF) deduced from the XRD patterns of the single-crystal, water-quenched, and LN-quenched $Cu_{2-x}Se$ samples.

compound	Single-crystal sample	Water-quenched sample	LN-quenched sample
a(Å)	7.138(1)	7.126(9)	7.138(2)
b(Å)	12.371(1)	12.326(2)	12.276(3)
c(Å)	27.345(1)	27.244(7)	27.228(5)
β	94.365(7)	94.452(5)	94.347(3)
Volume($Å^3$)	2407.7(3)	2386.1(6)	2379.1(9)
R_p	0.990	4.789	5.031
R_{wp}	1.321	6.264	6.520
GOF	3.155	0.509	0.561

4.3.2 Morphologies

Field emission scanning electron microscope (FE-SEM) images of the single-crystal, water-quenched, and LN-quenched polycrystalline $Cu_{2-x}Se$ bulks are shown in Figure 4-5. The single-crystal surface is extremely smooth, and its edge clearly shows the layered structure. All the melt-quenched samples are highly dense without any visible voids or porosity. The average grain size is ~ 10 μm for the water-quenched sample shown in Figure 4-5(c), which is slightly larger than that of the $Cu_{2-x}Se$ bulks prepared by the conventional hot-pressing method.[31,42] The LN-quenched samples also have micro-scaled grains even they are smaller than those in the water-quenched one. Only in the part near the surface, there are some nanoscale grains. This suggests that

$Cu_{2-x}Se$ can be crystallized quickly and it is very hard to achieve small gains for thick or big size samples.

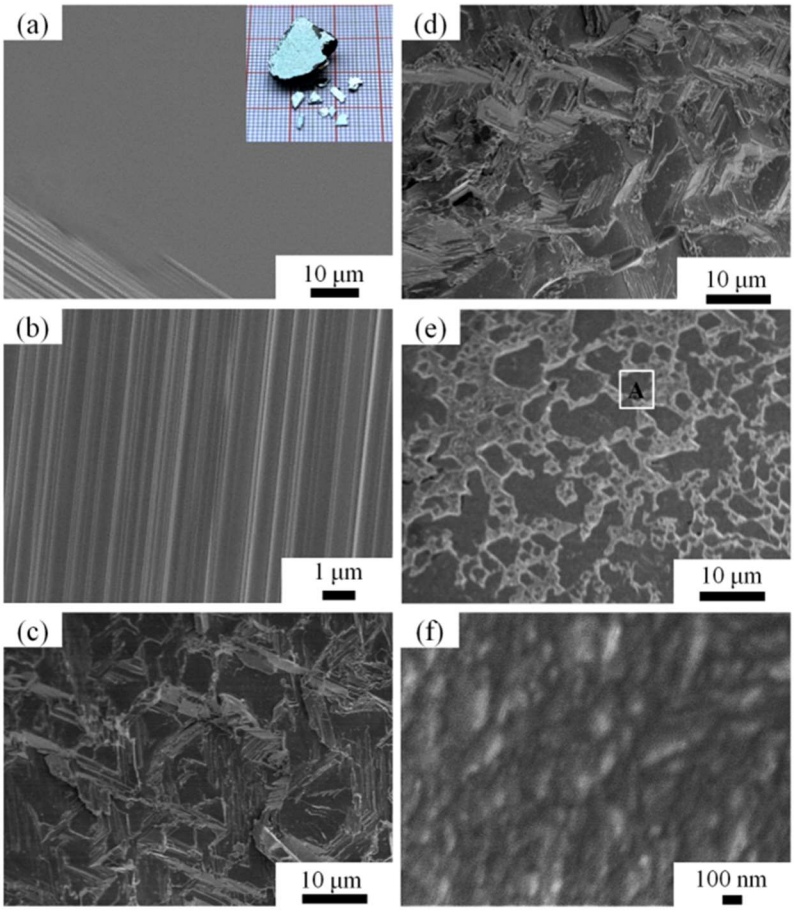

Figure 4-5 FE-SEM images of the as-prepared samples: (a, b) surface and cross-sectional images of single crystals. The inset shows an optical image of the $Cu_{2-x}Se$ single crystals. Cross-sectional images for water-quenched (c), inside (d) and near surface (e) of LN-quenched $Cu_{2-x}Se$ bulks as well as the magnified images of the region A in e (f).

In order to gain insight into real chemical compositions of our samples, we carried out the chemical analysis using the X-ray Energy Dispersive Spectrometer (EDS), and

the results of points and mapping EDS are displayed in Figure 4-6 and Figure 4-7, respectively. According to the point EDS analysis, subtle variations in the real chemical compositions are detected for different samples. The chemical composition is estimated to be $Cu_{2.01}Se$ for single crystals, $Cu_{1.96}Se$ for water-quenched sample, and $Cu_{1.94}Se$ for LN-quenched one, respectively, which is in good agreement with our XRD refinement results. The EDS mapping for all samples indicate that both Cu and Se are distributed homogeneously inside all samples. No Cu or Se rich regions are observed, which means that there is no Se or Cu segregation.

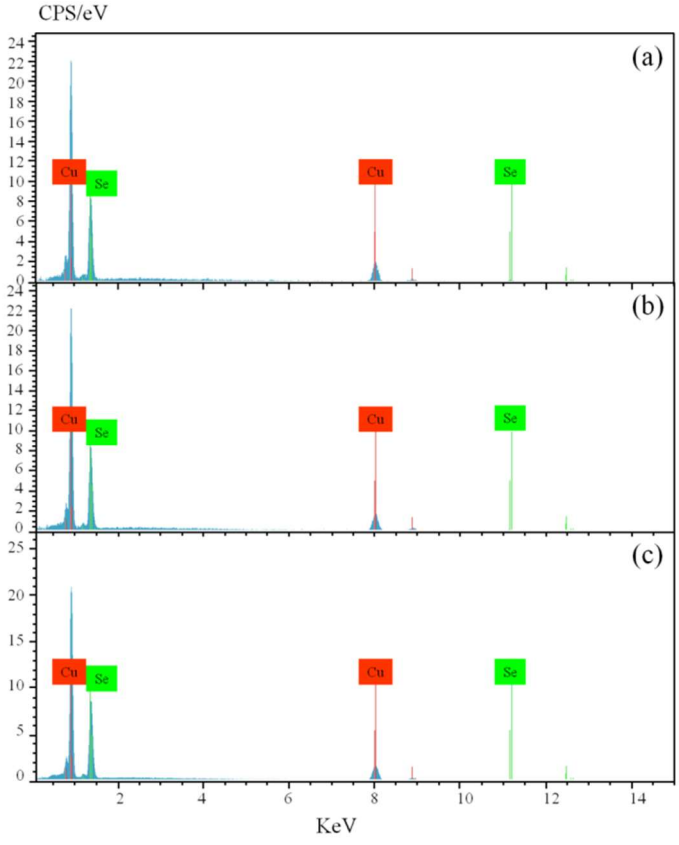

Figure 4-6 X-ray Energy Dispersive Spectroscopy (EDS) of points for the fabricated water-quenched, LN-quenched and single-crystal $Cu_{2-x}Se$ samples.

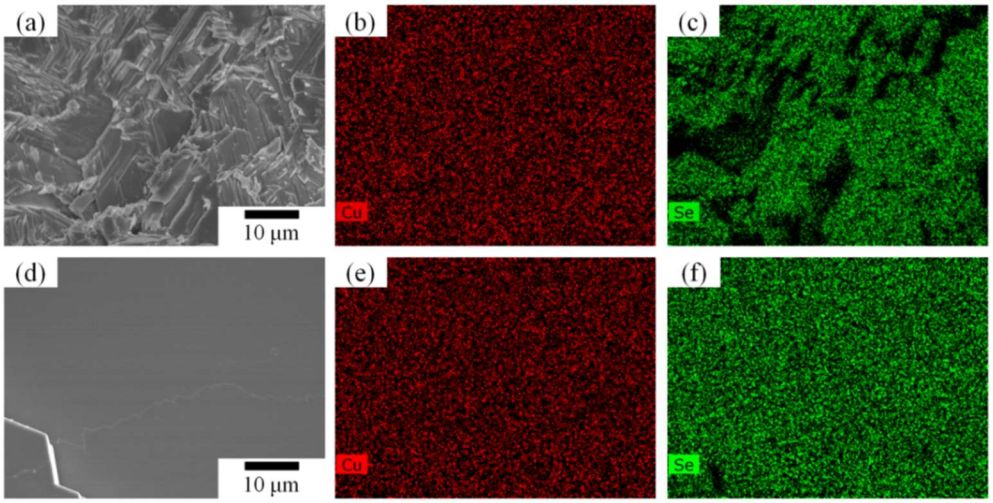

Figure 4-7 X-ray Energy Dispersive Spectrometer (EDS) mapping for the water-quenched (a, b, and c) and single-crystal (d, e, and f) $Cu_{2-x}Se$ samples.

4.3.3 Thermoelectric properties

The temperature dependence of the electrical resistivity (ρ), Seebeck coefficient (S), total thermal conductivity (κ), power factor (PF), lattice thermal conductivity (κ_L), and thermoelectric figure-of-merit (zT) for the single-crystal, water-quenched, and LN-quenched $Cu_{2-x}Se$ samples is plotted in Figure 4-8. The following facts are observed: 1) The values of ρ and zT for all samples show the same trend of increasing with increasing temperature. 2) S shows almost the same value for all samples over the whole temperature range from 300 to 973 K and increases as temperature increases. 3) κ decreases as temperature increases for all samples. 4) The power factor, defined as PF = S^2/ρ, is 4-7 × 10^{-4} $W \cdot m^{-1} \cdot K^{-2}$ for the low temperature α-phase and 4-11.5 × 10^{-4} $W \cdot m^{-1} \cdot K^{-2}$ for the high temperature β-phase, which is comparable to the previously reported

values for the conventional hot-pressed $Cu_{2-x}Se$ samples.[29]) Our LN-quenched $Cu_{2-x}Se$ sample has a $zT \approx 1.5$ at T ~ 973 K, which is as good as what has been reported for the hot-pressed sample.[29, 30] Furthermore, the zT for the water-quenched and single-crystal sample exhibit still higher value around 1.7-1.8 at ~ 973 K.

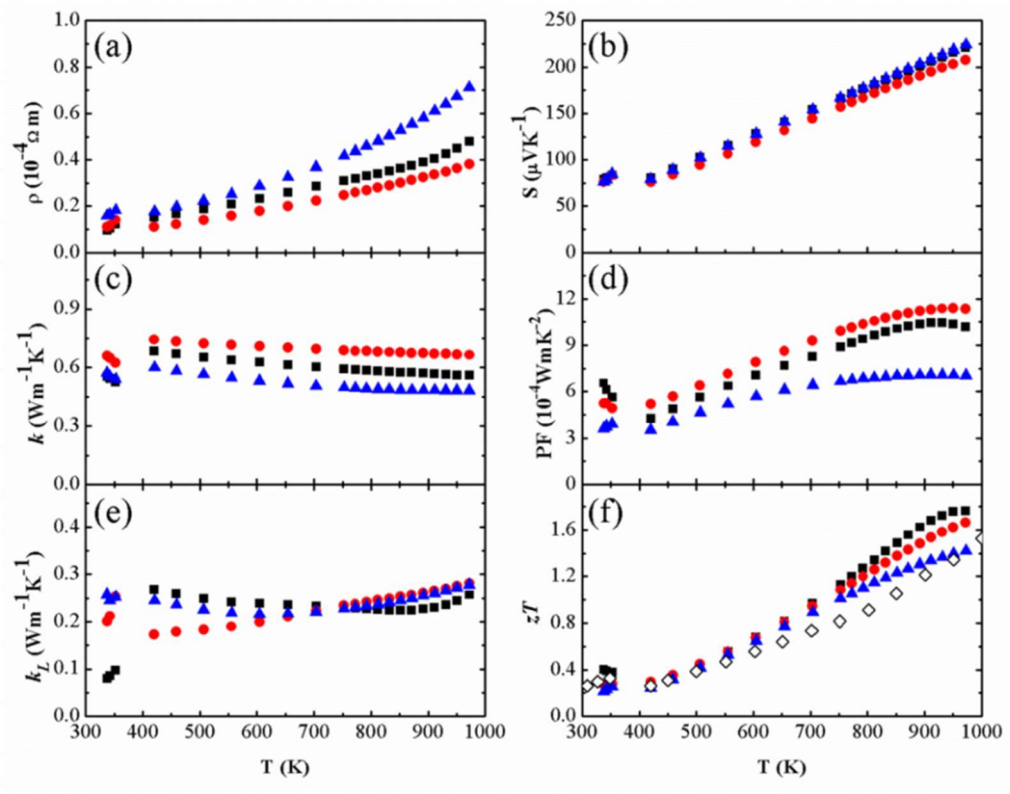

Figure 4-8 Temperature dependence of thermoelectric transport properties of single-crystal and ultrfast-formed $Cu_{2-x}Se$ bulks: (a) electrical resistivity (ρ), (b) Seebeck coefficient (S), (c) total thermal conductivity (κ), (d) lattice thermal conductivity (κ_L), (e) power factor (PF), and (f) thermoelectric figure-of-merit (zT). (■ Single crystals, ● Water-quenched bulks, ▲ LN-quenched bulks, and ◇Polycrystalline bulks synthesized by the hot-pressing method.)

It is interesting to note that compared to the water-quenched $Cu_{2-x}Se$, the LN-quenched one with smaller grain sizes has larger ρ values (~7×10-4 Ω·m) and lower κ values (~ 0.48 $W \cdot m^{-1} \cdot K^{-1}$) at ~ 973 K. This seems to be related to the higher density of grain boundaries which could scatter charge carriers. However, Seekbeck coefficient is almost the same for all samples. Furthermore, single crystal sample shows an intermediate ρ and κ among all samples. All these data indicates that grain sizes may not play an important role in the thermoelectric performance of the $Cu_{2-x}Se$ system at high temperatures. This is largely due to the liquid-like behaviour of copper ions, which dominates the system's thermoelectric performance at high temperatures. Furthermore, the difference in electrical resistivity and thermal conductivity may also be related to the difference in chemical composition of all samples.

According to the Wiedemann-Franz relationship, the charge carrier thermal conductivity (κ_c) can be estimated by $\kappa_c = LT/\rho$, where L is the Lorenz number.[42-44] In this work, we take $L = 1.5 \times 10^{-8}$ $V^2 \cdot K^{-2}$ to calculate κ_c, then subtract it from κ *to* get κ_L. The temperature dependence of the lattice thermal conductivity for all samples is displayed in Figure 4-8(e). It is interesting to note that the LN-quenched sample does not show the lowest lattice conductivity although it has higher density of grain boundaries compared to the others. For conventional thermoelectric materials, high density of grain boundaries can reduce the lattice thermal conductivity effectively. However, it seems that this is not applicable to the $Cu_{2-x}Se$ system because its high

temperature *β*-phase is crystallized in a cubic structure with a rigid *fcc* lattice constituted by Se atoms and kinetically disordered copper ions. It is the liquid-like behaviour of copper ions that dominates the system's high temperature thermoelectric performance. The lattice thermal conductivity of both the LN-quenched and single-crystal $Cu_{2-x}Se$ samples first decreases then increases gently. Interestingly, we note that this phenomenon is also reported by Yu et al.[31] This could be attributed to the liquid-like behaviour of copper ions which can confine the lattice vibrations and in turn reduce the lattice thermal conductivity. When the temperature is over the critical temperature (around 773K), the lattice vibration is mainly confined by the liquid-like copper ions. Therefore, the lattice thermal conductivity should be almost the same for all samples. As for the temperatures below the 773 K, the crystal lattice from both Se and Cu contributes to the lattice thermal conductivity. Additionally, the subtle difference in chemical compositions can also lead to different lattice thermal conductivity.

It should be pointed out that the electrical and thermal stability during the repeated heating and cooling process is quite essential for the practical applications of thermoelectric materials. Therefore, we measured several pieces of samples fabricated by the same method and also repeated several times for each sample to investigate their electrical and thermal stability. The repeatability of the thermal diffusivity, electrical resistivity, and Seebeck coefficient for water-quenched $Cu_{2-x}Se$ bulks are shown in Figure 4-9. The results indicate that our data is reproducible and the samples show quite

good repeatability for the thermal diffusivity, electrical resistivity, and Seebeck coefficient during the repeated measurements.

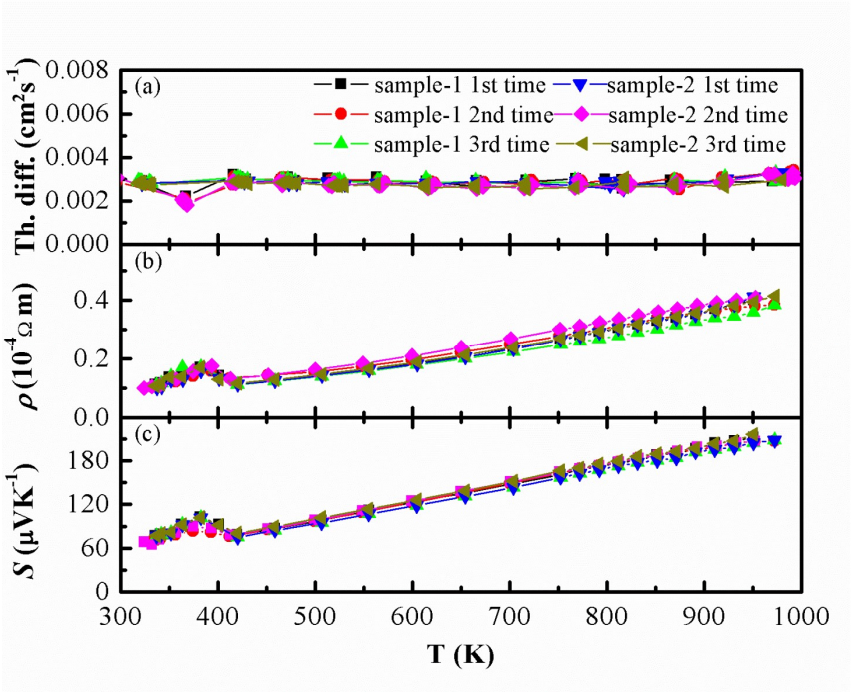

Figure 4-9 Temperature dependence of thermal diffusivity, electrical resistivity and Seebeck coefficient of water-quenched $Cu_{2-x}Se$ samples. The measurements were repeated three times for each sample.

4.4 Conclusion

Our results indicate that the fast melt-quenching method works well for the fabrication of highly dense $Cu_{2-x}Se$ bulks with excellent thermoelectric performance, $zT \approx 1.7$ at 973 K, and this method should be applicable to other types of congruent-melting thermoelectric materials. It is remarkable that the fabrication cost can be reduced significantly, as it only takes a few minutes. We have also proposed that it is

the cubic crystal symmetry and liquid-like behaviour of copper ions that makes $Cu_{2-x}Se$ show superior thermoelectric performance. Our findings pave the way for commercialization of $Cu_{2-x}Se$ as an excellent component in thermoelectric modules and also provide guidance in searching for new classes of isotropic thermoelectric systems or further improving the cost performance of other congruent melting thermoelectric materials. These investigations are currently underway in our group.

References

[1] F. J. DiSalvo, Thermoelectric cooling and power generation, Science 1999, 285, 703.

[2] L. E. Bell, Cooling, heating, generating power, and recovering waste heat with thermoelectric systems, Science 2008, 321, 1457.

[3] A. I. Hochbaum, R. Chen, R. D. Delgado, W. Liang, E. C. Garnett, M. Najarian, A. Majumdar, P. Yang, Enhanced thermoelectric performance of rough silicon nanowires, Nature 2008, 451, 163.

[4] J. Yang, Y. Hin-Lap, A. K. Y. Jen, Rational design of advanced thermoelectric materials, Adv. Energy Mater. 2013, 3, 549.

[5] G. J. Snyder, Toberer, E. S. , Complex thermoelectric materials, Nat. Mater. 2008, 7, 10.

[6] B. C. Sales, Smaller is cooler, Science 2002, 295, 1248.

[7] D. M. Rowe, CRC Handbook of thermoelectric, CRC Handbook of thermoelectrics, CRC press, FL 1995.

[8] D. M. Rowe, CRC hand book of thermoelectrics: macro to nano, CRC hand book of thermoelectrics: macro to nano. CRC Press, New York 2005.

[9] G. S. Nolas, J. Poon, M. Kanatzidis, Recent developments in bulk thermoelectric materials, MRS Bull. 2006, 31, 199.

[10] Y. Z. Pei, A. D. Lalonde, N. A. Heinz, X. Shi, S. Iwanaga, H. Wang, L. D. Chen, G. J. Snyder, Stabilizing the optimal carrier concentration for high thermoelectric efficiency, Adv. Mater. 2011, 23, 5674.

[11] X. Shi, J. Yang, J. R. Salvador, M. Chi, J. Y. Cho, H. Wang, S. Bai, J. Yang, W. Zhang, L. Chen, Multiple-filled skutterudites: high thermoelectric figure of merit through separately optimizing electrical and thermal transports, J. Am. Chem. Soc. 2011, 133, 7837.

[12] E. S. Toberer, P. Rauwel, S. Gariel, J. Taftø, G. Jeffrey Snyder, Composition and the thermoelectric performance of β-Zn_4Sb_3, J. Mater. Chem. 2010, 20, 9877.

[13] A. D. LaLonde, Y. Pei, G. J. Snyder, Reevaluation of $PbTe_{1-x}I_x$ as high performance n-type thermoelectric material, Energ. Environ. Sci. 2011, 4, 2090.

[14] H. Wang, Y. Pei, A. D. LaLonde, G. J. Snyder, Weak electron–phonon coupling contributing to high thermoelectric performance in n-type PbSe, PNAS 2011, 109, 9705.

[15] H. Wang, Y. Pei, A. D. LaLonde, G. J. Snyder, Heavily doped p-type PbSe with high thermoelectric performance: an alternative for PbTe, Adv. Mater. 2011, 23, 1366.

[16] Y. Pei, Z. M. Gibbs, A. Gloskovskii, B. Balke, W. G. Zeier, G. J. Snyder, Optimum Carrier Concentration in n-Type PbTe Thermoelectrics, Adv. Energ. Mater. 2014, 4, 1400486.

[17] J. P. Heremans, V. Jovovic, E. S. Toberer, A. Saramat, K. Kurosaki, A. Charoenphakdee, S. Yamanaka, G. J. Snyder, Enhancement of thermoelectric efficiency in PbTe by distortion of the electronic density of states, Science 2008, 321, 554.

[18] C. J. Vineis, A. Shakouri, A. Majumdar, M. G. Kanatzidis, Nanostructured thermoelectrics: big efficiency gains from small features, Adv. Mater. 2010, 22, 3970.

[19] M. Zebarjadi, K. Esfarjani, M. S. Dresselhaus, Z. F. Ren, G. Chen, Perspectives on thermoelectrics: from fundamentals to device applications, Energy Environ. Sci. 2012, 5, 5147.

[20] W. Liu, X. Yan, G. Chen, Z. Ren, Recent advances in thermoelectric nanocomposites, Nano Energy 2012, 1, 42.

[21] G. Chen, M. S. Dresselhaus, G. Dresselhaus, J. P. Fleurial, T. Caillat, Recent developments in thermoelectric materials, International Materials Reviews 2003, 48, 45.

[22] P. Jood, R. J. Mehta, Y. Zhang, G. Peleckis, X. Wang, R. W. Siegel, T. Borca-Tasciuc, S. X. Dou, G. Ramanath, Al-doped zinc oxide nanocomposites with enhanced thermoelectric properties, Nano Lett. 2011, 11, 4337.

[23] Y. Zhang, X. L. Wang, W. K. Yeoh, R. K. Zheng, C. Zhang, Electrical and thermoelectric properties of single-wall carbon nanotube doped Bi_2Te_3, Appl. Phys. Lett. 2012, 101, 031909.

[24] A. May, J.-P. Fleurial, G. Snyder, Thermoelectric performance of lanthanum telluride produced via mechanical alloying, Phys. Rev. B 2008, 78, 125205.

[25] G. J. Snyder, M. Christensen, E. Nishibori, T. Caillat, B. B. Iversen, Disordered zinc in Zn_4Sb_3 with phonon-glass and electron-crystal thermoelectric properties, Nat. Mater. 2004, 3, 458.

[26] H. Yu, H. Zhang, Z. Wang, J. Wang, Z. Shao, M. Jiang, CW and Q-switched laser output of LD-end-pumped 1.06 μm *c*-cut Nd : $LuV0_4$ laser, Optics Express 2007, 15, 3206.

[27] K. Wu, L. Z. Hao, H. H. Yu, Z. P. Wang, J. Y. Wang, H. J. Zhang, Thermal and laser properties of Nd : $Lu_3Sc_{1.5}Ga_{3.5}O_{12}$ for high power dual-wavelength laser, Optics Express 2012, 20, 6944.

[28] X. Yan, B. Poudel, Y. Ma, W. S. Liu, G. Joshi, H. Wang, Y. Lan, D. Wang, G. Chen, Z. F. Ren, Experimental studies on anisotropic thermoelectric properties and structures of *n*-type $Bi_2Te_{2.7}Se_{0.3}$, Nano Lett. 2010, 10, 3373.

[29] H. Liu, X. Shi, F. Xu, L. Zhang, W. Zhang, L. Chen, Q. Li, C. Uher, T. Day, G. J. Snyder, Copper ion liquid-like thermoelectrics, Nat. Mater. 2012, 11, 422.

[30] B. Yu, W. Liu, S. Chen, H. Wang, H. Wang, G. Chen, Z. Ren, Thermoelectric properties of copper selenide with ordered selenium layer and disordered copper layer, Nano Energy 2012, 1, 472.

[31] D. E. L. D. J. chakrabari, The Cu-Se (Copper-Selenium) system, Bulletin of alloys phase diagrams 1981, 2, 305.

[32] R. D. Heyding, R. M. Murry, The crystal structures of $Cu_{1.8}Se$, Cu_3Se_2, a- and g-CuSe, $CuSe_2$ and $CuSe_2$ II, Can. J. Chem. 1976, 54, 841.

[33] V. M. Glazov, A. S. Pashinkin, V. A. Fedorov, Phase equilibria in the Cu-Se system, Inorg. Mater. 2000, 36, 641.

[34] L. Gulay, M. Daszkiewicz, O. Strok, A. Pietraszko, Crystal structure of Cu_2Se, Chem. Met. Alloys 2011, 4, 200.

[35] G. Lorenz, C. Wagner, Investigations on Cuprous Selenide and Copper Tellurides, J. Chem. Phys. 1957, 26, 1607.

[36] V. N. Konev, V. A. Kudinova, V. I. Neverov, Deviations from Stoichiometry and Effective Mass of Holes in Cu_2S (S + Se) Solid Solutions, lzv. Akad. Nauk SSSR, Neorg. Mater. 1975, 11, 1318.

[37] V. M. Glazov, L. M. Pavlova, A. A. Asryan, Thermal Dissociation of Copper Chalcogenides during Melting, Zh. Fiz Khim. 1996, 70, 5.

[38] X. Xiao, W. Xie, X. Tang, Q. Zhang, Phase transition and high temperature thermoelectric properties of copper selenide $Cu_{2-x}Se$ ($0 \leqslant x \leqslant 0.25$), Chinese Physics B 2011, 20, 087201.

[39] K. Chrissafis, K. M. Paraskevopoulos, C. Manolikas, Studying $Cu_{2-x}Se$ phase transformation through DSC examination, J. Thermal Analysis and Calorimetry 2006, 84, 195.

[40] H. Liu, X. Yuan, P. Lu, X. Shi, F. Xu, Y. He, Y. Tang, S. Bai, W. Zhang, L. Chen, Y. Lin, L. Shi, H. Lin, X. Gao, X. Zhang, H. Chi, C. Uher, Ultrahigh thermoelectric performance by electron and phonon critical scattering in $Cu_2Se_{1-x}I_x$, Adv. Mater. 2013, 25, 6607.

[41] H. Liu, X. Shi, M. Kirkham, H. Wang, Q. Li, C. Uher, W. Zhang, L. Chen, Structure-transformation-induced abnormal thermoelectric properties in semiconductor copper selenide, Materials Letters 2013, 93, 121.

[42] R. J. Mehta, Y. Zhang, C. Karthik, B. Singh, R. W. Siegel, T. Borca-Tasciuc, G. Ramanath, A new class of doped nanobulk high-figure-of-merit thermoelectrics by scalable bottom-up assembly, Nat. Mater. 2012, 11, 233.

[43] J. Androulakis, C. H. Lin, H. J. Kong, C. Uher, C. I. Wu, T. Hogan, B. A. Cook, T. Caillat, K. M. Paraskevopoulos, M. G. Kanatzidis, Spinodal decomposition and nucleation and growth as a means to bulk nanostructured thermoelectrics: enhanced performance in $Pb_{1-x}Sn_xTe$-PbS, J. Am. Chem. Soc. 2007, 129, 9780.

[44] A. Bejan, A. D. Allan, Heat Transfer Handbook, Wiley, New York, 2003.

CHAPTER 5

5 STRUCTURAL, THERMOELECTRIC AND MECHENICAL PROPERTIES FOR THE $CU_{1.98}S_XSE_{1-X}$ ALLOYS

5.1 Preface

The dimensionless thermoelectric figure-of-merit (zT) is related to the Seebeck coefficient, absolute temperature in Kelvin, electrical conductivity, total thermal conductivity, charge carrier thermal conductivity, and lattice thermal conductivity.[1-4] Enhanced zT values could be realized through adjusting the electronic structures and thermal conductivity by the doping approach.[5-9] It should be noted that zT is proportional to the square of S, indicating that improving S might be an easier way to get improved zT values, compared to regulating the other thermoelectric parameters such as σ and κ.

It is well known that σ and S can be estimated by the following formulas,[10-12]

$$\sigma = ne\mu \tag{5-1}$$

$$S = \frac{8\pi^2 k_B^2}{3eh^2} m^* T \left(\frac{\pi}{3n}\right)^{2/3} \tag{5-2}$$

where n, μ, k_B, h, and m^* are the charge carrier density, carrier mobility, Boltzmann constant, Planck constant and effective mass of the carriers, respectively. Moreover, the

carrier mobility (μ) and effective mass (m^*) can be derived from the following equations,[13, 14]

$$\frac{1}{m^*} = \frac{1}{\hbar^2}\frac{d^2E(k)}{d\kappa^2} \quad (5\text{-}3)$$

$$\mu = \frac{q}{m^*}\bar{\tau} \quad (5\text{-}4)$$

where $\hbar$, $E(k)$, q, and $\bar{\tau}$ are the reduced Planck constant or Dirac constant, the energy at the k point of the first Brillouin zone, the elementary charge and the average scattering time, respectively. Furthermore, information on the band gap, effective mass, and charge carrier mobility can be deduced from the band structures and density-of-states (DOS) obtained from related first principle calculations. In this regard, S can be predicted through performing theoretical calculations on the band structures and DOS, and the estimation of σ can also be roughly achieved with considering the average scattering time as a constant. Therefore, it is highly desirable to gain insight into the electronic structures before proceeding to some experiments.

Among all the state-of-the-art high temperature *p*-type thermoelectric materials, the copper-ion-liquid-like $Cu_{2-x}Se$ and $Cu_{2-x}S$ compounds show high thermoelectric performance, even though there still are some issues that need to be resolved before large-scale utilization can be considered.[15] It has been reported that polycrystalline $Cu_{2-x}Se$ and $Cu_{2-x}S$ bulks can achieve the highest zT values of ~ 1.6 and 1.7 at 1000 K,[16, 17] which have been further improved to 1.8 and 1.9,[18, 19] respectively. Additionally, it

should be noted that the high-temperature β-$Cu_{2-x}Se$ and α-$Cu_{2-x}S$ have the same crystal structure, and both of them are superionic conductors. Besides the high crystal symmetry, these two systems also possess another important property, that of congruent melting, which means that highly dense samples can be easily fabricated by a facile melt-solidification technique.

The previous studies[19-21] on the electronic structures for Cu_2Se and Cu_2S compounds indicate that both compounds are zero-gap materials, and the copper deficiency makes them intrinsic p-type conductors owing to the contributions mainly from the Cu 3d-, Se 4p-, and S 3p-states near the Fermi level (E_F). These facts provide evidence that doping other elements into Cu or Se (S) sites could effectively alter their electronic structures, and consequently affect their electrical and thermal transport behaviour as well as their overall thermoelectric performance.

Generally, in order to obtain enhanced S and concurrent high σ as well as low κ values through the doping approach, the following factors should be considered when choosing dopants: (1) Dopants should be heavier than the counterpart element, which will lead to low thermal conductivity owing to the increased mass and decreased mean free path of phonon vibrations. (2) Dopants should have the same valence as the counterpart element, which will ensure the charge balance of the system and maintain the same crystal structure. (3) Dopants should have comparable radiuses to the

counterpart element, which will result in little difference in the lattice parameters and provide good optimization of electronic and thermal transport properties.

As for the $Cu_{2-x}Se$ system, the doping approach, using such elements as Ag, Sb, Al, and Sn for the Cu sites[22-27] and Te and I for the Se sites,[20, 28] has been chosen to modify its electronic structures and thermal conductivity up to now. The results illustrate, however, that only a small amount doping with one of these elements could lead to limited improvements to the thermoelectric performance in this system. Generally, the lighter atoms and heavier atoms should have opposite effects on the electronic and thermal transport properties. For the substitutions on Se sites, only the heavier atoms have been investigated so far, and no enhanced thermoelectric performance was observed except at the phase transition temperatures. Therefore, it is necessary to investigate the doping effects of lighter atoms, with a smaller atomic radius, to test whether or not the doping approach could be beneficial for the further enhancement of the overall thermoelectric performance of the $Cu_{2-x}Se$ system.

In this work, we investigated sulphur doping effects on the thermoelectric properties of the $Cu_{2-x}Se$ system based on the following considerations: (1) At high temperature, α-Cu_2S has the same crystal structure as β-Cu_2Se, and therefore, sulphur should be very easy to substitute into the lattice and replace Se. (2) S^{2-} has the same valence as Se^{2-}, which should result in good electron balance in this system. (3) The unit

cell size should be reduced after S substitutes for Se, which will affect the migration of copper ions and lead to varied electrical and thermal transport behaviour.

It should be noted that, for practical applications of thermoelectric materials, besides the high *zT* values, the thermoelectric compatibility factor (*s*), derived as

$$s = \frac{\sqrt{1+zT}-1}{\alpha \cdot T} \quad (5\text{-}5)$$

where α, *zT, T* are the Seebeck coefficient, dimensionless figure-of-merit, and absolute temperature, respectively. The thermoelectric compatibility factor is another important factor, which is crucial for the efficient operation of a high temperature thermoelectric device.[12, 29-32] The closer the *s* for two *n*- and *p*-type materials, the higher the combined efficiency that will be achieved when they are adjoining segments in one thermoelectric device. Little information on s, however, has been reported for the $Cu_{2-x}Se$ or $Cu_{2-x}S$ based thermoelectric materials. Hence, it is meaningful to calculate the s values for the sulphur doped $Cu_{2-x}Se$ to gain sufficient information for their future practical applications.

Herein, we conducted a systematic study on the sulphur doping effects on the band structures and DOS for the $Cu_{1.875}S_xSe_{1-x}$ compounds using density functional theory (DFT). The doping effects on the thermoelectric properties of highly dense $Cu_{1.98}S_xSe_{1-x}$ polycrystalline bulks were also investigated experimentally, in order to provide a full understanding of how the doping approach modifies the thermoelectric properties of the $Cu_{2-x}Se$ system. Our results indicate that the overall thermoelectric performance in

$Cu_{1.98}S_xSe_{1-x}$ is strongly dependent on the sulphur doping concentration, and it is mainly correlated with the electron effective mass and DOS.

5.2 Experimental

5.2.1 Sample fabrications

Polycrystalline $Cu_{1.98}S_xSe_{1-x}$ pellets were synthesized by a conventional solid-state method. Mixtures of Cu, S, and Se powders in the molar ratios of 1.98 : x : 1-x (x = 0, 0.02, 0.08, 0.16, 0.2, 0.3, 0.4, 0.5, 0.6, 0.7 0.8, 0.9, 1.0) were pressed into pellets and sealed in evacuated quartz tubes, then heated to 873 K for 1-5 hours with a heating rate of 5 K/min, followed by a furnace cooling to room temperature. Finally, the as-sintered pellets were used in a melt-solidification approach to achieve highly dense polycrystalline bulks, which has been described in detail in our previous work.[18, 20] The obtained polycrystalline bulks were then shaped into round disks and rectangular bulks for electrical conductivity and thermal diffusivity measurements, respectively.

5.2.2 Measurements

X-ray diffraction (XRD) patterns were collected on a GBC MMA system using Cu Kα radiation. The electrical conductivity and Seebeck coefficient were measured simultaneously in a helium atmosphere from 300 to 973 K using an RZ2001i system. The thermal diffusivity (D) was measured by the laser flash method (LINSEIS LFA

1000), and the specific heat (*C*p) was determined by differential scanning calorimetry (NETZSCH DSC 204F1). The sample density (*dd*) was determined by the Archimedes method, and the thermal conductivity (κ) was calculated according to $\kappa = D \times Cp \times dd$.

5.2.3 Calculation details

The calculations of band structures, and total and partial DOS were performed based on the DFT method, implemented by the CASTEP package[33] with the generalized gradient approximation (GGA).[34] The calculations were parameterized by the Perdew-Burke-Ernzerhof (PBE)[35] and ultra-soft pseudo-potentials. The plane wave cut-off energy was set at 400 eV. For Cu_2Se and Cu_2S, a primitive cell with the Brillouin zone path of ΓXWLΓK was employed for the band structure calculations. For the $Cu_{15}S_xSe_{8-x}$ (x = 0, 1, 2, 4, 6, 8), geometry optimizations were performed on a 2×2×2 supercell, with one copper atom deleted, of the Cu_2Se primitive cell. Then, the Brillouin zone path of ΓXWLΓK and a k-point set of 15×15×15 for the supercell were used to calculate the band structures, and the total and partial DOS, respectively.

5.3 Results and discussion

5.3.1 First principles calculations

Figure 5-1 shows a perspective view of the crystal structures for the cubic structured Cu_2Se(S), as well as the ideal versions of the unit cell[21] and the

primitive cell. It indicates that, in the ideal version of the unit cell for the cubic structured $Cu_2Se(S)$ with space group of $Fm\bar{3}m$, the selenium (sulphur) atoms form a face-centred cubic (*fcc*) sub-lattice, and the copper atoms occupy the tetrahedral interstitial positions. It should, however, be noted that β-Cu_2Se and α-Cu_2S have been reported to be superionic conductors, in which the copper ions behave like a liquid,[16, 18, 36-38] and they are kinetically disordered throughout the whole structure.

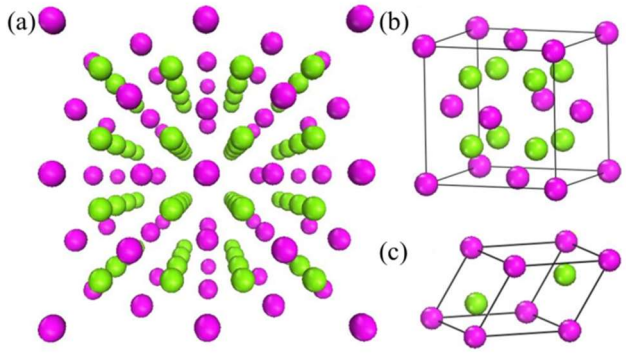

Figure 5-1 (a) Perspective view of the crystal structure for high temperature cubic structured $Cu_2Se(S)$. (b) Ideal version of the unit cell for the cubic structured $Cu_2Se(S)$. (c) Primitive cell for the cubic structured $Cu_2Se(S)$. Cu and Se(S) atoms are represented by green and purple spheres, respectively.

Figure 5-2 and Figure 5-3 display the calculated total and partial DOS for the $Cu_{15}S_xSe_{8-x}$ (x = 1, 2, 4, 6) compounds. It indicates that, for all the compounds, the valence bands consist of three regions: a lower region between 12 and 16 eV below the E_F, which is mainly constituted by Se 4s-states, a middle region between 4 and 8 eV below the E_F, which is a mixture of states that come from Cu,

Se, and S, and an upper region from the E_F down to -4 eV, which mostly consists of Cu 3d-states with some contributions from Se 4p-states and S 3p-states. Furthermore, the upper region penetrates into the E_F, mainly due to the contributions of Cu 3d-states and Se 4p-states, indicating that all these copper deficient sulphur doped $Cu_{15}Se_8$ compounds should be intrinsic *p*-type conductors. In addition, similar to the Se 4s- and 4p-states, the S 3s- and 3p-states also make contributions to all these three regions of the valence bands, with 3s-states for the lower region and 3p-states for the middle and upper regions, respectively.

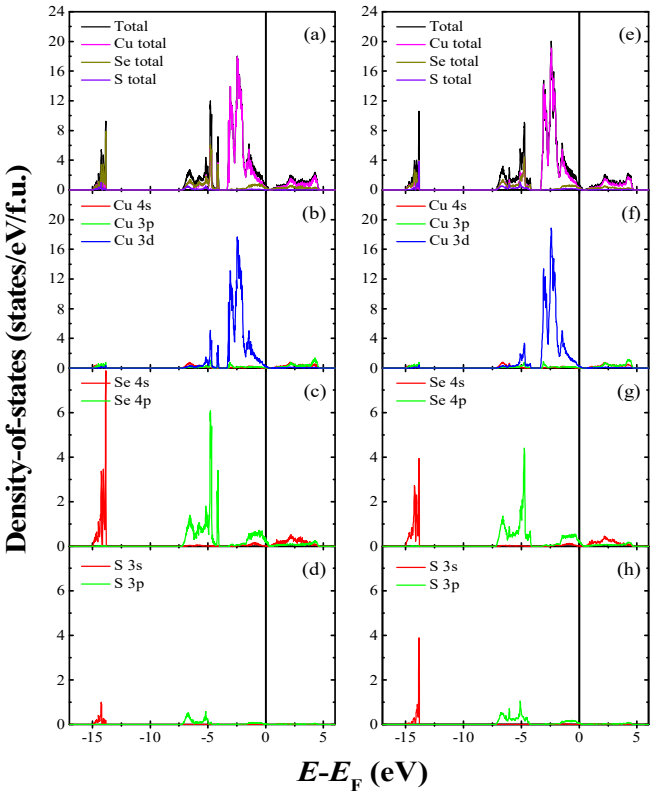

Figure 5-2 Calculated total and partial density-of-states (DOS) for the $Cu_{15}S_xSe_{8-x}$ (x = 1, 2) compounds obtained from the density functional theory calculations. (a, b, c, d) total and partial DOS for the $Cu_{15}S_1Se_7$. (e, f, g, h) total and partial DOS for the $Cu_{15}S_2Se_6$.

The total DOS for the Cu, Se, and S atoms are displayed, and the partial DOS for the 4s-, 3p-, and 3d-states of Cu, the 4s- and 4p-states of Se, and the 3s- and 3p-states of S are also presented. The vertical lines mark the position of the Fermi level (E_F).

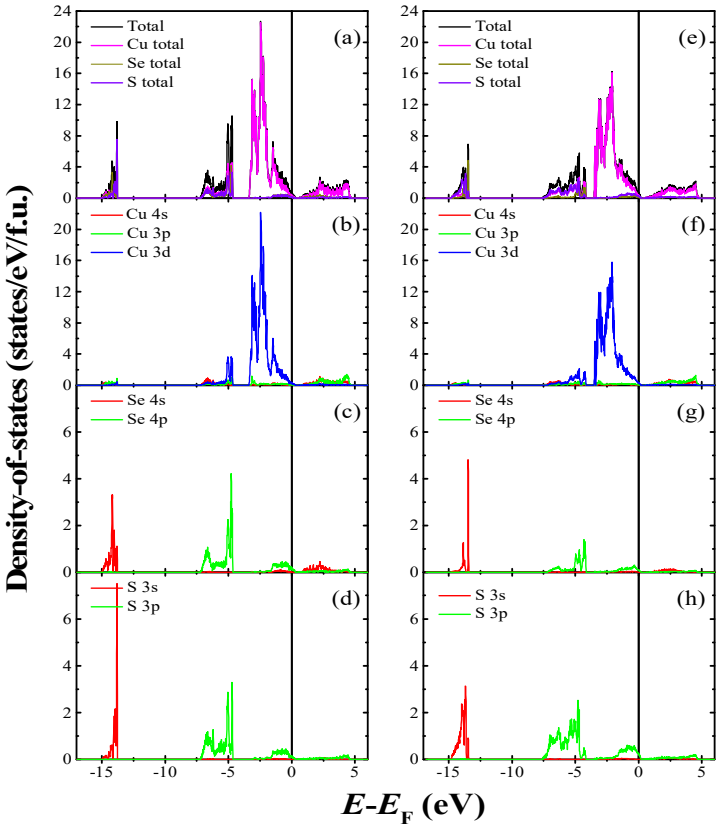

Figure 5-3 Calculated total and partial density-of-states (DOS) for the $Cu_{15}S_xSe_{8-x}$ (x = 4, 6) compounds obtained from the density functional theory calculations. (a, b, c, d) total and partial DOS for the $Cu_{15}S_4Se_4$. (e, f, g, h) total and partial DOS for the $Cu_{15}S_6Se_2$. The total DOS for the Cu, Se, and S atoms are displayed, and the partial DOS for the 4s-, 3p-, and 3d-states of Cu, the 4s- and 4p-states of Se, and the 3s- and 3p-states of S are also presented. The vertical lines mark the position of the Fermi level (E_F).

Figure 5-4 shows the sulphur doping level dependence of the total and partial DOS near E_F for the $Cu_{15}S_xSe_{8-x}$ (x = 0, 1, 2, 4, 6, 8) compounds. The partial DOS for the S atoms obviously increases with increasing x, while the partial DOS for the Se atoms shows the opposite trend, decreasing with increasing x. The total DOS exhibits the same non-monotonic tendency as the partial DOS for the Cu atoms, indicating that the DOS near E_F for this system is mainly determined by the copper atoms rather than the S or Se atoms. The total DOS firstly increases slightly, and then clearly decreases, with the $Cu_{15}S_6Se_2$ having the highest DOS among all the compounds, ~ 0.69 states/eV/f.u..

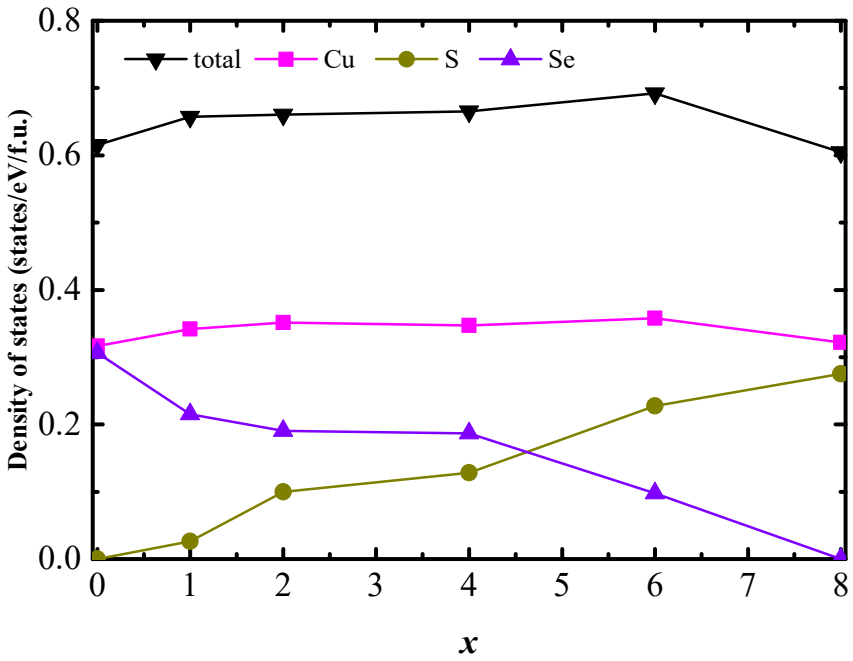

Figure 5-4 Sulphur doping level dependence of the total and partial density-of-states near the Fermi level for the $Cu_{15}S_xSe_{8-x}$ (x = 0, 1, 2, 4, 6, 8) compounds.

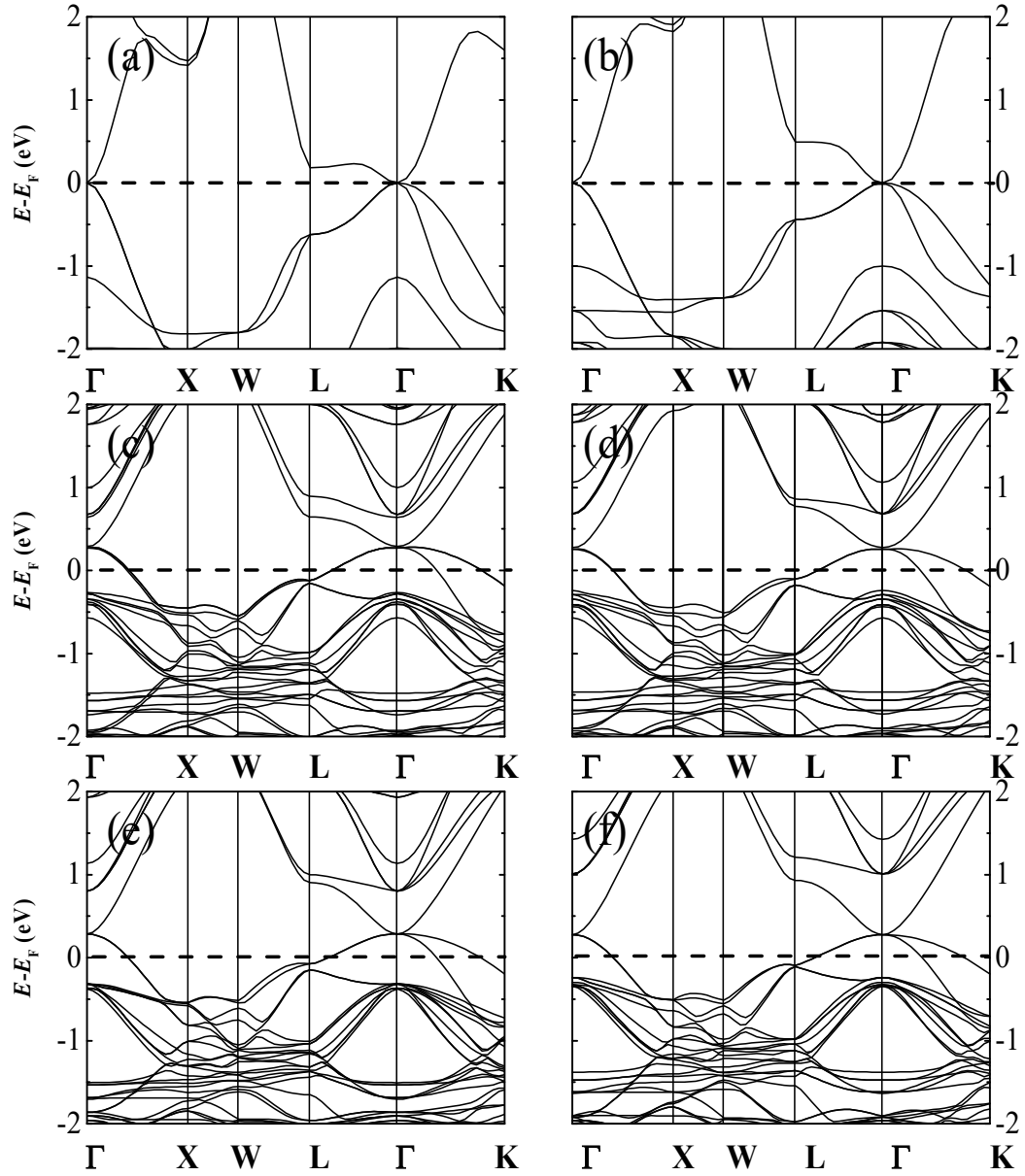

Figure 5-5 Typical calculated band structures for the Cu_2Se, Cu_2S, and $Cu_{15}S_xSe_{8-x}$ (x = 0, 1, 4, 8) compounds. (a) Calculated band structure for Cu_2Se. (b) Calculated band structure for Cu_2S. (c) Calculated band structure for $Cu_{15}Se_8$. (d) Band structure for the $Cu_{15}S_1Se_7$. (e) Band structure for $Cu_{15}S_4Se_4$. (f) Band structure for $Cu_{15}S_8$. Figure 5-5Figure 5-5 shows the typical calculated band structures for the Cu_2Se, Cu_2S, and $Cu_{15}S_xSe_{8-x}$ (x = 0, 1, 4, 8) compounds. The results provide further evidence that the

stoichiometric Cu_2Se and Cu_2S are zero-gap materials, while all the copper deficient compounds are intrinsic *p*-type conductors, which agrees well with the previous conclusions deduced from the calculated DOS. Based on the definition of effective mass (shown in Equation 5-3), we know that the effective mass can be easily derived from the calculated band structures.

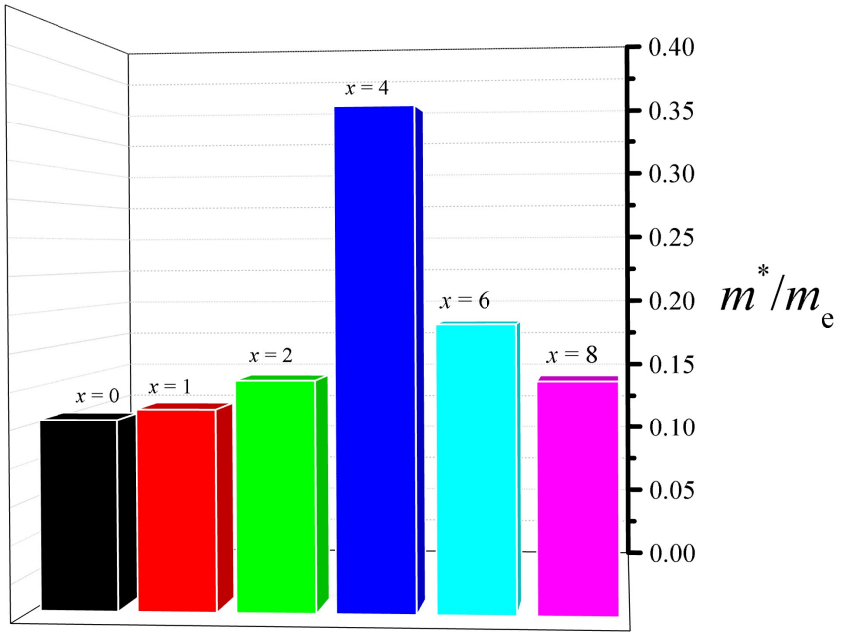

Figure 5-6 Calculated effective mass for the $Cu_{15}S_xSe_{8-x}$ (x = 0, 1, 2, 4, 6, 8) compounds.

Figure 5-6 displays the deduced effective mass for the $Cu_{15}S_xSe_{8-x}$ (x = 0, 1, 2, 4, 6, 8) compounds. It indicates that, similar to the DOS, the sulphur doping also has a non-monotonic effect on the effective mass. It firstly has positive effects and gives the $Cu_{15}S_4Se_4$ its highest m^*, with a value of ~ 0.336 m_e. It then shows negative effects and results in decreased m^* values as the sulphur doping level increases.

According to Equations 5-1 to 5-4 and discussions on σ, S, and n as well as μ, we know that for certain thermoelectric compounds, both σ and S are related to the m^* and the DOS. Specifically, σ is proportional to the carrier density (n), which is related to the DOS at E_F, and it is also inversely proportional to m^*. S, however, is proportional to m^* and $\left(\frac{1}{n}\right)^{2/3}$. Therefore, based on the obtained information on the DOS and m^*, we can anticipate the trends for the variation of S. σ values can also be roughly estimated with disregarding the average scattering time. The cubic structured sulphur doped $Cu_{2-x}Se$ compounds should exhibit non-monotonic variation in σ and S with increasing sulphur concentration according to the calculated DOS and m^* using the DFT method.

5.3.2 Structural properties

Figure 5-7 shows the X-ray diffraction (XRD) patterns for the fabricated $Cu_{1.98}S_xSe_{1-x}$ (x = 0, 0.02, 0.08, 0.16, 0.2, 0.3, 0.4, 0.5, 0.6, 0.7, 0.8, 0.9, 1.0) samples. A summarized phase diagram for the sulphur doping level dependence of the crystal structures is shown in Figure 5-8. The results indicate that the $Cu_{1.98}S_xSe_{1-x}$ samples show different crystal structures with different x values. They are single-phase and have the same monoclinic[39] crystal structure as the low temperature α-phase $Cu_{2-x}Se$ (PDF No.: 27-1131[22]) when $x \leq 0.16$. They then become composites of low temperature cubic structured $Cu_{1.8}Se$ and hexagonal structured $Cu_{2.001}S$ when x varies in the range from 0.2 to 0.7 ($0.2 \leq x \leq 0.7$). Finally, they become single-phase orthorhombic structured Cu_2S (PDF: 23 - 961) when x is over 0.8.

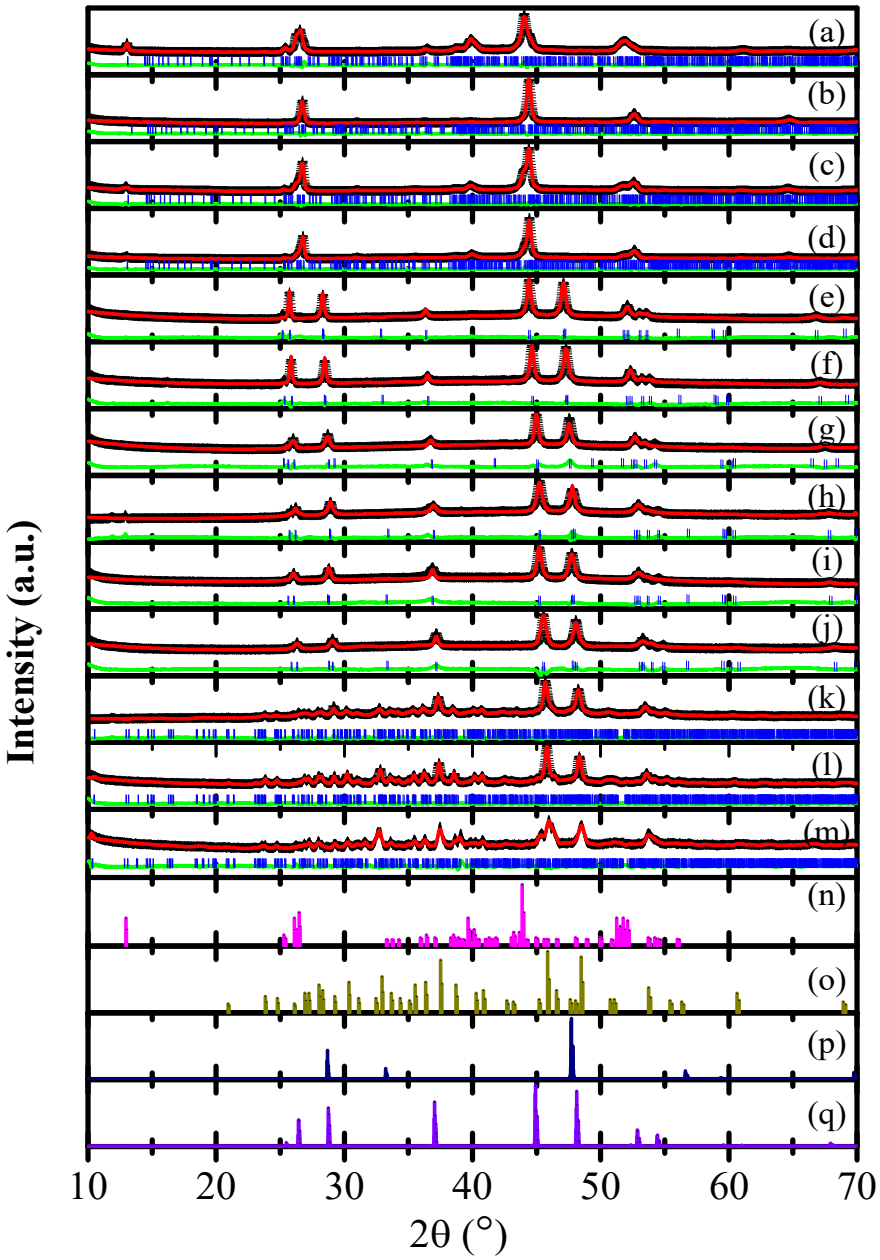

Figure 5-7 X-ray diffraction (XRD) patterns of the fabricated $Cu_{1.98}S_xSe_{1-x}$ (x = 0, 0.02, 0.08, 0.16, 0.2, 0.3, 0.4, 0.5, 0.6, 0.7, 0.8, 0.9, 1.0) samples: (a) $Cu_{1.98}Se$, (b) $Cu_{1.98}S_{0.02}Se_{0.98}$, (c) $Cu_{1.98}S_{0.08}Se_{0.92}$, (d) $Cu_{1.98}S_{0.16}Se_{0.84}$, (e) $Cu_{1.98}S_{0.2}Se_{0.8}$, (f) $Cu_{1.98}S_{0.3}Se_{0.7}$, (g) $Cu_{1.98}S_{0.4}Se_{0.6}$, (h) $Cu_{1.98}S_{0.5}Se_{0.5}$, (i) $Cu_{1.98}S_{0.6}Se_{0.4}$, (j) $Cu_{1.98}S_{0.7}Se_{0.3}$, (k) $Cu_{1.98}S_{0.8}Se_{0.2}$, (l) $Cu_{1.98}S_{0.9}Se_{0.1}$, (m) $Cu_{1.98}S$, (n) standard XRD pattern for

monoclinic structured Cu_2Se, (o) standard XRD pattern for orthorhombic structured Cu_2S, (p) standard XRD pattern for cubic structured $Cu_{1.8}Se$, and (q) standard XRD pattern for hexagonal structured $Cu_{2.001}S$. (+ data points, — calculation line, — difference line, | marker points).

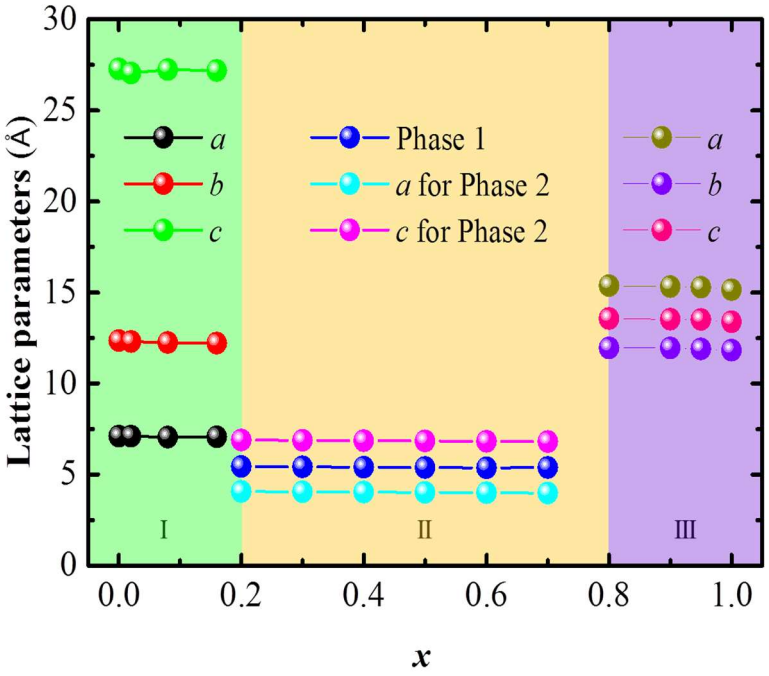

Figure 5-8 Phase diagram of sulphur doping level dependence of the crystal structures at room temperature. (I: monoclinic structured Cu_2Se phase; II: Composites of cubic structured $Cu_{1.8}Se$ (Phase 1) and hexagonal structured $Cu_{2.001}S$ (Phase 2); III: orthorhombic structured Cu_2S phase).

Rietveld refinements were performed for all samples based on the obtained X-ray diffraction patterns and the deduced lattice parameters, and the R-factors are listed in Table 5-1. The phase diagram for the sulphur doping level dependence of the lattice parameters is also displayed in Figure 5-8. The results reveal that the $Cu_{1.98}S_xSe_{1-x}$ (x =

0.02, 0.08, 0.16) samples have slightly reduced lattice parameters in comparison with the $Cu_{1.98}Se$ sample, due to the smaller radius of sulphur compared to that of selenium. In the same way, the $Cu_{1.98}S_{0.8}Se_{0.2}$ and $Cu_{1.98}S_{0.9}Se_{0.1}$ samples have enlarged lattice parameters in contrast to the $Cu_{1.98}S$ sample, owing to the larger radius of selenium.

Table 5-1 Lattice parameters, and profile (R_p) and weighted profile (R_{wp}) R-factors for the $Cu_{1.98}S_xSe_{1-x}$ (x = 0, 0.02, 0.08, 0.16, 0.2, 0.3, 0.4, 0.5, 0.6, 0.7, 0.8, 0.9, 1.0) samples deduced from Rietveld refinements of the XRD patterns. (Phase 1: cubic structured $Cu_{1.8}Se$, Phase 2: hexagonal structured $Cu_{2.001}S$).

Sample		a (Å)	b (Å)	c (Å)	β (°)	V (Å^3)	R_p	R_{wp}
$Cu_{1.98}Se$		7.117(7)	12.358(6)	27.278(2)	94.112(6)	2393.3(4)	1.820	2.793
$Cu_{1.98}S_{0.02}Se_{0.98}$		7.101(2)	12.301(4)	27.044(0)	94.193(3)	2356.1(0)	3.115	4.536
$Cu_{1.98}S_{0.08}Se_{0.92}$		7.050(5)	12.251(1)	27.237(8)	94.182(7)	2346.4(4)	2.745	3.600
$Cu_{1.98}S_{0.16}Se_{0.84}$		7.072(2)	12.223(9)	27.185(6)	94.186(6)	2343.9(2)	2.556	3.378
$Cu_{1.98}S_{0.2}Se_{0.8}$	Phase 1	5.435(3)	5.435(3)	5.435(3)	90.0(0)	160.5(7)	2.594	3.472
	Phase 2	4.069(1)	4.069(1)	6.891(8)	120.0(0)	98.8(2)		
$Cu_{1.98}S_{0.3}Se_{0.7}$	Phase 1	5.430(2)	5.430(2)	5.430(2)	90.0(0)	160.1(2)	2.917	3.769
	Phase 2	4.056(7)	4.056(7)	6.879(4)	120.0(0)	98.0(5)		
$Cu_{1.98}S_{0.4}Se_{0.6}$	Phase 1	5.415(2)	5.415(2)	5.415(2)	90.0(0)	158.8(0)	2.713	3.687
	Phase 2	4.036(8)	4.036(8)	6.859(9)	120.0(0)	96.8(1)		
$Cu_{1.98}S_{0.5}Se_{0.5}$	Phase 1	5.387(0)	5.387(0)	5.387(0)	90.0(0)	156.3(3)	2.398	3.260
	Phase 2	4.022(7)	4.022(7)	6.846(3)	120.0(0)	95.9(4)		
$Cu_{1.98}S_{0.6}Se_{0.4}$	Phase 1	5.368(8)	5.368(8)	5.368(8)	90.0(0)	154.7(5)	3.493	4.429
	Phase 2	4.003(3)	4.003(3)	6.820(0)	120.0(0)	94.6(6)		
$Cu_{1.98}S_{0.7}Se_{0.3}$	Phase 1	5.390(7)	5.390(7)	5.390(7)	90.0(0)	156.6(5)	2.939	4.243
	Phase 2	3.993(5)	3.993(5)	6.806(2)	120.0(0)	94.0(0)		
$Cu_{1.98}S_{0.8}Se_{0.2}$		15.375(0)	11.954(3)	13.562(1)	116.278(2)	2235.0(7)	1.644	4.779
$Cu_{1.98}S_{0.9}Se_{0.1}$		15.317(9)	11.929(1)	13.536(2)	116.356(1)	2216.3(4)	1.546	2.214
$Cu_{1.98}S$		15.155(7)	11.828(9)	13.401(1)	115.955(7)	2160.15(3)	2.565	3.555

5.3.3 Thermoelectric properties

Since both $Cu_{2-x}Se$ and $Cu_{2-x}S$ are superionic conductors, and the migration of copper ions plays important roles on the system's electrical conductivity, the changed lattice parameters should lead to different electrical conductivity and Seebeck coefficient, which will, in turn, result in modified thermoelectric properties with different *zT* values. Thus, it is essential to discuss the sulphur doping effects on the thermoelectric properties of the $Cu_{2-x}Se$ system, as well as the selenium doping effects on the thermoelectric properties of the $Cu_{2-x}S$ system. Hence, we will focus on the thermoelectric properties of the single-phase $Cu_{1.98}S_xSe_{1-x}$ (x = 0.02, 0.08, 0.16) and $Cu_{1.98}S_xSe_{1-x}$ (x = 0.8, 0.9, 1.0) samples in the following part.

5.3.3.1 Thermoelectric properties for the $Cu_{1.98}S_xSe_{1-x}$ (x = 0.02, 0.08, 0.16) bulks

Figure 5-9 shows the temperature dependence of the specific heat for the obtained $Cu_{1.98}S_xSe_{1-x}$ (x = 0, 0.02, 0.08, 0.16) bulks. It indicates that the $Cu_{1.98}S_xSe_{1-x}$ (x = 0.02, 0.08, 0.16) samples have much higher C_p values compared to the $Cu_{1.98}Se$ sample. Furthermore, all the $Cu_{1.98}S_xSe_{1-x}$ samples show a phase transition in the temperature range from 350 to 400 K, and generally, the transition temperature for the sulphur doped $Cu_{1.98}Se$ are much lower compared to the $Cu_{1.98}Se$. This might be related to the reduced lattice parameters and defects in the $Cu_{1.98}S_xSe_{1-x}$ (x = 0.02, 0.08, 0.16) samples.

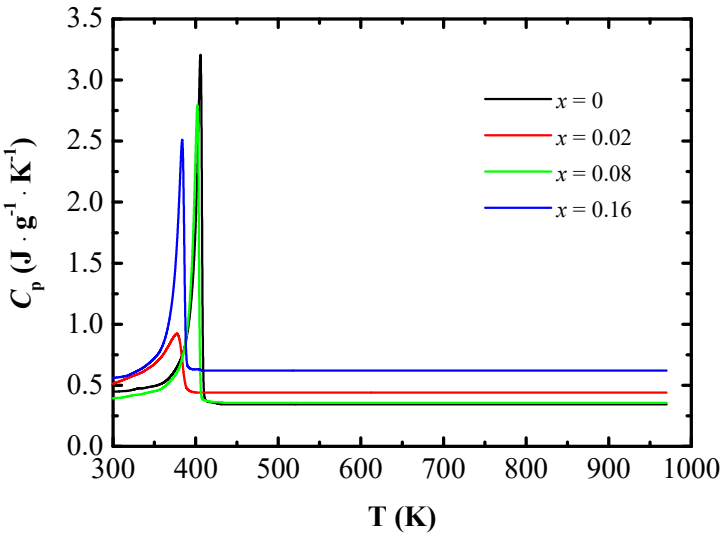

Figure 5-9 Temperature dependence of the specific heat for the obtained $Cu_{1.98}S_xSe_{1-x}$ (x = 0, 0.02, 0.08, 0.16) bulks.

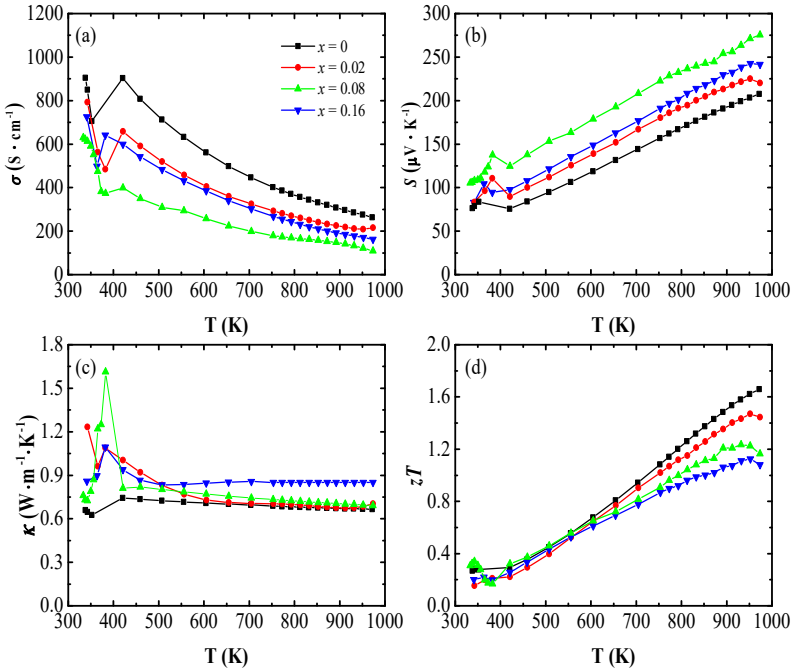

Figure 5-10 Temperature dependence of thermoelectric properties for the obtained $Cu_{1.98}SxSe_{1-x}$ (x = 0, 0.02, 0.08, 0.16) bulks: (a) electrical conductivity (σ), (b) Seebeck

coefficient (*S*), (c) total thermal conductivity (κ), and (d) dimensionless figure-of-merit (*zT*).

Figure 5-10(a) shows the temperature dependence of the electrical conductivity for the $Cu_{1.98}S_xSe_{1-x}$ (x = 0, 0.02, 0.08, 0.16) bulks. It indicates that compared to $Cu_{1.98}Se$, the $Cu_{1.98}S_xSe_{1-x}$ (x = 0.02, 0.08, 0.16) samples have lower σ values over the whole measured temperature range, and the most obvious difference occurs at T = 420 K between 400 $S \cdot cm^{-1}$ for the $Cu_{1.98}S_{0.08}Se_{0.92}$ and 900 $S \cdot cm^{-1}$ for the $Cu_{1.98}Se$. It should be pointed out that this difference becomes less obvious with increasing temperature because the high temperature phases are superionic conductors.

Figure 5-10(b) displays the temperature dependence of the Seebeck coefficient for the $Cu_{1.98}S_xSe_{1-x}$ (x = 0, 0.02, 0.08, 0.16) bulks. It reveals that the $Cu_{1.98}S_xSe_{1-x}$ (x = 0.02, 0.08, 0.16) samples have larger S values than the $Cu_{1.98}Se$. Specifically, among all the samples, the $Cu_{1.98}S_{0.08}Se_{0.92}$ has the highest S, around 275 $\mu V \cdot K^{-1}$ at T = 970 K, which is over 30% higher than that of the $Cu_{1.98}Se$.

It should be pointed out that, for the monoclinic structured Cu_2Se phased $Cu_{1.98}S_xSe_{1-x}$ samples, the observed sulphur doping level dependence of the electrical conductivity and the Seebeck coefficient is in good agreement with our previous theoretical predictions. The DOS is enhanced as the sulphur doping level increases, while the effective mass is reduced as the doping level increases. Additionally, σ and *S* are proportional to $\frac{n}{m^*}$ and m^*, respectively. Therefore, when the contribution from the

effective mass is higher than that from the DOS, σ should be decreased and S should be increased concurrently.

Figure 5-10(c) shows the temperature dependence of the thermal conductivity for the $Cu_{1.98}S_xSe_{1-x}$ (x = 0, 0.02, 0.08, 0.16) bulks. It indicates that both the $Cu_{1.98}S_{0.02}Se_{0.98}$ and $Cu_{1.98}S_{0.08}Se_{0.92}$ bulks have almost the same κ values as the $Cu_{1.98}Se$, especially in the temperature range from 500 to 1000 K. The $Cu_{1.98}S_{0.16}Se_{0.84}$, however, shows increased values over the whole temperature range from 300 to 1000 K.

The temperature dependence of the dimensionless figure-of-merit (zT) for the $Cu_{1.98}S_xSe_{1-x}$ (x = 0, 0.02, 0.08, 0.16) bulks is shown in Figure 5-10(d). It should be noted that the $Cu_{1.98}S_xSe_{1-x}$ (x = 0.02, 0.08, 0.16) samples show almost the same zT values as the $Cu_{1.98}Se$ in the temperature range from 400 to 600 K. Furthermore, they have zT values over 1.0 when T > 800 K and exhibit a peak zT at T around 950 K, with the highest value of 1.5 occurring for the $Cu_{1.98}S_{0.02}Se_{0.98}$.

5.3.3.2 Thermoelectric properties for the Cu1.98SxSe1-x (x = 0.8, 0.9, 1.0) bulks

Figure 5-11 shows the temperature dependence of the specific heat for the obtained $Cu_{1.98}S_xSe_{1-x}$ (x = 0.8, 0.9, 1.0) bulks. The results indicate that all the $Cu_{1.98}S_xSe_{1-x}$ (x = 0.8, 0.9, 1.0) bulks have almost the same C_p values in the whole measured temperature range except the phase transition temperatures. For the first phase transition happened at temperatures lower than 400 K, the phase transition temperature for the $Cu_{1.98}S_xSe_{1-x}$ (x

= 0.8, 0.9, 1.0) samples increased as the selenium doping level, x, increases. The transition temperatures for the second phase transition are almost the same for all the $Cu_{1.98}S_xSe_{1-x}$ (x = 0.8, 0.9, 1.0) samples. It should be pointed out that, in the temperature range from 700 to 1000 K, all the $Cu_{1.98}S_xSe_{1-x}$ (x = 0.8, 0.9, 1.0) samples have stable C_p values, with the $Cu_{1.98}S_xSe_{1-x}$ (x = 0.8, 0.9) samples having a little bit lower values compared to the $Cu_{1.98}S$. This might be related to the enlarged lattice parameter and other defects existed in the samples. This is in good agreement with what we observed in the $Cu_{1.98}S_xSe_{1-x}$ (x = 0, 0.02, 0.08, 0.16) bulks.

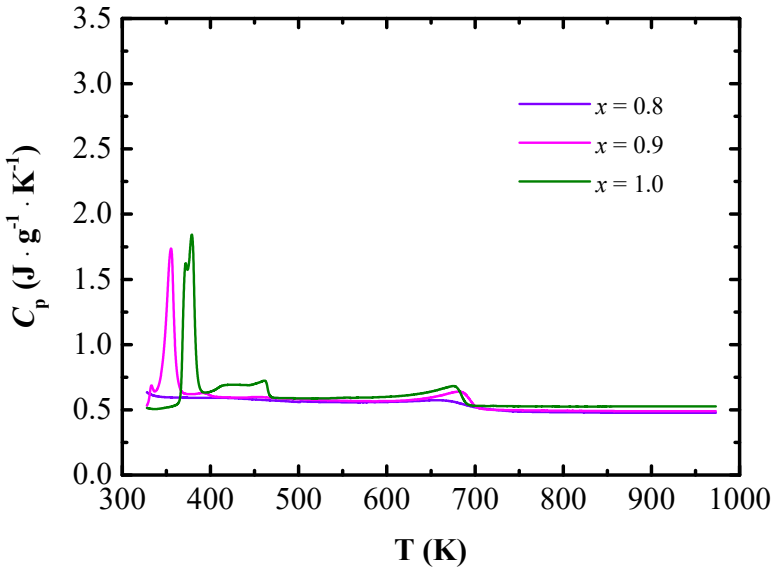

Figure 5-11 Temperature dependence of the specific heat for the obtained $Cu_{1.98}S_xSe_{1-x}$ (x = 0.8, 0.9, 1.0) bulks.

Figure 5-12 displays the temperature dependence of the electrical conductivity (a), Seebeck coefficient (b), total thermal conductivity (c), and dimensionless figure-of-merit (d) for the obtained $Cu_{1.98}S_xSe_{1-x}$ (x = 0.8, 0.9, 1.0) bulks. The results indicate that,

for the high temperature cubic structured Cu_2S phase, the $Cu_{1.98}S_xSe_{1-x}$ samples do not show a monotonic increase or decrease in their electrical conductivity compared to the $Cu_{1.98}S$. The same trend is also observed for the temperature dependence of the Seebeck coefficient. This non-monotonic trend can be ascribed to the competition between the enhancement of the DOS and the effective mass. Enhanced electrical conductivity and a reduced Seebeck coefficient can be obtained when the contribution from the DOS is stronger than that from the effective mass. When the contribution of the effective mass is stronger, decreased electrical conductivity and increased Seebeck coefficient will be achieved.

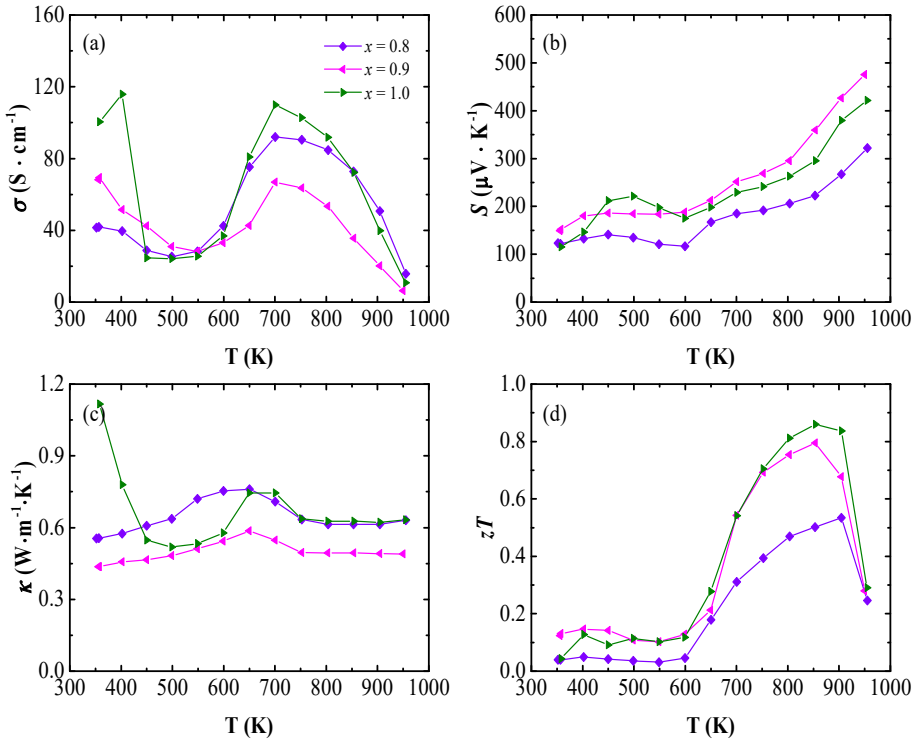

Figure 5-12 Temperature dependence of the thermoelectric properties for the obtained $Cu_{1.98}S_xSe_{1-x}$ (x = 0.8, 0.9, 1.0) bulks: (a) electrical conductivity (σ), (b) Seebeck

coefficient (S), (c) total thermal conductivity (κ), and (d) dimensionless figure-of-merit (zT).

In the temperature range from 700 to 1000 K, the $Cu_{1.98}S_{0.8}Se_{0.2}$ sample has almost the same thermal conductivity as the $Cu_{1.98}S$, while the $Cu_{1.98}S_{0.9}Se_{0.1}$ sample has much smaller thermal conductivity, with values around $0.5 W \cdot m^{-1} \cdot K^{-1}$. This paradoxical result might be related to the characteristics of the superionic system and the larger radius as well as the heavier mass of selenium compared to sulphur. As aforementioned, the cubic structured Cu_2S is a superionic conductor and it is the migration of copper ions that determines the thermal conductivity of this system. Therefore, the selenium doped samples should have higher thermal conductivity than the $Cu_{1.98}S$, due to the enlarged lattice parameters evidenced from the refinements of the X-ray diffraction patterns. On the other hand, selenium is much heavier than sulphur, so the selenium doped samples should have lower thermal conductivity. As a result of these two opposite factors, the samples show the complicated and varying trend that is observed for the thermal conductivity.

The temperature dependence of the dimensionless figure-of-merit indicates that the selenium doping does not improve the thermoelectric performance of the $Cu_{1.98}S$ system, with the $Cu_{1.98}S$ having the highest zT value around 0.86 at 850 K among all the orthorhombic structured samples, even though certain thermoelectric parameters are enhanced. This is in good agreement with our previous reports on the tellurium and

iodine doped $Cu_{2-x}Se$ system[20], which provides further evidence of the distinctiveness of superionic thermoelectric materials in comparison with the conventional thermoelectric materials. Figure 5-13 shows a summarized phase diagram for the sulphur doping level dependence of the dimensionless figure-of-merit for the obtained $Cu_{1.98}S_xSe_{1-x}$ (x = 0, 0.02, 0.08, 0.16, 0.8, 0.9, 1.0) samples. It indicates that the zT values are first reduced as x increases from 0 to 0.16, and then they are enhanced as x increases from 0.8 to 1.0, which agrees very well with our previous theoretical and experimental discussions on sulphur (selenium) doping effects on the superionic $Cu_{2-x}Se(S)$ system.

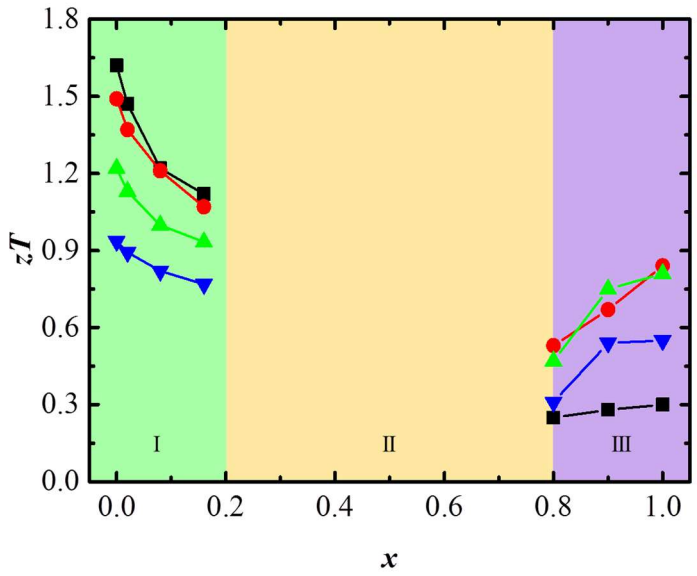

Figure 5-13 Phase diagram of the Sulphur doping level dependence of the dimensionless figure-of-merit (zT).

For the practical applications of thermoelectric materials, besides the high zT values that are needed, the thermoelectric compatibility factor, s, is another important

factor that needs to be considered when designing an efficient thermoelectric generator.[12, 31, 40] The maximum efficiency of a thermoelectric generator will be decreased greatly if the compatibility factors for the segments of *n*- and *p*-type thermoelectric materials differ from each other by a factor larger than two. Therefore, in order to discover the best applicable temperature range and best matching material for a certain thermoelectric material, the calculation of *s* is essential.

5.3.3.3 Thermoelectric compatibility factors for the $Cu_{1.98}S_xSe_{1-x}$ (x = 0, 0.02, 0.08, 0.16, 0.8, 0.9, 1.0) bulks.

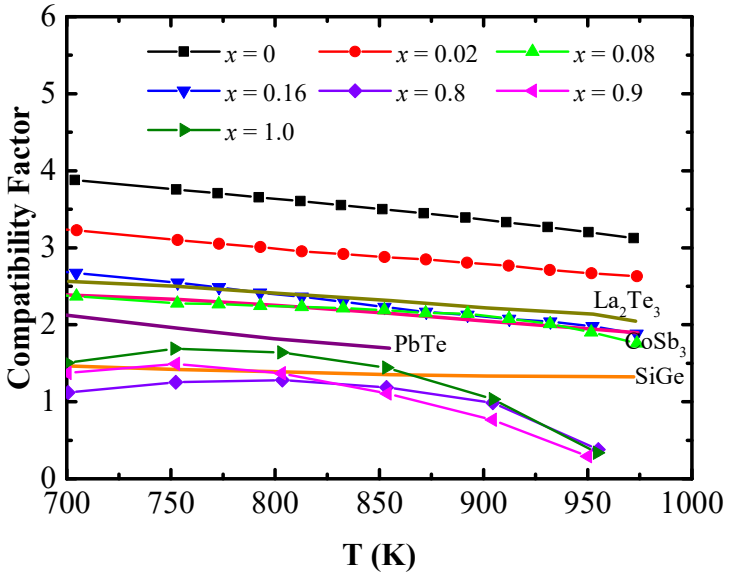

Figure 5-14 Temperature dependence of the thermoelectric compatibility factor for the $Cu_{1.98}S_xSe_{1-x}$ (x = 0, 0.02, 0.08, 0.16, 0.8, 0.9, 1.0) samples.

Figure 5-14 shows the temperature dependence of the thermoelectric compatibility factor for the $Cu_{1.98}S_xSe_{1-x}$ (x = 0, 0.02, 0.08, 0.16, 0.8, 0.9, 1.0) bulks. It indicates that all the samples exhibit stable s values with small fluctuations over a large temperature

range from 700 to 1000 K. In the measured temperature range, average s values of around 3.85, 2.92, 2.14, and 2.56 were achieved for the Cu_2Se-phase $Cu_{1.98}Se$, $Cu_{1.98}S_{0.02}Se_{0.98}$, $Cu_{1.98}S_{0.08}Se_{0.92}$, and $Cu_{1.98}S_{0.16}Se_{0.84}$ samples, respectively. Furthermore, the Cu_2S-phase samples $Cu_{1.98}S_{0.8}Se_{0.2}$, $Cu_{1.98}S_{0.9}Se_{0.1}$, and $Cu_{1.98}S$ exhibit average s values of ~ 0.72, 0.87, and 0.93 in the temperature range from 700 to 1000 K, respectively.

For comparison purposes, the s values for some well-known n-type thermoelectric materials are also provided in Figure 5-14 . It indicates that polycrystalline SiGe, PbTe, La_2Te_3, and $CoSb_3$ bulks show s of ~ 1.37, 1.90, 2.14, and 2.31, respectively. It should be noted that these are very close to the s values of the $Cu_{1.98}S_xSe_{1-x}$ (x = 0, 0.02, 0.08, 0.16, 0.8, 0.9, 1.0) bulks, with the differences less than a factor of 2 in the temperature range from 700 to 1000 K. Therefore, a relatively high efficiency could be gained from their coupled thermoelectric modules, which is gratifying for their future practical applications.

5.4 Conclusions

In summary, our DFT calculations indicate that all the copper deficient $Cu_{15}S_xSe_{8-x}$ compounds are intrinsic *p*-type conductors. Sulphur doping has non-monotonic effects on the DOS and m^*, with the $Cu_{15}S_6Se_2$ and $Cu_{15}S_4Se_4$ having the highest DOS value, ~ 0.69 states/eV/f.u., and the highest m^*, ~ 0.336 m_e, respectively. The $Cu_{1.98}S_xSe_{1-x}$ compounds have the same crystal structure as

monoclinic structured Cu_2Se when $x \leq 0.16$, become composites of cubic structured Cu1.8Se and hexagonal structured $Cu_{2.001}S$ when $0.2 \leq x \leq 0.7$, and finally have the same crystal structure as orthorhombic structured Cu_2S when $0.8 \leq x \leq 1.0$. The overall thermoelectric performance of the $Cu_{1.98}S_xSe_{1-x}$ compounds is mainly correlated with the electron effective mass and the density of states, with the zT values first increasing and then decreasing. Additionally, all the samples show stable thermoelectric compatibility factors over a broad temperature range from 700 to 1000 K, which could greatly benefit their practical applications.

References

[1] W. G. Zeier, Y. Pei, G. Pomrehn, T. Day, N. Heinz, C. P. Heinrich, G. J. Snyder, W. Tremel, Phonon scattering through a local anisotropic structural disorder in the thermoelectric solid solution $Cu_2Zn_{1-x}Fe_xGeSe_4$, J. Am. Chem. Soc. 2013, 135, 726.

[2] W. Liu, X. Yan, G. Chen, Z. Ren, Recent advances in thermoelectric nanocomposites, Nano Energy 2012, 1, 42.

[3] P. Jood, R. J. Mehta, Y. Zhang, G. Peleckis, X. Wang, R. W. Siegel, T. Borca-Tasciuc, S. X. Dou, G. Ramanath, Al-doped zinc oxide nanocomposites with enhanced thermoelectric properties, Nano Lett. 2011, 11, 4337.

[4] Y. Zhang, X. L. Wang, W. K. Yeoh, R. K. Zheng, C. Zhang, Electrical and thermoelectric properties of single-wall carbon nanotube doped Bi_2Te_3, Appl. Phys. Lett. 2012, 101, 031909.

[5] Y. Pei, X. Shi, A. LaLonde, H. Wang, L. Chen, G. J. Snyder, Convergence of electronic bands for high performance bulk thermoelectrics, Nature 2011, 473, 66.

[6] Y. Pei, Z. M. Gibbs, A. Gloskovskii, B. Balke, W. G. Zeier, G. J. Snyder, Optimum Carrier Concentration in n-Type PbTe Thermoelectrics, Adv. Energy Mater. 2014, 4, 1400486.

[7] S. A. Yamini, H. Wang, Z. M. Gibbs, Y. Pei, S. X. Dou, G. J. Snyder, Chemical composition tuning in quaternary p-type Pb-chalcogenides--a promising strategy for enhanced thermoelectric performance, Phys. Chem. Chem. Phys. 2014, 16, 1835.

[8] Y. Pei, N. A. Heinz, G. J. Snyder, Alloying to increase the band gap for improving thermoelectric properties of Ag_2Te, J. Mater. Chem. 2011, 21, 18256.

[9] H. Wang, Y. Pei, A. D. LaLonde, G. J. Snyder, Heavily doped p-type PbSe with high thermoelectric performance: an alternative for PbTe, Adv. Mater. 2011, 23, 1366.

[10] M. Cutler, J. Leavy, R. Fitzpatrick, Electronic transport in semimetallic cerium sulfide, Phys. Rev. 1964, 133, A1143.

[11] A. Bulusu, D. G. Walker, Review of electronic transport models for thermoelectric materials, Superlattice Microst. 2008, 44, 1.

[12] G. J. Snyder, Toberer, E. S. , Complex thermoelectric materials, Nat. Mater. 2008, 7, 10.

[13] D. K. Misra, A. Rajput, A. Bhardwaj, N. S. Chauhan, S. Singh, Enhanced power factor and reduced thermal conductivity of a half-Heusler derivative $Ti_9Ni_7Sn_8$: A bulk nanocomposite thermoelectric material, Appl. Phys. Lett. 2015, 106, 103901.

[14] B. Lange, C. Freysoldt, J. Neugebauer, Native and hydrogen-containing point defects in Mg_3N_2: A density functional theory study, Phys. Rev. B 2010, 81, 224109.

[15] G. Dennler, R. Chmielowski, S. Jacob, F. Capet, P. Roussel, S. Zastrow, K. Nielsch, I. Opahle, G. K. H. Madsen, Are Binary Copper Sulfides/Selenides Really New and Promising Thermoelectric Materials?, Adv. Energy Mater. 2014, 4, 1301581.

[16] H. Liu, X. Shi, F. Xu, L. Zhang, W. Zhang, L. Chen, Q. Li, C. Uher, T. Day, G. J. Snyder, Copper ion liquid-like thermoelectrics, Nat. Mater. 2012, 11, 422.

[17] Y. He, T. Day, T. Zhang, H. Liu, X. Shi, L. Chen, G. J. Snyder, High thermoelectric performance in non-toxic earth-abundant copper sulfide, Adv. Mater. 2014, 26, 3974.

[18] L. Zhao, X. Wang, J. Wang, Z. Cheng, S. Dou, J. Wang, L. Liu, Superior intrinsic thermoelectric performance with zT of 1.8 in single-crystal and melt-quenched highly dense $Cu_{2-x}Se$ bulks, Sci. Rep. 2015, 5, 7671.

[19] L. Zhao, X. Wang, F. Y. Fei, J. Wang, Z. Cheng, S. Dou, J. Wang, G. J. Snyder, High thermoelectric and mechanical performance in highly dense $Cu_{2-x}S$ bulks prepared by a melt-solidification technique, J. Mater. Chem. A 2015, 3, 9432.

[20] L. Zhao, X. Wang, F. F. Yun, J. Wang, Z. Cheng, S. Dou, J. Wang, G. J. Snyder, The Effects of Te^{2-} and I^- Substitutions on the Electronic Structures, Thermoelectric Performance, and Hardness in Melt-Quenched Highly Dense $Cu_{2-x}Se$, Advanced Electronic Materials 2015, 1, 1400015.

[21] M. Rasander, L. Bergqvist, A. Delin, Density functional theory study of the electronic structure of fluorite Cu_2Se, J. Phys. Condens. Matter. 2013, 25, 125503.

[22] S. Ballikaya, H. Chi, J. R. Salvador, C. Uher, Thermoelectric properties of Ag-doped Cu_2Se and Cu_2Te, J. Mater. Chem. A 2013, 1, 12478.

[23] M. Ibáñez, D. Cadavid, U. Anselmi-Tamburini, R. Zamani, S. Gorsse, W. Li, A. M. López, J. R. Morante, J. Arbiol, A. Cabot, Colloidal synthesis and thermoelectric properties of Cu_2SnSe_3 nanocrystals, Journal of Materials Chemistry A 2013, 1, 1421.

[24] A. Suzumura, M. Watanabe, N. Nagasako, R. Asahi, Improvement in Thermoelectric Properties of Se-Free Cu_3SbS_4 Compound, J Electron Mater 2014, 43, 2356.

[25] B. Zhong, Y. Zhang, W. Li, Z. Chen, J. Cui, W. Li, Y. Xie, Q. Hao, Q. He, High superionic conduction arising from aligned large lamellae and large figure of merit in bulk $Cu_{1.94}Al_{0.02}Se$, Appl. Phys. Lett. 2014, 105, 123902.

[26] J. Fan, W. Carrillo-Cabrera, I. Antonyshyn, Y. Prots, I. Veremchuk, W. Schnelle, C. Drathen, L. Chen, Y. Grin, Crystal Structure and Physical Properties of Ternary Phases around the Composition $Cu_5Sn_2Se_7$ with Tetrahedral Coordination of Atoms, Chem Mater 2014, 26, 5244.

[27] K. Tyagi, B. Gahtori, S. Bathula, V. Toutam, S. Sharma, N. K. Singh, A. Dhar, Thermoelectric and mechanical properties of spark plasma sintered Cu_3SbSe_3 and Cu_3SbSe_4: Promising thermoelectric materials, Appl. Phys. Lett. 2014, 105, 261902.

[28] H. Liu, X. Yuan, P. Lu, X. Shi, F. Xu, Y. He, Y. Tang, S. Bai, W. Zhang, L. Chen, Y. Lin, L. Shi, H. Lin, X. Gao, X. Zhang, H. Chi, C. Uher, Ultrahigh thermoelectric performance by electron and phonon critical scattering in $Cu_2Se_{1-x}I_x$, Adv. Mater. 2013, 25, 6607.

[29] G. J. Snyder, Application of the compatibility factor to the design of segmented and cascaded thermoelectric generators, Appl. Phys. Lett. 2004, 84, 2436.

[30] G. Snyder, T. Ursell, Thermoelectric efficiency and compatibility, Phys. Rev. Lett. 2003, 91, 148301.

[31] G. J. Snyder, T. Caillat, Using the compatibility factor to design high efficiency segmented thermoelectric generators, MRS Proceedings 2003, 793, 37.

[32] A. Bhardwaj, N. S. Chauhan, D. K. Misra, Significantly enhanced thermoelectric figure of merit of p-type Mg_3Sb_2-based Zintl phase compound via

nanostructuring employing high energy mechanical milling coupled with spark plasma sintering, J. Mater. Chem. A 2015, 3, 10777.

[33] S. J. Clark, M. D. Segall, C. J. Pickard, P. J. Hasnip, M. I. J. Probert, K. Refson, M. C. Payne, First principles methods using CASTEP, Z. Kristallogr. 2005, 220, 567.

[34] P. Hohenberg, Inhomogeneous electron gas, Phys. Rev. 1964, 136, B864.

[35] J. P. Perdew, K. Burke, M. Ernzerhof, Generalized Gradient Approximation Made Simple, Phys. Rev. Lett. 1996, 77, 3865.

[36] M. Oliveria, R. K. McMullan, B. J. Wuensch, Single crystal neutron diffraction analysis of the cation distribution in the high-temerpature phases a-Cu2-xS, a-Cu2-xSe, AND a-Ag2Se, Solid State Ion. 1988, 28-30, 1332.

[37] R. D. Heyding, R. M. Murry, The crystal structures of $Cu_{1.8}Se$, Cu_3Se_2, a- and g-CuSe, $CuSe_2$ and $CuSe_2$ II, Can. J. Chem. 1976, 54, 841.

[38] P. Lu, H. Liu, X. Yuan, F. Xu, X. Shi, K. Zhao, W. Qiu, W. Zhang, L. Chen, Multiformity and fluctuation of Cu ordering in Cu2Se thermoelectric materials, J. mater. Chem. A 2015, 3, 6901.

[39] L. Gulay, M. Daszkiewicz, O. Strok, A. Pietraszko, Crystal structure of Cu_2Se, Chem. Met. Alloys 2011, 4, 200.

[40] T. S. Ursell, G. J. Snyder, Compatibility of Segmented Thermoelectric Generators, Twenty-First International Conference on Thermoelectrics 2002, 412.

CHAPTER 6

6 STRUCTURAL, THERMOELECTRIC AND MECHENICAL PROPERTIES FOR THE TE-DOPED AND I-DOEPD $CU_{2-X}SE$ BULKS

6.1 Preface

Thermoelectric technology can convert thermal energy into electrical energy directly,[1-4] with such virtues as high reliability, quiet operation, and no pollution.[5-8] It is well known that the energy conversion efficiency of thermoelectric materials at a temperature T can be estimated by a dimensionless thermoelectric figure-of-merit, zT.[9-13] Furthermore, κ can be expressed as $\kappa = \kappa_L + \kappa_c$, where κ_L and κ_c are the lattice thermal conductivity and the charge carrier thermal conductivity, respectively. At high temperatures, lattice vibrations make the predominant contribution to the total thermal conductivity, as compared to the charge carriers.

Among all the high temperature thermoelectric materials developed so far, the copper-ion-liquid-like behaviour of $Cu_{2-x}Se$ should make it one of the most promising materials for potential applications and large scale utilization. It has been reported that polycrystalline $Cu_{2-x}Se$ bulks made by the conventional hot pressing method using a Spark Plasma Sintering (SPS) system have reached a high zT of ~ 1.5-1.6 at 1000 K.[14, 15]

It is well known that improved thermoelectric performance with higher zT values can be achieved by lowering κ, while not degrading S and σ. Generally, κ can be reduced effectively by the confinement of phonon vibrations through substitution or doping using heavier atoms. Heavier atoms belonging to the same family can effectively

reduce thermal conductivity and have little effect on electrical conductivity because they have the same chemical valence. Fortunately, the thermoelectric performance of several kinds of materials has been successfully enhanced to a large extent, with zT over 1.0 achieved through this approach.[16-18] Therefore, it might be possible to further improve the thermoelectric performance of the $Cu_{2-x}Se$ system via the doping approach on Se sites.

In order to gain further insight into the maximum level of this system's thermoelectric performance, we chose tellurium and iodine for substitution onto Se sites, based on the following considerations: 1) Te^{2-} has the same valence as Se^{2-} and is heavier than Se^{2-}. Therefore, it should have little effect on the carrier concentration and could effectively reduce lattice thermal conductivity. 2) I^- is also much heavier than Se^{2-}, and it should lead to a reduction of thermal conductivity as well, although its valence is 1^-, instead of 2^-. It should be pointed out that I-doped $Cu_{2-x}Se$ bulk has been reported to achieve enhanced zT values at the phase transition temperature of around 400 K.[19, 20] There are, however, no reports on its high temperature thermoelectric performance at T > 500 K up to now. Therefore, it is just as desirable to investigate the I-doping effects on the thermoelectric performance of $Cu_{2-x}Se$.

Furthermore, it is also important to understand why $Cu_{2-x}Se$ is an intrinsic p-type conductor, as well as how the dopant elements affect the parent compound's electrical conductivity from the fundamental point of view. There is a lack of information on the electronic density of states of the doped $Cu_{2-x}Se$ system so far. Therefore, density functional theory (DFT) calculations are very necessary for the $Cu_{2-x}Se$ system, which can also provide theoretical backup for further improving its thermoelectric performance using different dopants.

It should be noted that good mechanical performance is quite essential for the practical applications of thermoelectric materials, because they are likely to sustain some strong mechanical and thermal stresses caused by the pressure needed to make good contact between the thermoelectric modules and the heat source, as well as the temperature gradient inside the thermoelectric modules. It has been reported that the correlation between electronic and mechanical properties can be related to the elastic interaction between dislocations and impurities, which will confine the motion of dislocations, and then, in turn, lead to enhanced hardness values.[21, 22] Therefore, it is also interesting to investigate the effects of Te- and I-doping on the mechanical properties of $Cu_{2-x}Se$.

In this work, we report our systematic study on the effects of Te^{2-} or I^- doping on the electronic density of states, crystal structures, thermoelectric performance, and hardness in the $Cu_{2-x}Se$ system. Our results show that stoichiometric Cu_2Se is a zero-gap material that becomes *p*-type for copper deficiency. Both calculations and experimental observations reveal that Te-doping increases electrical conductivity, while I-doping reduces it. I-doping was also found to enhance the Seebeck coefficient and reduce the charge carrier thermal conductivity. All our samples are *p*-type and show zT values over or close to 1.0 at T = 973 K, except for $Cu_{2-x}Te_{0.16}Se_{0.84}$. A maximum hardness of ~ 0.66 GPa is achieved for $Cu_{2-x}Te_{0.16}Se_{0.84}$, which is higher than those of polycrystalline Bi_2Te_3 and PbTe bulks.

6.2 Experimental

6.2.1 Sample fabrications

Firstly, polycrystalline un-doped, Te-doped, and I-doped $Cu_{2-x}Se$ pellets were synthesized by a conventional solid-state method. A mixture of Cu, Se, and Te powders in the molar ratio 2-x : y : 1-y (x = 0.02, y = 0.02, 0.08, 0.16), or Cu, Se, and I powders in the molar ratio 2-x : y : 1-y (x = 0.02, y = 0.04, 0.08) was pressed into pellets and sealed in evacuated quartz tubes, before being heated to 873 K for 1-5 hours with a heating rate of 5 K/min, followed by a furnace cooling to room temperature. Secondly, the as-sintered pellets were used in the melt-quenching approach. After they were melted completely on an acetylene and oxygen flame, they were quickly quenched in water to obtain highly dense bulks.

Finally, the obtained bulks were shaped into disks with dimensions of Φ10 mm × 1 mm for thermal diffusivity measurements. After the measurements, the same sample disks were cut into rectangular bars for the electrical conductivity and Seebeck coefficient measurements.

6.2.2 Measurements

XRD patterns and FE-SEM cross-sectional images were collected with a GBC MMA system using Cu-Kα radiation and a JEOL JSM-7500FA system, respectively. The electrical conductivity and Seebeck coefficient were measured simultaneously in a helium atmosphere in the temperature range from room temperature to 973 K using an RZ2001i system. The thermal diffusivity (D) was measured by the laser flash method (LINSEIS LFA 1000), and the specific heat (C_p) was determined by differential scanning calorimetry (TA Q100). The sample density (dd) was determined by the

Archimedes method. The thermal conductivity (κ) was calculated by $\kappa = D \times C_p \times dd$. The Vickers hardness of the ultra-fast formed samples was measured at different locations, with the Duramin 70 Vickers hardness tester applying a load of 0.1 N.

6.2.3 Calculation details

First principles calculations were carried out using density functional theory (DFT) implemented by the Cambridge Serial Total Energy Package (CASTEP)[23] The generalized gradient approximation (GGA)[24] was used in our calculations, with parameterization by the Perdew-Burke-Ernzerhof (PBE)[25] and ultra-soft pseudo-potentials. The plane wave cut-off energy was set at 400 eV. Total and partial density of states of Te-doped, I-doped, and un-doped copper deficient $Cu_{1.875}Se$ was calculated on 2×2×2 supercells of the primitive cell. A 4×4×4 Monkhorst-Pack k–point mesh, [26] with the Brillouin zone path of ΓXWLΓK, of a primitive cell was employed to calculate the band structure of Cu_2Se.

6.3 Results and discussion

6.3.1 DFT calculations

Before carrying out experiments, let us first investigate by DFT calculations how the Te^{2-} and I^- substitutions on Se^{2-} sites can affect the system's electronic density of states, which, in turn, affects its electrical conductivity and Seebeck coefficient. It is well known that high temperature β-phase $Cu_{2-x}Se$ is crystallized as a cubic structure with space group $Fm\bar{3}m$. Figure 6-1 shows the idealized version of the unit cell and primitive cell for high temperature β-phase Cu_2Se[27] . It indicates that the Se atoms form

a rigid face-centred cubic (*fcc*) sub-lattice, while the Cu atoms occupy the tetrahedral interstitial positions in the ideal unit cell.

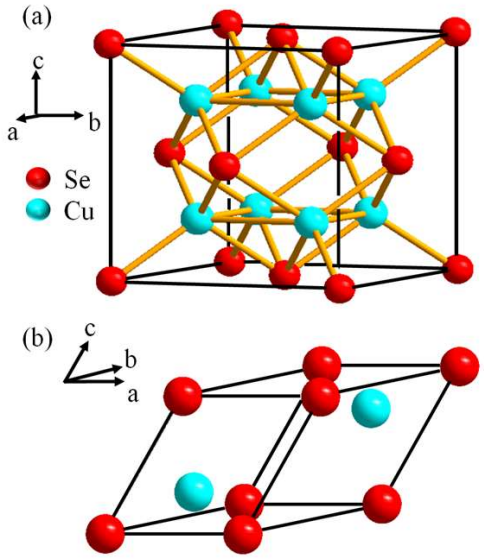

Figure 6-1 The ideal version of unit cell (a) and primitive cell (b) for the high temperature β-phase Cu_2Se.

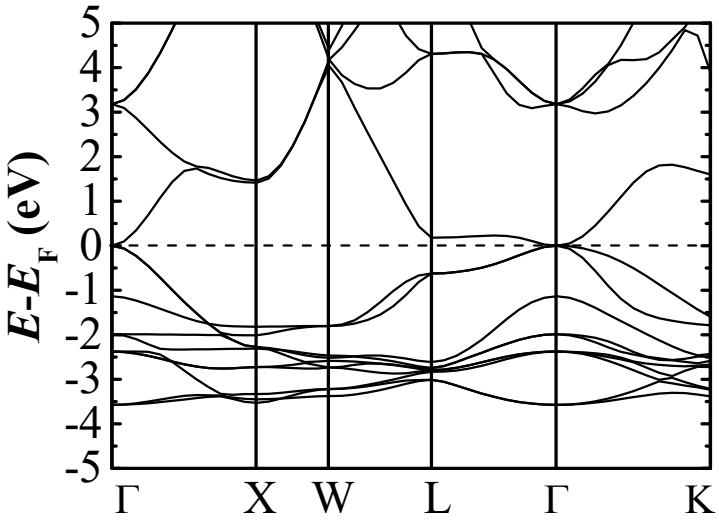

Figure 6-2 Calculated electronic band structures for the stoichiometric Cu_2Se based density functional theory method.

Figure 6-2 shows the calculated electronic band structures for the stoichiometric Cu_2Se density functional theory (DFT) method. It indicates that the stoichiometric Cu_2Se is a zero-gap material,[28, 29] which is in good agreement with what has been reported by M. Råsander et al.

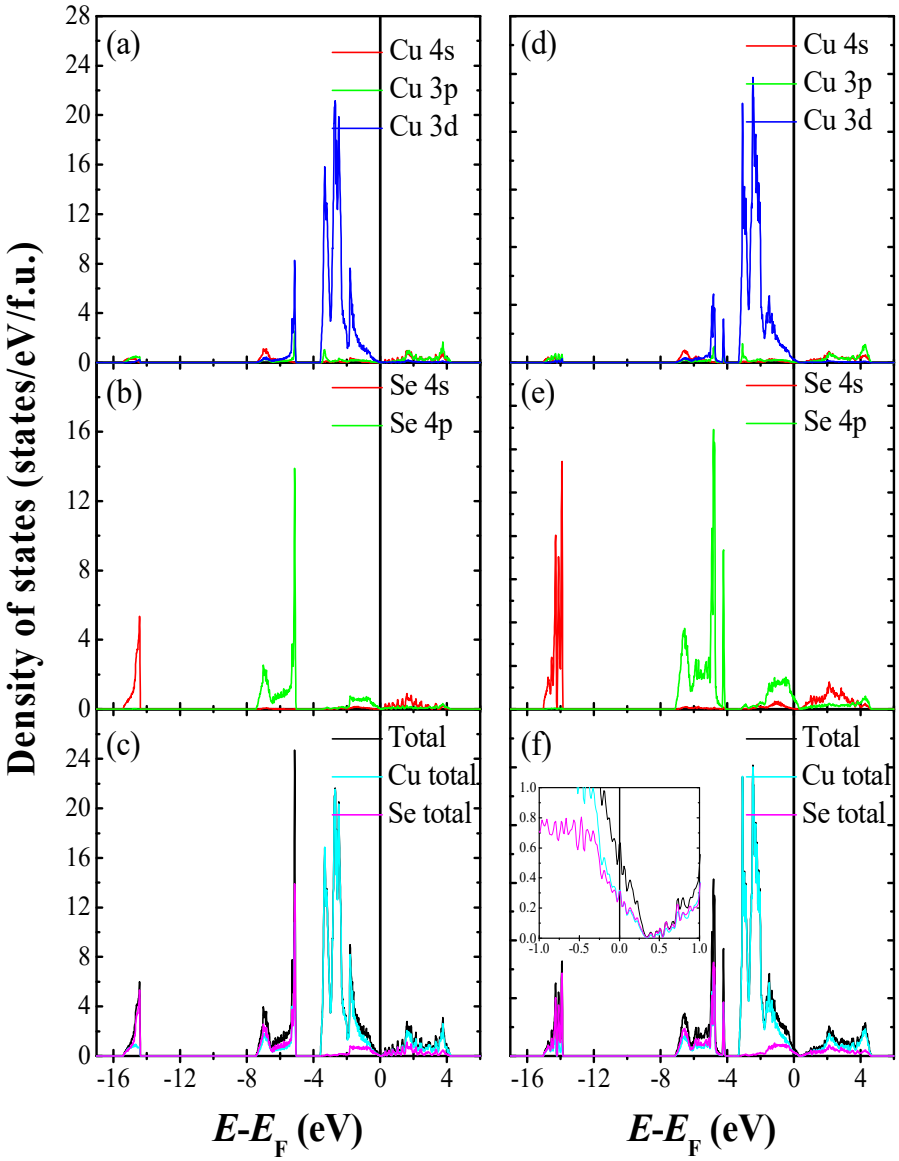

Figure 6-3 Calculated total and partial electronic density of states for stoichiometric Cu_2Se (left) and copper deficient $Cu_{15}Se_8$ (right). The inset displayed in (f) shows the enlarged total density of states near the Fermi level of $Cu_{15}Se_8$.

Figure 6-3 shows the calculated total and partial density of states (DOS) for stoichiometric Cu_2Se, and copper deficient $Cu_{15}Se_8$ using the DFT method. The inset displayed in Figure 6-3(f) shows the enlarged total density of states near the Fermi level of $Cu_{15}Se_8$. The results indicate that the Cu 3d states make the dominant contribution to the total DOS from -4eV to the Fermi level (E_F). The total DOS in the conduction bands is mainly built up by Cu 3p-states and Se 4s-states. The 4p- and 4s-states of Se are responsible for the peaks around -6 eV and -15 eV, respectively. For copper deficient $Cu_{15}Se_8$, the Cu 3p-, 3d-, and Cu-4s states, and the Se 4s-, and 4p-states all move above E_F compared to those of Cu_2Se, making the $Cu_{15}Se_8$ an intrinsic *p*-type conductor.

Figure 6-4 (a-h) shows the calculated total and partial electronic density of states for the Te-doped $Cu_{15}Se_7Te_1$ (left) and I-doped $Cu_{15}Se_7I_1$ (right). The insets in Figure 6-4 (d) and Figure 6-4 (h) show the enlarged total DOS of $Cu_{15}Se_7Te_1$ and $Cu_{15}Se_7I_1$, respectively. The results reveal that both the $Cu_{15}Se_7Te_1$ and $Cu_{15}Se_7I_1$ compounds are *p*-type conductors. Furthermore, compared to the un-doped $Cu_{15}Se_8$, the Te^{2-} substitution causes an increase in the total DOS due to the contribution of its 5*p*-electrons at E_F. This can be ascribed to the enhancement of the partial DOS of both Se and Cu, which was displayed in the insets of Figure 6-4 (d).

The I^- substitution, however, gives rise to the reduction of the total and prtial DOS for both Se and Cu in the $Cu_{15}Se_7I_1$ compound. This should be related to the localization of the I^- 5*p* electrons as shown in the inset in Figure 6-4 (h).

It is well known that electrical conductivity (σ) and Seebeck coefficient (*S*) can be estimated by the following formula:

$$\sigma = ne\mu \qquad (6\text{-}1)^{[30]}$$

$$S = \frac{8\pi^2 k_B^2}{3e^{\ 2}} m^* T \left(\frac{\pi}{3n}\right)^{2/3} \qquad (6\text{-}2)^{[3, 31]}$$

where n, μ, k_B, and m^* are the charge carrier density, carrier mobility, Boltzmann constant, and effective mass of the carrier, respectively. Therefore, we can expect that the Te-doped and I doped $Cu_{2-x}Se$ should have higher and lower electrical conductivity than the corresponding un-doped $Cu_{2-x}Se$, respectively. Additionally, the Seebeck coefficient for I-doped $Cu_{2-x}Se$ samples should be the highest ones.

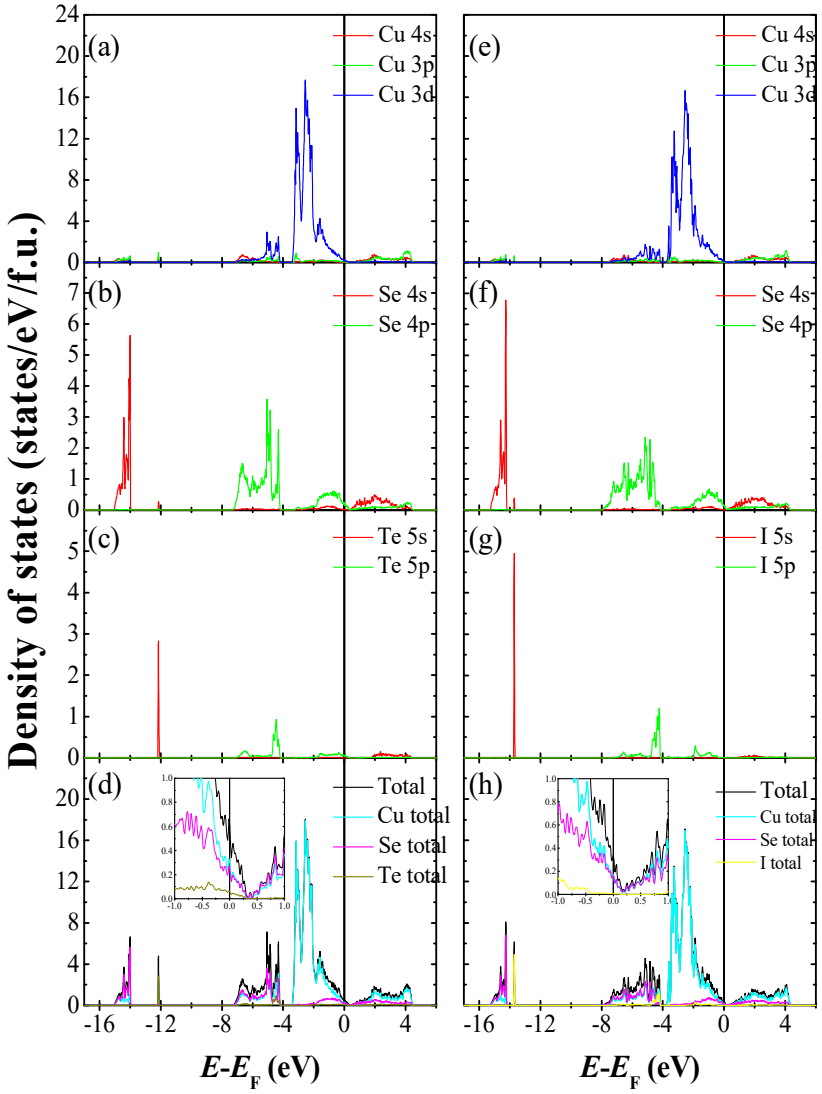

Figure 6-4 Calculated total and partial electronic density of states for the Te-doped $Cu_{15}Se_7Te_1$ (left) and I-doped $Cu_{15}Se_7I_1$ (right). The insets in (d) and (h) show the enlarged total density of states of $Cu_{15}Se_7Te_1$ and $Cu_{15}Se_7I_1$, respectively.

6.3.2 Structural properties

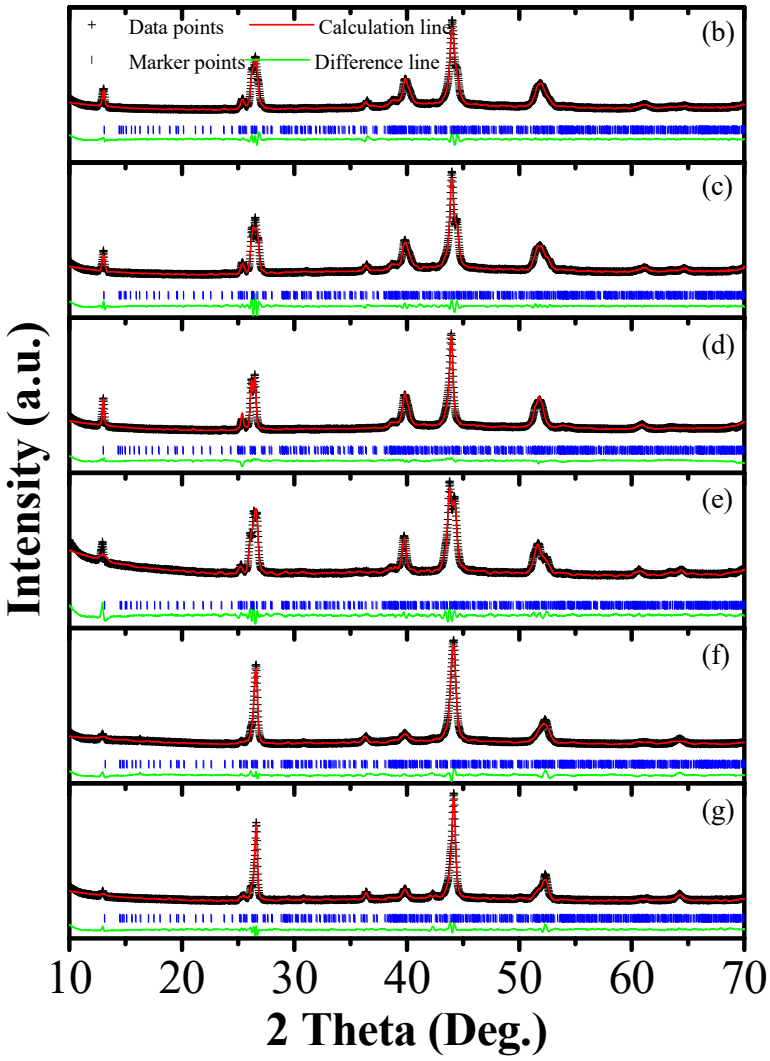

Figure 6-5 X-ray diffraction patterns of standard low temperature α-phase $Cu_{2-x}Se$, and refined XRD patterns for all the un-doped, Te-doped and I-doped $Cu_{2-x}Se$ bulks fabricated by the melt-quenching method: (a) standard low temperature α-phase $Cu_{2-x}Se$ (PDF No. 27-1131), (b) $Cu_{2-x}Se$, (c) $Cu_{2-x}Te_{0.02}Se_{0.98}$, (d) $Cu_{2-x}Te_{0.08}Se_{0.92}$, (e) $Cu_{2-x}Te_{0.16}Se_{0.84}$, (f) $Cu_{2-x}I_{0.04}Se_{0.96}$, and (g) $Cu_{2-x}Te_{0.08}Se_{0.92}$.

Figure 6-5 displays the X-ray diffraction (XRD) patterns of standard low temperature α-phase $Cu_{2-x}Se$ and refined XRD patterns for all the un-doped, Te-doped, and I-doped $Cu_{2-x}Se$ bulks fabricated by the ultra-fast melt-quenching method. The

atomic positions, lattice parameters, and R-factors for all samples deduced from the Rietveld refinement of the XRD patterns are listed in Table 6-1, Table 6-2 and Table 6-3, respectively. All the results indicate that all the Te-doped and I-doped samples are single phase and have the same monoclinic crystal structure as low temperature α-phase $Cu_{2-x}Se$ (PDF No.: 27-1131), with some differences in lattice parameters and atomic positions. Table 6-3 shows the Rietveld refinement results, indicating that all the Te-doped and I-doped samples have much larger unit cell volumes compared to the un-doped sample. These results imply that that Te^{2-} and I^- have successfully substituted onto Se^{2-} sites in the $Cu_{2-x}Se$ lattice.

Table 6-1 Atomic positions for the as-prepared un-doped and I-doped $Cu_{2-x}Se$ samples deduced from Rietveld refinements of XRD patterns

Atom	$Cu_{2-x}Se$			$Cu_{2-x}I_{0.04}Se_{0.96}$			$Cu_{2-x}I_{0.08}Se_{0.92}$		
	x/a	*y/b*	*z/c*	*x/a*	*y/b*	*z/c*	*x/a*	*y/b*	*z/c*
Cu1	0.3817(1)	0.0806(1)	0.3208(6)	0.3653(5)	0.0414(4)	0.2863(9)	0.3315(7)	0.0713(2)	0.3155(0)
Cu2	0.8910(1)	0.9160(0)	0.4405(1)	0.8902(6)	0.9224(3)	0.4375(0)	0.8921(0)	0.9182(4)	0.4420(5)
Cu3	0.8552(8)	0.2484(6)	0.3231(6)	0.9416(4)	0.2244(6)	0.3202(1)	0.8168(8)	0.2388(3)	0.3168(1)
Cu4	0.4343(0)	0.0708(9)	0.4510(8)	0.4064(9)	0.0858(3)	0.4601(5)	0.4090(0)	0.0676(6)	0.4595(1)
Cu5	0.1915(7)	0.1844(8)	0.3888(5)	0.2322(8)	0.2576(3)	0.3373(8)	0.2270(6)	0.2173(1)	0.3917(1)
Cu6	0.8995(0)	0.2488(2)	0.4353(7)	0.7967(3)	0.2843(3)	0.5169(0)	0.8970(4)	0.2645(2)	0.4515(7)
Cu7	0.6401(8)	0.9003(2)	0.3658(9)	0.6017(4)	0.8750(3)	0.3346(1)	0.6241(4)	0.9111(8)	0.3506(5)
Cu8	0.8215(6)	0.8998(6)	0.2931(9)	0.8508(3)	0.9101(0)	0.2897(6)	0.8560(0)	0.9164(6)	0.2890(8)
Cu9	0.4958(5)	0.2639(5)	0.3488(2)	0.5121(7)	0.2633(0)	0.3838(7)	0.5175(6)	0.2551(0)	0.3611(0)
Cu10	0.6836(2)	0.0858(8)	0.3915(5)	0.6656(5)	0.0716(6)	0.3946(6)	0.6718(7)	0.0809(6)	0.3972(5)
Cu11	0.9684(8)	0.0201(5)	0.3490(5)	0.9757(4)	0.0639(7)	0.3542(5)	0.9304(3)	0.0556(9)	0.3540(0)
Cu12	0.2703(5)	0.9276(9)	0.3977(7)	0.2407(2)	0.9280(2)	0.4041(2)	0.2402(9)	0.9255(0)	0.4024(7)
Se1	0.0677(9)	0.0700(6)	0.4470(3)	0.0532(7)	0.0707(9)	0.4448(0)	0.0604(2)	0.0874(8)	0.4346(5)
Se2	0.6782(6)	0.0867(6)	0.2995(7)	0.7039(4)	0.0762(1)	0.3074(3)	0.6845(1)	0.0783(7)	0.2988(9)
Se3	0.2013(4)	0.2442(1)	0.3140(3)	0.1793(6)	0.2157(0)	0.3148(2)	0.1776(5)	0.2301(1)	0.3030(5)
Se4	0.0720(9)	0.7441(4)	0.4425(1)	0.0780(4)	0.7560(3)	0.4489(5)	0.0889(3)	0.7526(7)	0.4470(5)
Se5	0.5669(2)	0.9032(1)	0.4389(3)	0.5714(5)	0.9040(4)	0.4426(6)	0.5660(5)	0.9086(6)	0.4371(1)
Se6	0.1927(0)	0.9177(8)	0.3103(2)	0.1633(8)	0.8951(2)	0.3194(1)	0.1886(3)	0.9024(4)	0.3039(8)
I	-	-	-	0.1885(4)	0.9051(7)	0.3064(9)	0.1977(3)	0.8943(8)	0.3154(5)

Table 6-2 Atomic positions for the as-prepared Te-doped $Cu_{2-x}Se$ samples deduced from Rietveld refinements of XRD patterns.

Atom	$Cu_{2-x}Te_{0.02}Se$			$Cu_{2-x}Te_{0.08}Se_{0.98}$			$Cu_{2-x}Te_{0.16}Se_{0.84}$		
	x/a	*y/b*	*z/c*	*x/a*	*y/b*	*z/c*	*x/a*	*y/b*	*z/c*
Cu1	0.4116(4)	0.0832(9)	0.3272(0)	0.4354(2)	0.0089(6)	0.3289(1)	0.3772(1)	0.0860(7)	0.3120(5)
Cu2	0.8912(2)	0.9145(8)	0.4293(3)	0.8820(2)	0.9192(1)	0.4441(1)	0.9357(9)	0.9164(6)	0.4363(7)
Cu3	0.8714(6)	0.2481(1)	0.3035(5)	0.8738(6)	0.2643(1)	0.2996(5)	0.9118(3)	0.2268(3)	0.3214(5)
Cu4	0.4283(5)	0.0747(7)	0.4454(4)	0.4275(8)	0.0513(6)	0.4370(8)	0.3725(5)	0.0685(4)	0.4474(2)
Cu5	0.2264(0)	0.2055(2)	0.3962(5)	0.2280(4)	0.2387(6)	0.4058(5)	0.2160(5)	0.2277(4)	0.3984(8)
Cu6	0.9075(9)	0.2423(0)	0.4389(5)	0.8887(8)	0.2423(5)	0.4319(3)	0.9407(4)	0.2353(7)	0.4502(3)
Cu7	0.6125(4)	0.9103(1)	0.3686(0)	0.6647(0)	0.9292(9)	0.2697(8)	0.6073(6)	0.8647(5)	0.3492(2)
Cu8	0.8702(6)	0.9091(9)	0.2877(9)	0.8621(4)	0.9061(1)	0.2982(1)	0.9036(6)	0.9006(7)	0.2855(7)
Cu9	0.5734(4)	0.3094(9)	0.3915(1)	0.4424(9)	0.2128(3)	0.3373(5)	0.5310(2)	0.2157(2)	0.3381(3)
Cu10	0.6609(8)	0.0921(1)	0.3930(8)	0.6606(8)	0.1160(3)	0.3947(6)	0.7011(1)	0.0746(2)	0.3944(2)
Cu11	0.9354(5)	0.0590(5)	0.3566(1)	0.9928(7)	0.0545(1)	0.3551(6)	0.9346(5)	0.0687(4)	0.3622(9)
Cu12	0.2634(3)	0.9343(7)	0.3971(3)	0.2384(1)	0.9036(4)	0.4039(3)	0.2749(3)	0.9172(1)	0.4025(8)
Se1	0.0569(5)	0.0758(7)	0.4456(7)	0.0545(3)	0.0833(6)	0.4437(7)	0.0835(0)	0.0625(2)	0.4404(0)
Se2	0.6930(0)	0.0876(5)	0.3063(0)	0.7002(3)	0.0876(0)	0.3074(8)	0.6930(8)	0.0714(4)	0.3039(0)
Se3	0.2062(4)	0.2166(8)	0.3068(5)	0.1834(6)	0.2481(1)	0.3133(7)	0.1770(3)	0.2408(1)	0.2969(8)
Se4	0.0814(7)	0.7500(1)	0.4444(6)	0.0793(9)	0.7403(1)	0.4461(1)	0.0730(3)	0.7354(7)	0.4504(6)
Se5	0.5724(9)	0.8987(5)	0.4479(9)	0.5723(7)	0.9132(3)	0.4416(1)	0.5615(3)	0.9063(4)	0.4356(4)
Se6	0.2214(9)	0.9078(7)	0.3134(5)	0.1804(8)	0.9183(3)	0.3051(5)	0.6526(5)	0.9031(0)	0.2869(5)
Te	0.1660(8)	0.9510(7)	0.3156(1)	0.1831(2)	0.9104(7)	0.3123(0)	0.1912(0)	0.9036(9)	0.3046(2)

Table 6-3 Lattice parameters and R-factors for the as-prepared Te-doped, and I-doped $Cu_{2-x}Se$ samples deduced from Rietveld refinements of XRD patterns.

Lattice parameter / Sample	*a* (Å)	*b* (Å)	*c* (Å)	*β*	*V* (Å^3)	*Rp*	*Rwp*
$Cu_{2-x}Se$	7.117(7)	12.358(6)	27.278(2)	94.112(6)	2392.0(1)	1.820	2.793
$Cu_{2-x}Te_{0.02}Se_{0.98}$	7.159(4)	12.249(1)	27.364(8)	94.556(2)	2392.2(1)	2.126	3.225
$Cu_{2-x}Te_{0.08}Se_{0.92}$	7.136(5)	12.361(6)	27.310(6)	94.572(7)	2401.6(3)	1.989	2.971
$Cu_{2-x}Te_{0.16}Se_{0.84}$	7.214(7)	12.345(2)	27.608(6)	94.789(3)	2450.4(3)	2.383	3.401
$Cu_{2-x}I_{0.04}Se_{0.96}$	7.115(1)	12.350(3)	27.306(5)	94.155(2)	2393.2(1)	2.668	3.606
$Cu_{2-x}I_{0.08}Se_{0.92}$	7.117(2)	12.368(1)	27.274(4)	94.033(4)	2394.9(2)	2.586	3.505

6.3.3 Thermoelectric properties

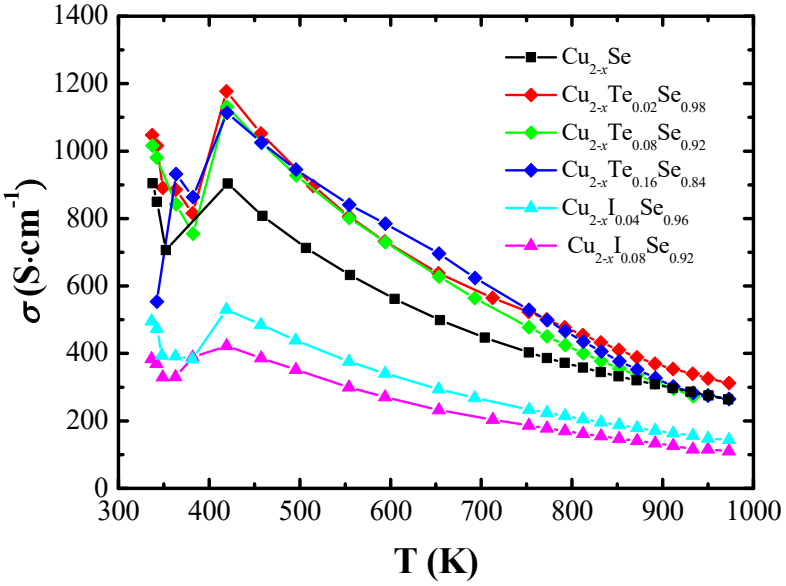

Figure 6-6 Temperature dependence of the electrical conductivity (σ) for the obtained highly dense un-doped, Te-doped, and I-doped $Cu_{2-x}Se$ bulks.

The temperature dependences of the electrical conductivity for the obtained highly dense un-doped, Te-doped, and I-doped $Cu_{2-x}Se$ bulks are displayed in Figure 6-6. As we predicted from first principles calculations, the Te-doped $Cu_{2-x}Se$ samples have higher electrical conductivity than the un-doped one over the wide temperature range from room temperature to 750 K. The highest value of ~ 1180 $S \cdot cm^{-1}$ for $Cu_{2-x}Te_{0.08}Se_{0.92}$ at 420 K is more than 30% larger than that of the un-doped $Cu_{2-x}Se$. When T goes over 750 K, the Te-doped $Cu_{2-x}Se$ samples have almost the same electrical conductivity as the un-doped sample, particularly the $Cu_{2-x}Te_{0.08}Se_{0.92}$ and $Cu_{2-x}Te_{0.16}Se_{0.84}$.

The electrical conductivity of the I-doped $Cu_{2-x}Se$ samples is lower than that of the un-doped sample for both the low temperature α-phase and the high temperature β-phase, and this trend becomes more obvious as the I-doping level increases. For the $Cu_{2-x}I_{0.08}Se_{0.92}$, the electrical conductivity is about 110 $S \cdot cm^{-1}$ at ~ 970 K, which is about 50% lower than that of the un-doped bulk. The above experimental observations are consistent with our first-principles calculation results.

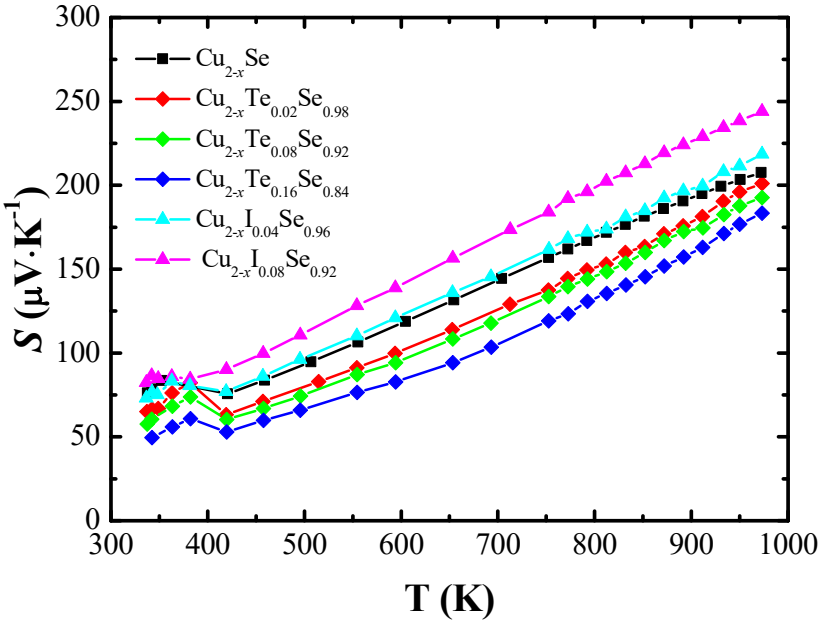

Figure 6-7 Temperature dependence of the Seebeck coefficient for the obtained highly dense un-doped, Te-doped, and I-doped $Cu_{2-x}Se$ bulks.

Figure 6-7 shows the temperature dependence of the Seebeck coefficient for the obtained un-doped, Te-doped, and I-doped $Cu_{2-x}Se$ bulks. All the I-doped $Cu_{2-x}Se$ samples have higher S values than the un-doped sample. For the $Cu_{2-x}I_{0.08}Se_{0.92}$, the highest S is 245 $\mu V \cdot K^{-1}$ at T around 970 K, which is ~ 20% larger than that of the un-doped sample. All the Te-doped samples have a lower Seebeck coefficient compared to the un-doped one, however, and it decreases slightly as the Te-doping level increases.

The ability of a material to produce useful electrical power under a given temperature difference can be estimated by the power factor (PF), where PF = σS^2, and σ and S are the electrical conductivity and Seebeck coefficient, respectively.

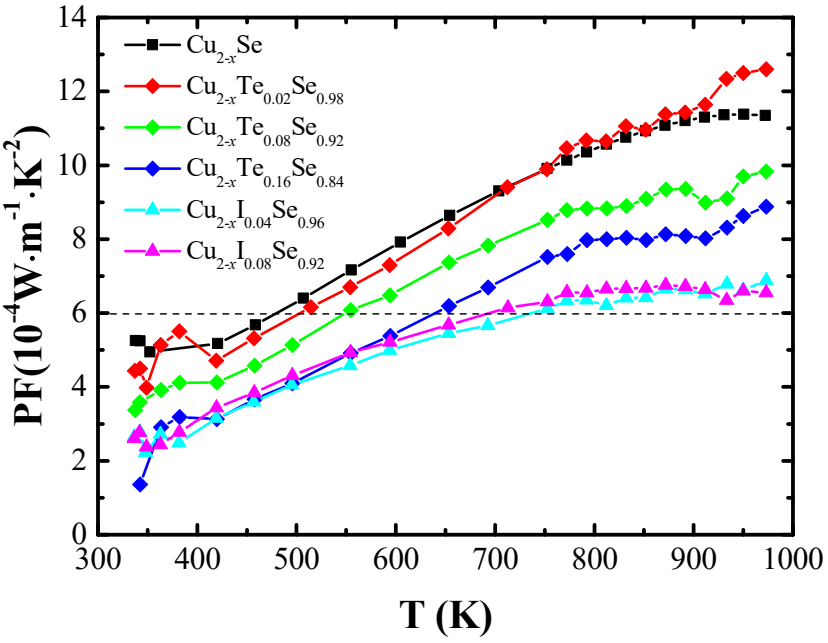

Figure 6-8 Temperature dependence of the power factor (PF) for the obtained highly dense un-doped, Te-doped, and I-doped $Cu_{2-x}Se$ bulks.

Figure 6-8 shows the temperature dependence of the power factor for the un-doped, Te-doped, and I-doped $Cu_{2-x}Se$ samples fabricated by the ultra-fast melt-quenching method. It indicates that all the samples have a PF value over 6×10^{-4} $W \cdot m^{-1} \cdot K^{-2}$ when the temperature goes over 700 K. All the Te-doped samples show the same trend in the power factor with increasing temperature, with the highest value of 12.5×10^{-4} $W \cdot m^{-1} \cdot K^{-2}$ at 973 K for the $Cu_{2-x}Te_{0.02}Se_{0.98}$ sample. Additionally, all the I-doped samples have PF values between 2.5×10^{-4} and 7.0×10^{-4} $W \cdot m^{-1} \cdot K^{-2}$ in the temperature range from room temperature to 973 K.

Figure 6-9 Figure 6-9shows the temperature dependence of the thermal transport properties: the specific heat (C_p) for the fabricated un-doped, Te-doped, and I-doped $Cu_{2-x}Se$ samples. Judging from the C_p versus T curves, all the samples exhibit a phase transition at a critical temperature T_c = 350 - 400 K, and the T_c values of all the Te-doped, and I-doped $Cu_{2-x}Se$ samples are smaller compared to the un-doped sample.

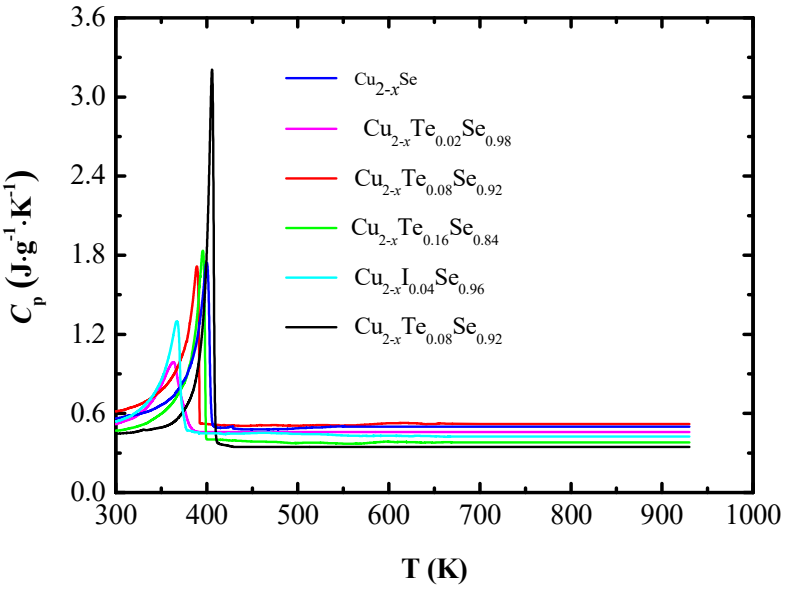

Figure 6-9 Temperature dependence of the specific heat (C_p) for the fabricated un-doped, Te-doped, and I-doped $Cu_{2-x}Se$ bulks.

Figure 6-10 shows the temperature dependence of the thermal transport properties: the total thermal conductivity (κ), and the calculated lattice thermal conductivity (κ_L) and charge carrier thermal conductivity (κ_c) for the fabricated un-doped, Te-doped, and I-doped $Cu_{2-x}Se$ samples. In contrast to other types of thermoelectric materials, the doping approach using heavier atoms, such as Te and I, seems not to be effective for reducing the thermal conductivity of the $Cu_{2-x}Se$ system. Rather, all the Te-doped Cu_{2-}

$_x$Se samples have higher κ values than the un-doped sample, while all the I-doped samples have almost the same κ values as the un-doped $Cu_{2-x}Se$. This should be attributed to the fact that it is the liquid-like behaviour of the copper ions that determines the thermal conductivity of the $Cu_{2-x}Se$ system.

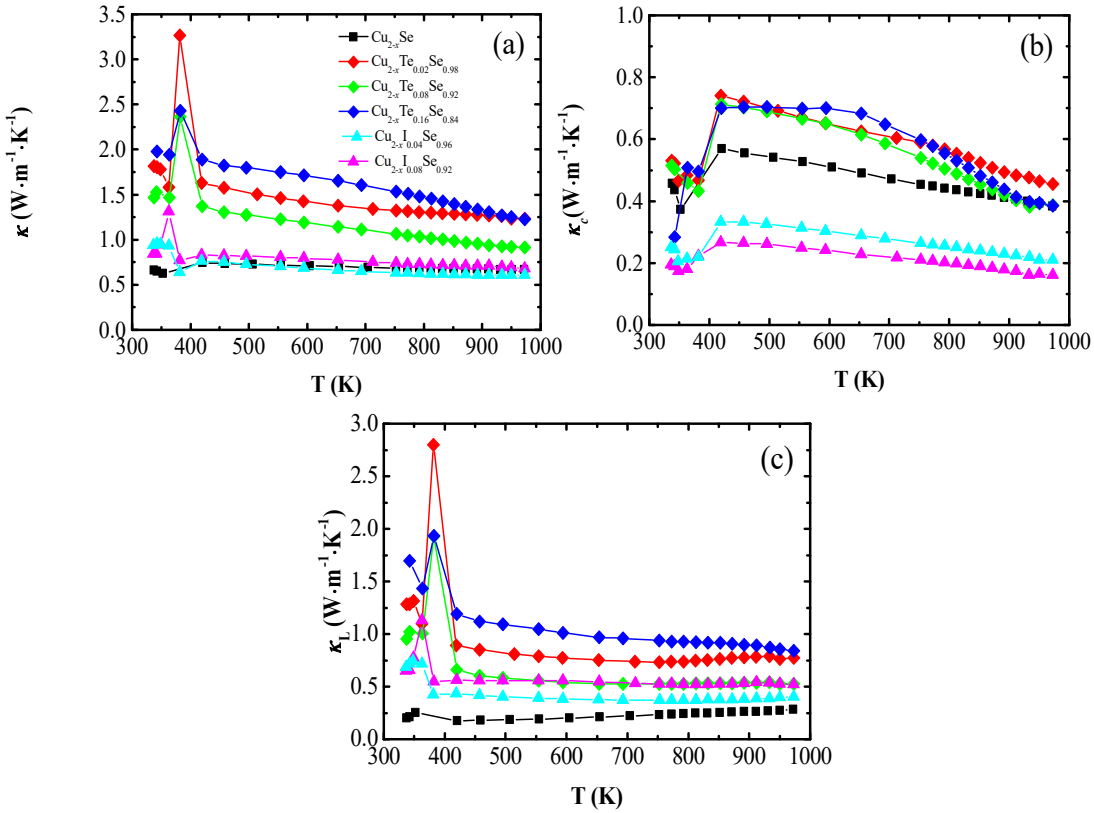

Figure 6-10 Temperature dependence of the total thermal conductivity (κ), and the calculated lattice thermal conductivity (κ_L), and the charge carrier thermal conductivity (κ_c) for the fabricated high dense un-doped, Te-doped, and I-doped $Cu_{2-x}Se$ samples.

In order to further investigate the doping effects of heavier atoms on the thermal transport properties of the $Cu_{2-x}Se$ system, we have also calculated κ_L and κ_c. According to the Wiedemann-Franz relationship, κ_c can be estimated by $\kappa_c = LT\sigma$, where L is the Lorenz number.[6, 32-34] Here, we take $L = 1.5 \times 10^{-8}$ V^2·K^{-2} to calculate κ_c. Our results

show that the I-doped $Cu_{2-x}Se$ samples have significantly reduced κ_c, which can be attributed to the lower carrier concentration caused by the lower valence compared to Se^{2-}. The Te-doped $Cu_{2-x}Se$ samples have much higher κ_c than the un-doped sample in the temperature range from room temperature to 750 K, after which the κ_c decreases slightly.

All the Te- and I-doped $Cu_{2-x}Se$ samples, however, have higher κ_L values compared to the un-doped sample, which is unexpected, because both Te and I are much heavier than Se. In addition, both Te and I expand the lattice parameters and could give more space for the copper ions to migrate. The strengthened migration of copper ions in the $Cu_{2-x}Se$ system will cause both strong scattering of phonons and TO-branch softening (liquid-like),[35] which make the liquid-like behaviour become more significant with lower κ_L values. The observed κ_L values for all the Te- and I-doped $Cu_{2-x}Se$ samples are increased, however, compared to the un-doped one. Therefore, the expanded lattice parameter may not be a direct influence that affects the thermal transport, and high temperature inelastic X-ray scattering experiments will be helpful to gain insight into the phonon spectrum in relation to the enhanced thermal conductivity for both Te-doped, and I-doped $Cu_{2-x}Se$. These will be carried out in our further study in the near future. So, doping with heavier atoms can have some positive effects on certain thermoelectric parameters, such as the electrical conductivity or Seebeck coefficient, to some extent, although the system's overall thermoelectric performance may not be enhanced.

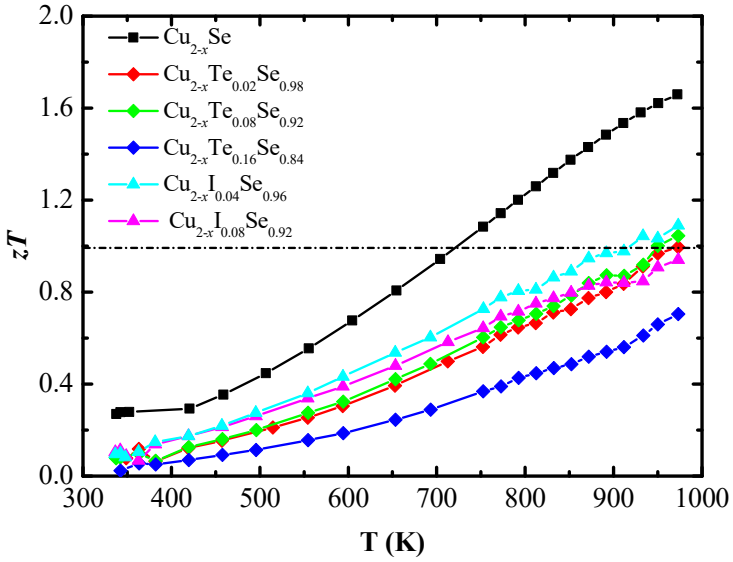

Figure 6-11 Temperature dependence of the dimensionless figure-of-merit (zT) for the obtained un-doped, Te-doped, and I-doped $Cu_{2-x}Se$ bulks.

Figure 6-11 shows the temperature dependence of the dimensionless thermoelectric figure-of-merit (zT) for all the undoped, Te-doped, and I-doped $Cu_{2-x}Se$ samples. It is notable that the undoped $Cu_{2-x}Se$ exhibits a zT of 1.7 at 973 K and $zT > 1$ for $T > 700$ K. All of the Te- and I-doped $Cu_{2-x}Se$ samples also show zT close to 1.0 at 973 K. Although all of our samples were prepared by the melt-quenching method, which only took a few minutes, their overall thermoelectric performance is as good as what has been reported for the same compounds made by the lengthy hot-pressing method requiring high-pressure heat treatments.[14, 15]

A typical cross-sectional field emission scanning electron microscope (FE-SEM) image for the fabricated un-doped, Te-doped, and I-doped $Cu_{2-x}Se$ bulks is displayed in

Figure 6-12 . It indicates that the bulks produced by the ultra-fast formation method are highly dense and consist of micro-scale grains with no obvious voids.

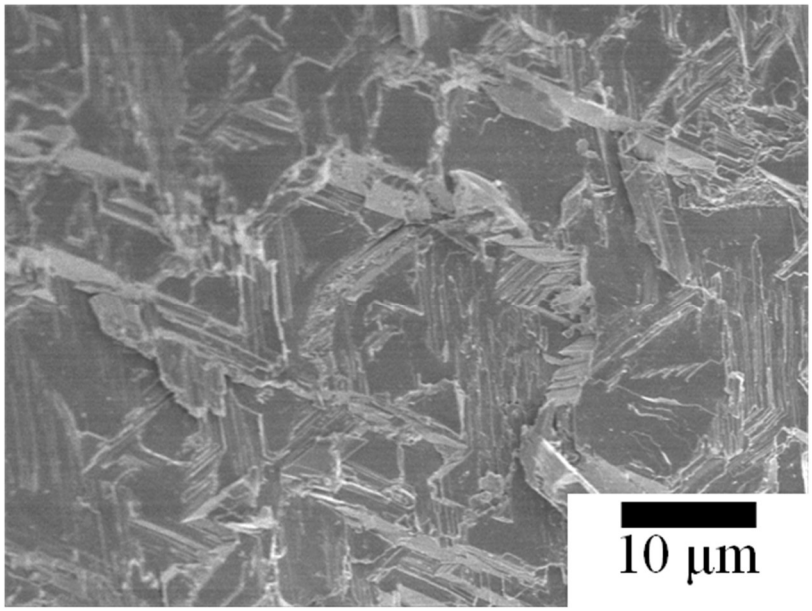

Figure 6-12 Typical cross-sectional FE-SEM image for the fabricated un-doped, Te-doped, and I-doped $Cu_{2-x}Se$ bulks

6.3.4 Hardness

As good mechanical performance is quite essential for the practical applications of thermoelectric materials, we have determined the hardness for all the obtained bulks. According to the relationship between hardness and dislocations, the maximal energy of the elastic interaction between a dislocation and an impurity atom can be estimated by the interaction parameter, ξ, which can be defined as $\xi = \frac{r_1 - r_0}{r_0}$, where r_0 is the radius of the substituted matrix atom and r_1 is the radius of the impurity atom, respectively. The higher the interaction parameter, the greater the lattice distortion will be, which is proportional to the hardness of the material. Using the covalent radius of r_0 = 1.17 Å for Se, r_1 = 1.33 Å for I, and r_1 = 1.35 Å for Te to calculate ξ, we can obtain the values of

0.154 for Te-doping and 0.137 for I-doping, respectively. Both values are positive, so we propose that the Te- and I-doped samples should have higher hardness values compared to the un-doped one.

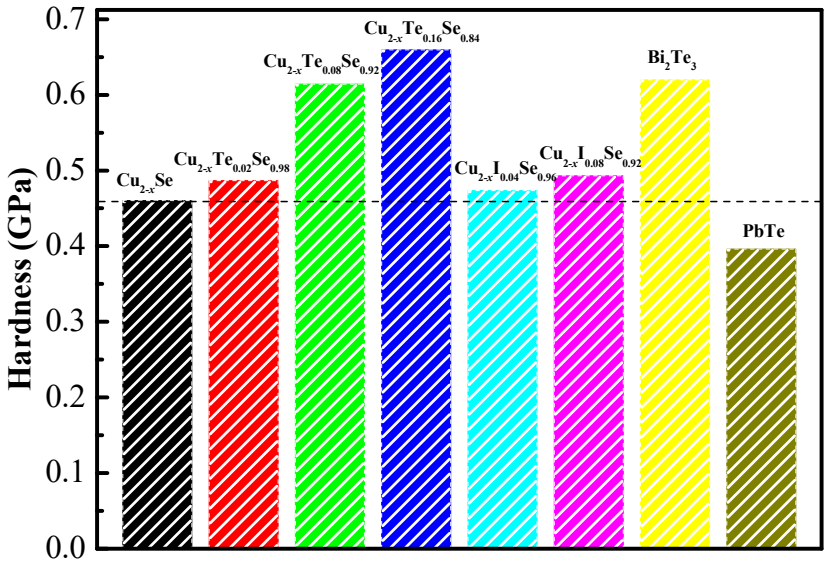

Figure 6-13 Micro-hardness values of the obtained highly dense un-doped, Te-doped, and I-doped $Cu_{2-x}Se$ bulks.

Figure 6-13 shows the micro-hardness values of the ultra-fast-formed un-doped, Te-doped, and I-doped $Cu_{2-x}Se$ bulks. It indicates that the un-doped $Cu_{2-x}Se$ sample has a hardness of ~0.46 GPa, which is higher than the hardness of polycrystalline PbTe bulks (~0.40 GPa).[36] It should be noted that the hardness is distinctly enhanced by Te- and I-doping, with improvement of ~8% for the $Cu_{2-x}I_{0.08}Se_{0.92}$ sample (~0.50 GPa) and 43% for the $Cu_{2-x}Te_{0.16}Se_{0.84}$ sample (~0.66 GPa), respectively. The enhanced hardness for the $Cu_{2-x}Te_{0.16}Se_{0.84}$ is higher than that of hot-pressed Bi_2Te_3 (~0.62 GPa) bulks.[37] The improved mechanical performance combined with the good thermoelectric

performance offered by the doping approach gives $Cu_{2-x}Se$ great potential for high temperature thermoelectric applications.

6.4 Conclusions

DFT calculations indicate that stoichiometric Cu_2Se is a zero-gap material and copper deficient $Cu_{1.875}Se$ is an intrinsic *p*-type conductor. Te^{2-} substitution increases the total DOS at E_F due to its 5*p*-electron contribution. Whereas, the I^- substitution leads to the reduction of the total and partial DOS for both Se and Cu as a result of the localization of the I^- 5*p* electrons. Compared to the highly dense un-doped $Cu_{2-x}Se$ bulks, the Te-doped and I-doped $Cu_{2-x}Se$ bulks do not show enhanced *zT* values due to the decreased electrical conductivity and increased thermal conductivity. It should be noted that all the bulks fabricated by the melt-quenching method show *zT* over or close to 1.0 at T = 973 K, except for the $Cu_{2-x}Te_{0.16}Se_{0.84}$. Furthermore, hardness of ~ 0.66 GPa is achieved for the $Cu_{2-x}Te_{0.16}Se_{0.84}$, which is higher than those of polycrystalline Bi_2Te_3 and PbTe bulks.

References

[1] D. M. Rowe, CRC Handbook of thermoelectric, CRC Handbook of thermoelectrics, CRC press, FL 1995.

[2] B. C. Sales, Smaller is cooler, Science 2002, 295, 1248.

[3] G. J. Snyder, Toberer, E. S. , Complex thermoelectric materials, Nat. Mater. 2008, 7, 10.

[4] J. Yang, Y. Hin-Lap, A. K. Y. Jen, Rational design of advanced thermoelectric materials, Adv. Energy Mater. 2013, 3, 549.

[5] D. M. Rowe, CRC hand book of thermoelectrics: macro to nano, CRC hand book of thermoelectrics: macro to nano. CRC Press, New York 2005.

[6] Y. Z. Pei, A. D. Lalonde, N. A. Heinz, X. Shi, S. Iwanaga, H. Wang, L. D. Chen, G. J. Snyder, Stabilizing the optimal carrier concentration for high thermoelectric efficiency, Adv. Mater. 2011, 23, 5674.

[7] S. K. Bux, R. G. Blair, P. K. Gogna, H. Lee, G. Chen, M. S. Dresselhaus, R. B. Kaner, J.-P. Fleurial, Nanostructured bulk silicon as an effective thermoelectric material, Adv. Funct. Mater. 2009, 19, 2445.

[8] G. S. Nolas, J. Poon, M. Kanatzidis, Recent developments in bulk thermoelectric materials, MRS Bull. 2006, 31, 199.

[9] C. J. Vineis, A. Shakouri, A. Majumdar, M. G. Kanatzidis, Nanostructured thermoelectrics: big efficiency gains from small features, Adv. Mater. 2010, 22, 3970.

[10] M. Zebarjadi, K. Esfarjani, M. S. Dresselhaus, Z. F. Ren, G. Chen, Perspectives on thermoelectrics: from fundamentals to device applications, Energy Environ. Sci. 2012, 5, 5147.

[11] G. Chen, M. S. Dresselhaus, G. Dresselhaus, J. P. Fleurial, T. Caillat, Recent developments in thermoelectric materials, International Materials Reviews 2003, 48, 45.

[12] W. Liu, X. Yan, G. Chen, Z. Ren, Recent advances in thermoelectric nanocomposites, Nano Energy 2012, 1, 42.

[13] D. D. Pollock, Thermalcouples: Theory and Properties, CRC Press, Boca Raton, FL 1991.

[14] H. Liu, X. Shi, F. Xu, L. Zhang, W. Zhang, L. Chen, Q. Li, C. Uher, T. Day, G. J. Snyder, Copper ion liquid-like thermoelectrics, Nat. Mater. 2012, 11, 422.

[15] B. Yu, W. Liu, S. Chen, H. Wang, H. Wang, G. Chen, Z. Ren, Thermoelectric properties of copper selenide with ordered selenium layer and disordered copper layer, Nano Energy 2012, 1, 472.

[16] X. Shi, J. Yang, J. R. Salvador, M. Chi, J. Y. Cho, H. Wang, S. Bai, J. Yang, W. Zhang, L. Chen, Multiple-filled skutterudites: high thermoelectric figure of merit through separately optimizing electrical and thermal transports, J. Am. Chem. Soc. 2011, 133, 7837.

[17] Q. Zhang, F. Cao, W. Liu, K. Lukas, B. Yu, S. Chen, C. Opeil, D. Broido, G. Chen, Z. Ren, Heavy doping and band engineering by potassium to improve the thermoelectric figure of merit in p-type PbTe, PbSe, and $PbTe_{(1-y)}Se_{(y)}$, J. Am. Chem. Soc. 2012, 134, 10031.

[18] K. Biswas, J. He, I. D. Blum, C. I. Wu, T. P. Hogan, D. N. Seidman, V. P. Dravid, M. G. Kanatzidis, High-performance bulk thermoelectrics with all-scale hierarchical architectures, Nature 2012, 489, 414.

[19] H. Liu, X. Yuan, P. Lu, X. Shi, F. Xu, Y. He, Y. Tang, S. Bai, W. Zhang, L. Chen, Y. Lin, L. Shi, H. Lin, X. Gao, X. Zhang, H. Chi, C. Uher, Ultrahigh

thermoelectric performance by electron and phonon critical scattering in $Cu_2Se_{1-x}I_x$, Adv. Mater. 2013, 25, 6607.

[20] D. R. Brown, T. Day, T. Caillat, G. J. Snyder, Chemical Stability of $(Ag,Cu)_2Se$: a Historical Overview, J. Electron. Mater. 2013, 42, 2014.

[21] Y. Gelbstein, Z. Dashevsky, M. P. Dariel, The search for mechanically stable PbTe based thermoelectric materials, J Appl Phys 2008, 104, 033702.

[22] M. S. Ablova, M. N. Vinogradova, M. I. Karklina, Effect of donor and acceptor impurities on microhardness of PbTe, Sov. Phys. Solid State 1969, 10, 1929.

[23] S. J. Clark, M. D. Segall, C. J. Pickard, P. J. Hasnip, M. I. J. Probert, K. Refson, M. C. Payne, First principles methods using CASTEP, Z. Kristallogr. 2005, 220, 567.

[24] P. Hohenberg, Inhomogeneous electron gas, Phys. Rev. 1964, 136, B864.

[25] J. P. Perdew, K. Burke, M. Ernzerhof, Generalized Gradient Approximation Made Simple, Phys. Rev. Lett. 1996, 77, 3865.

[26] H. J. Monkhorst, J. D. Pack, Special points for Brillouin-zone integrations, Physical Review B 1976, 13, 5188.

[27] M. Rasander, L. Bergqvist, A. Delin, Density functional theory study of the electronic structure of fluorite Cu_2Se, J. Phys. Condens. Matter. 2013, 25, 125503.

[28] X. Wang, S. X. Dou, C. Zhang, Zero-gap materials for future spintronics, electronics and optics, NPG Asia Mater. 2010, 2, 31.

[29] X. Wang, Proposal for a New Class of Materials: Spin Gapless Semiconductors, Phys. Rev. Lett. 2008, 100.

[30] A. Bulusu, D. G. Walker, Review of electronic transport models for thermoelectric materials, Superlattice Microst. 2008, 44, 1.

[31] M. Cutler, J. Leavy, R. Fitzpatrick, Electronic transport in semimetallic cerium sulfide, Phys. Rev. 1964, 133, A1143.

[32] J. Androulakis, C. H. Lin, H. J. Kong, C. Uher, C. I. Wu, T. Hogan, B. A. Cook, T. Caillat, K. M. Paraskevopoulos, M. G. Kanatzidis, Spinodal decomposition and nucleation and growth as a means to bulk nanostructured thermoelectrics: enhanced performance in $Pb_{1-x}Sn_xTe$-PbS, J. Am. Chem. Soc. 2007, 129, 9780.

[33] A. Bejan, A. D. Allan, Heat Transfer Handbook, Wiley, New York, 2003.

[34] R. J. Mehta, Y. Zhang, C. Karthik, B. Singh, R. W. Siegel, T. Borca-Tasciuc, G. Ramanath, A new class of doped nanobulk high-figure-of-merit thermoelectrics by scalable bottom-up assembly, Nat. Mater. 2012, 11, 233.

[35] H. Liu, Y. He, X. Shi, X. Guo, L. Chen, Recent progress in “phonon-liquid” thermoelectric materials, Chinese Science Bulletin (Chinese Version) 2013, 58, 2603.

[36] Y. Gelbstein, G. Gotesman, Y. Lishzinker, Z. Dashevsky, M. P. Dariel, Mechanical properties of PbTe-based thermoelectric semiconductors, Scripta Mater 2008, 58, 251.

[37] K. Ueno, A. Yamamoto, T. Noguchi, T. Inoue, S. Sodeoka, H. Obara, Optimization of hot-press conditions of Zn_4Sb_3 for high thermoelectric performance. II. Mechanical properties, J. Alloys Compd. 2005, 388, 118.

7 CONCLUSIONS AND PROPOSED FUTURE WORK

In this thesis, highly dense $Cu_{2-x}S$ and $Cu_{2-x}Se$ based thermoelectric materials were successfully fabricated by a low-cost and time-saving melt-quenching approach. We also investigated the structural properties, electronic structures, and mechanical and thermoelectric properties for the pure $Cu_{2-x}S$ (x = 0 and 0.03), pure $Cu_{2-x}Se$ (x = 0 and 0.02), $Cu_{1.98}S_xSe_{1-x}$ alloys, and Te-doped and I-doped $Cu_{2-x}Se$ systems.

7.1 Pure $Cu_{2-x}S$ system

The studies on the structural properties, electronic structures, and mechanical and thermoelectric properties for the pure $Cu_{2-x}S$ bulks indicate that the melt-solidification technique works well for the fabrication of highly dense $Cu_{2-x}S$ (x = 0 and 0.03) polycrystalline bulks. The fabricated $Cu_{1.97}S$ bulks show excellent thermoelectric performance, with zT as high as ~1.9 at 973 K, and good mechanical properties with a Vickers hardness of ~ 1.0 GPa. Density functional theory calculations reveal that stoichiometric Cu_2S is a small-band-gap semiconductor, and copper deficiency makes the copper deficient $Cu_{2-x}S$ a p-type conductor. The synthesized $Cu_{2-x}S$ (x = 0 and 0.03) bulks show quite good repeatibility in terms of the thermal diffusivity during the repeated heating and cooling processes, although they exhibit poor electrical stability under concurrent high temperature and high electrical field.

7.2 Pure $Cu_{2-x}Se$ system

The results indicate that the fast melt-solidification approach is an effective method for the fabrication of highly dense $Cu_{2-x}Se$ bulks with excellent thermoelectric performance, with $zT \approx 1.7$ at 973 K. Furthermore, this method should be applicable to other types of congruent-melting thermoelectric materials, based on our discussions. It is remarkable that the fabrication cost can be reduced significantly, as the synthesis only takes a few minutes. There is evidence that it is the cubic crystal symmetry and liquid-like behaviour of copper ions that makes $Cu_{2-x}Se$ show superior thermoelectric performance. The present findings not only pave the way for commercialization of $Cu_{2-x}Se$ as an excellent component in thermoelectric modules, but also provide guidance in searching for new classes of isotropic thermoelectric systems or further improving the cost performance of other congruent-melting thermoelectric materials.

7.3 $Cu_{1.98}S_xSe_{1-x}$ system

The results derived from density functional theory calculations indicate that all the copper deficient $Cu_{15}S_xSe_{8-x}$ compounds are intrinsic *p*-type conductors. Sulphur doping has non-monotonic effects on the DOS and m^*, with the $Cu_{15}S_6Se_2$ and $Cu_{15}S_4Se_4$ having the highest DOS values, ~ 0.69 states/eV/f.u., and the highest m^*, ~ 0.336 m_e, respectively. The $Cu_{1.98}S_xSe_{1-x}$ compounds have the same crystal structure as monoclinic-structured Cu_2Se when $x \leq 0.16$, become

composites of cubic-structured $Cu_{1.8}Se$ and hexagonal-structured $Cu_{2.001}S$ when $0.2 \leq x \leq 0.7$, and finally have the same crystal structure as orthorhombic-structured Cu_2S when $0.8 \leq x \leq 1.0$. The overall thermoelectric performance of the $Cu_{1.98}S_xSe_{1-x}$ compounds is mainly correlated with the electron effective mass and the density of states, with the zT values firstly increasing and then decreasing. Additionally, all the samples show stable thermoelectric compatibility factors over a broad temperature range from 700 to 1000 K, which could greatly benefit their practical applications.

7.4 Te-doped and I-doped $Cu_{2-x}Se$ system

Density functional theory calculations indicate that stoichiometric Cu_2Se is a zero-gap material and that copper deficient $Cu_{1.875}Se$ is an intrinsic *p*-type conductor. Te^{2-} substitution increases the total DOS at E_F due to its 5*p*-electron contribution. Whereas, I^- substitution leads to the reduction of the total and partial DOS for both Se and Cu as a result of the localization of the I^- 5*p* electrons. Compared to the highly dense un-doped $Cu_{2-x}Se$ bulks, the Te-doped and I-doped $Cu_{2-x}Se$ bulks do not show enhanced zT values due to the decreased electrical conductivity and increased thermal conductivity. It should be noted that all the bulks fabricated by the melt-quenching method show zT over or close to 1.0 at $T = 973$ K, except for the $Cu_{2-x}Te_{0.16}Se_{0.84}$. Furthermore, hardness of ~ 0.66 GPa is achieved for the $Cu_{2-x}Te_{0.16}Se_{0.84}$, which is higher than those of polycrystalline Bi_2Te_3 and PbTe bulks.

7.5 Proposed future work

Theoretical calculations on the electrical and thermal transport parameters are powerful for determining whether a given thermoelectric system is promising or not. Hence, it is quite essential to perform some calculations on the electronic band structures, density of states, and phonons to estimate the thermoelectric performance of the particular thermoelectric system before performing any experiments.

For practical applications of the superionic $Cu_{2-x}Se$ and $Cu_{2-x}S$ based thermoelectric materials, the stability under concurrent high temperature and electric field should be one crucial factor. This doctoral research on the $Cu_{2-x}S$ system indicates that this system has poor thermal stability under repeated measurements. Therefore, it is important to develop some methods to enhance the electrical and thermal stability through suppressing the evaporation of elements or improving the structural stability.

The doping approach is an effective method that is used to modify the electrical and thermal transport properties of thermoelectric materials to obtain greatly improved thermoelectric performance. Doping with S, Te, and I into the Se sites of $Cu_{2-x}Se$ was investigated in previous work in our laboratory. Unfortunately, these dopants cannot improve the overall thermoelectric performance of the $Cu_{2-x}Se$ system, even though certain thermoelectric parameters are indeed modified. It might be possible to obtain improved thermoelectric performance by using dopants that substitute into Cu sites of this compound, according to our calculated DOS for $Cu_{2-x}Se$ and the already published

work on Ag-doped $Cu_{2-x}Se$. These experiments on doping into Cu sites will be carried out in our group in future.

PUBLISHED PAPERS

1. L. L. Zhao, X. L. Wang, F. F. Yun, J. Y. Wang, Z. X. Cheng, S. X. Dou, J. Wang, G. Jeffrey Snyder, The effects of Te^{2-} and I^{-} substitutions on the electronic structures, thermoelectric performance, and hardness in melt-quenched highly dense $Cu_{2-x}Se$, Advanced Electronic Materials, 2015, 1, 1400015.

2. L. L. Zhao, X. L. Wang, F. F. Yun, J. Y. Wang, Z. X. Cheng, S. X. Dou, J. Wang, G. Jeffrey Snyder, High thermoelectric and mechanical performance in highly dense $Cu_{2-x}S$ bulks prepared by a melt-solidification technique, Journal of Materials Chemistry A, 2015, 3, 9432-9437.

3. L. L. Zhao, X. L. Wang, J. Y. Wang, Z. X. Cheng, S. X. Dou, J. Wang, L. Q. Liu, Superior intrinsic thermoelectric performance with *zT* of 1.8 in single-crystal and melt-quenched highly dense $Cu_{2-x}Se$ bulks, Scientific Reports, 2015, 5, 7671-1-7671-6.

4. L. L. Zhao, X. L. Wang, J. Y. Wang, Z. X. Cheng, J. Wang, N. Yin, Z. G. Gai, A. Jalalian, S. X. Dou, Cobalt doping effects on photoluminescence, Raman scattering, crystal structure, and magnetic and piezoelectric properties in ZnO single crystals grown from molten hydrous LiOH and NaOH solutions, Journal of Alloys and Compounds, 2015, 628, 303-307.

5. Z. G. Gai, Z. X. Cheng, X. L. Wang, L. L. Zhao, N. Yin, R. Abah, M. L. Zhao, F. Hong, Z. Y. Yu, S. X. Dou, A colossal dielectric constant of an amorphous TiO_2:(Nb, In)

film with low loss fabrication at room temperature, Journal of Materials Chemistry C, 2014, 2, 6790-6795.

6. N. Yin, A. Jalalian, Z. G. Gai, L. L. Zhao, X. L. Wang, Effect of doping ions on structure and electrical properties of lead-free KNN ceramics, Advanced Materials Research, 2014, 1058, 190-195.

7. N. Yin, A. Jalalian, L. L. Zhao, Z. G. Gai, Z. X. Cheng, X. L. Wang, Correlation between crystal structures, Raman scattering and piezoelectric properties of lead-free $Na_{0.5}K_{0.5}NbO_3$, 2015, Journal of Alloys and Compounds, 652, 341-345.

8. L. L. Zhao, F. F. Yun, J. Wang, J. Y. Wang, Z. X. Cheng, S. X. Dou, X. L. Wang, High thermoelectric performance of the excess silver doped $SnAg_xTe$ compounds via concurrent high power factor and low thermal conductivity, Journal of Materials Chemistry C. (Under Review)

9. L. L. Zhao, F. F. Yun, J. Wang, J. Y. Wang, N. Ye, Z. X. Cheng, S. X. Dou, X. L. Wang, Sulphur doping effects on the density-of-states, effective mass, and thermoelectric properties of $Cu_{1.98}S_xSe_{1-x}$.(To be submitted)

10. L. L. Zhao, F. X. Xiang, F. F. Yun, F. F. Yun, J. Wang, J. Y. Wang, Z. X. Cheng, S. X. Dou, X. L. Wang, Structural and electronic transport properties for black phosphorus single crystals. (To be submitted)

11. L. L. Zhao, J. Wang, F. F. Yun, S. N. Islam, J. Y. Wang, Z. X. Cheng, S. X. Dou, X. L. Wang, Band structure modification and high thermoelectric performance of the antimony doped $Sn_{1-x}Sb_xTe$ compounds. (To be submitted)

12. L. L. Zhao, F. F. Yun, J. Wang, J. Y. Wang, Z. X. Cheng, S. X. Dou, X. L. Wang, High thermoelectric performance for the $SnTe_{1-x}S_x$ alloys over a wide temperature range. (To be submitted)